Charles University Prague
Faculty of Mathematics and Physics

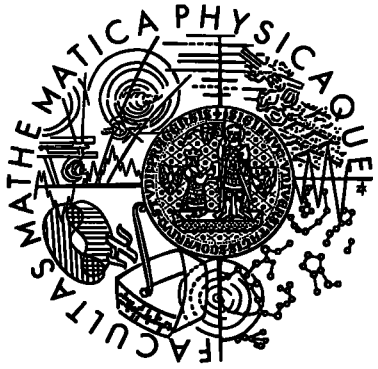

On the relation between properties and microstructure of new Mg based alloys and their composites for advanced structural applications

Doctoral thesis in branch F-3,
Physics of Condensed Matter and Materials Research

Oksana Padalka

Thesis supervisor: Prof. RNDr. Zuzanka Trojanová, DrSc.
Department of Physics of Materials

Prague 2008

Contents

List of Abbreviations and Symbols Used in the Thesis

ASTM - American Society for Testing and Materials;

AE - acoustic emission;

BF - bright field;

CDF - centered dark field;

CRSS - critical resolved shear stress;

CTE - coefficient of thermal expansion;

DF - dark field;

DP - diffraction patterns;

EBSD - electron backscatter diffraction;

ECAP - equal channel angular pressing;

EDAX - energy dispersive X-ray analyser;

hcp - hexagonal close packing;

LM - Light microscopy;

Mischmetal - mixture with a dominant element;

MMC - metal matrix composite;

PIMS - Precision Ion-Milling System;

PIPS - Precision Ion-Polishing System;

RE - rare earth metal;

SR - stress relaxation;

TEM - Transmission electron microscopy;

HV - Vickers microhardness;

a_1 - constant determined by the geometry, the dislocation density, and the modulus of elasticity;

B - geometrical constant;

b - Burgers vector;

b_1 - constant determined by the geometry, the dislocation density, and the modulus of elasticity;

C - contrast;

d - arithmetic mean of the indentation diagonals;

$d1$, $d2$ - indentation diagonals;

d_t - fibre size in the direction perpendicular to the applied stress;

E - Young modulus;

F - load;

f - volume fraction of the reinforcement (fibre);

G - shear modulus;

ΔG - Gibbs enthalpy;

$\boldsymbol{g}$ - vector of reciprocal space;

I - intensity;

ΔI - difference in the intensity;

$\boldsymbol{K}$ - vector of scattering;

$\boldsymbol{k}$ - wave vector;

k - Boltzmann constant;

k_0 - wave vector magnitude;

k_1 - material constant;

L - fibre size in the direction of the applied stress;

l - sample length;

m - strain rate sensitivity parameter;

p - phenomenological parameter;

q - phenomenological parameter;

r - position vector;

r_1 - constant determined by geometry, dislocation density, and modulus of elasticity;

$\boldsymbol{s}$ - deviation vector;

t_0 - time constant;

T - temperature;

T_0 - initial temperature;

ΔT - temperature difference;

V - activation volume;

v - dislocation velocity;

z - function of geometry and distribution of the fibres and elastic properties of the matrix and fibres;

α - coefficient of thermal expansion;

α_c - coefficients of thermal expansion of a composite;

α_c^{Emodel} - coefficient of thermal expansion determined from the elastic models;

α_f - coefficients of thermal expansion of the fibres;

α_m - coefficients of thermal expansion of the matrix;

$\Delta\alpha$ - difference in the expansion coefficients of the components;

β - constant;

γ - constant;

$\dot{\varepsilon}$ - strain rate;

ε_f - elongation to failure;

ε_{mis} - thermal mismatch strain;

ε_p - plastic strain;

ε_T - thermal strain;

ρ - dislocation density;

$\Delta\rho$ - total dislocation density;

ρ_G - dislocation density of geometrically necessary dislocations;

ρ_m - density of mobile dislocations;

ρ_T - thermal dislocation density;

σ - stress;

σ^* - effective stress;

σ_{ap} - applied stress;

σ_i - internal stress;

σ_{meff} - von Mises effective stress;

σ_{LT} - stress necessary for the load transfer;

σ_{TM} - stress induced by the thermal mismatch strain;

σ_{TS} - thermal stress;

Ψ - plane wave;

Ψ_0 - wave amplitude;

ψ - Taylor factor.

Preface

Magnesium alloys, due to their attractive properties such as low density, high specific strength and stiffness, excellent castability, good dimensional stability, and high damping capacity, find applications in automotive, aircraft, space, and other industries. Moreover, magnesium alloys have good ecological properties, including low toxicity, reusability and recyclability (unlike many polymers), and the increasing use of light magnesium alloys lead to the reduction of greenhouse gas emissions. However, limited strength, especially at elevated temperatures, low creep resistance, low cold formability (due to the hexagonal close packed (hcp) structure with a limited number of slip systems), and low corrosion resistance of magnesium alloys retard their applications. Some of these properties can be improved by novel processing technologies (rolling, Equal Channel Angular Pressing (ECAP)) while other properties (e.g., stiffness and strength) can be controlled by addition of reinforcements. Rolling and ECAP processing led to the development of new materials with attractive properties, which have not been yet fully investigated.

Mechanisms that determine properties of magnesium alloys and its composites can be revealed by investigations of their internal structure (crystal lattice, dislocations and their distribution, twins, grain boundaries, precipitates, etc.). The most comprehensive knowledge of the internal structure can be obtained from the transmission electron microscopy (TEM). Therefore, in order to extend the knowledge of deformation mechanisms which control mechanical and physical properties, the microstructure of plastically deformed Mg alloys and its composites was investigated by TEM and correlated with their mechanical and physical properties.

The thesis is arranged as follows. Chapters 1, 2 and 3 present basic properties of magnesium alloys and its composites. Chapter 4 presents the aims of the thesis. Chapter 5 describes used experimental methods and materials. Chapter 6 presents the results of the study of substructure and mechanical and physical properties of new magnesium alloys and its composites. Finally, Chapter 7 summarizes the conclusions of the thesis.

A significant part of the work was supported by the Research Project 1M 2560471601 "Eco-centre for Applied Research of Non-ferrous Metals" financed by the Ministry of Education, Youth and Sports of the Czech Republic.

I would like to thank all my colleagues from the Department of Physics of Materials for their help and support. Particularly, I am grateful to my thesis supervisor Prof. RNDr. Zuzanka Trojanová, DrSc. for her continuous help during the postgraduate study and the thesis preparation. I also greatly appreciate numerous consultations by Prof. RNDr. Pavel Lukáč, DrSc., who significantly helped me in my work. I am greatly thankful to my thesis consultant Doc. RNDr. Miloš Janeček, CSc. for supervising me in the TEM observations. I am also thankful to him for organizing my stay at the Clausthal University of Technology and for the help in solving administrative problems connected with it. I greatly appreciate Doc. RNDr. Josef Pešička, CSc., Doc. RNDr. Bohumil Smola, CSc., and Doc. RNDr. Miroslav Cieslar, CSc. for their technical support and advices during my work in the TEM laboratory. Also, I would like to thank Mgr. Zoltán Száraz for the cooperation in microhardness measurements.

Chapter 1

Magnesium alloys

1.1 Crystallography of magnesium alloys

The deformation behaviour of magnesium alloys is strongly influenced by the limited crystallographic equivalent slip systems owing to hcp (hexagonal close packing) structure. The main slip system in magnesium and magnesium alloys is the basal slip. Non-basal (prismatic and pyramidal) slip systems may be activated under some conditions. Figure 1.1 shows the lattice structure and three slip systems of magnesium. The easiest slip system is a $(0001) < \bar{1}2\bar{1}0 >$ slip on basal plane in an a-axis slip direction. According to the von Mises criterion (*von Mises*, 1928), at least five independent slip systems are necessary for compatible deformation of polycrystals. Therefore, to fulfil the von Mises criterion, non-basal slip systems should be activated. However, the activation of non-basal slip systems is not energetically favourable at room temperature. Hence, mechanical twinning is the next significant mode of deformation. Twinning may reorient some grains to a more favourable orientation for basal slip (*Zhang et al.*, 2000) and thereby activating fresh slip systems (*Bohlen et al.*, 2002). The non-basal slip systems are a $\{10\bar{1}1\} < \bar{1}2\bar{1}0 >$ first-order pyramidal slip system with an a-axis slip direction, a $\{10\bar{1}1\} < \bar{1}\bar{1}23 >$ first-order pyramidal plane slip system with a $< c+a >$ slip direction, and a $\{11\bar{2}2\} < \bar{1}\bar{1}23 >$ second-order pyramidal slip system with a $< c+a >$ slip direction.

Detailed information about slip systems and twinning can be obtained from TEM observations and mechanical test results. The main advantages of TEM include: (i) ex-

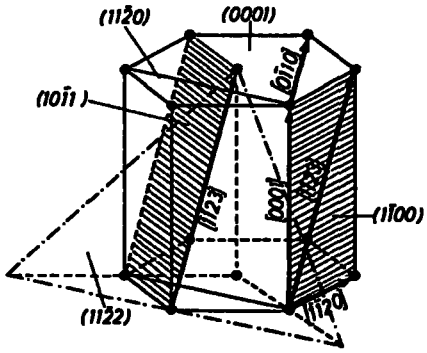

Figure 1.1: Slip systems in magnesium (*Friedrich and Mordike*, 2006).

tremely high resolution, as high as individual atomic planes in special cases, (ii) ability to determine the Burgers vector of dislocation by diffraction techniques, and (iii) ability to image dislocations without significantly affecting their behaviour. An overview of microstructure TEM investigation of plastically deformed Mg based alloys and its composites is presented in Chapter 3.

1.2 Classification of magnesium alloys

Magnesium alloys are usually classified by the product form: cast (including squeeze casting, die-casting), forged, wrought, or filler metal. Another classification is possible that divides alloys according to their composition. The detailed information about the classification by composition is given in *Drápala et al.* (2004). Additionally, magnesium alloys can be generally grouped into those that contain aluminum as an alloying element and those that do not. Because most Al-free alloys contain zirconium additions to refine the grain structure (magnesium-manganese alloys are the main exception), magnesium alloy systems can be alternatively grouped as zirconium-free and zirconium-containing ones. This classification is used in the thesis. The following two sections describe properties of the investigated materials as the function of zirconium content.

Magnesium alloys as other alloys are usually labelled according to the nomenclature of the American Society for Testing and Materials (ASTM) (*Avedesian and Baker*, 1999). This nomenclature is a letter-number system. The first part consists of code letters indicating the two principal alloying elements (listed in the order of decreasing alloying

amount). These code letters are listed in Table 1.1. The second part consists of the weight percentages of these two elements (rounded off to the nearest whole number and listed in the same order as the code letters).

Table 1.1: Marking of elements in the magnesium (and other) alloys according to ASTM.

A:	Aluminum	M:	Manganese	S:	Silicon	B:	Bismuth
N:	Nickel	T:	Tin	C:	Copper	P:	Lead
W:	Yttrium	D:	Cadmium	Q:	Silver	Y:	Antimony
E:	Rare earth metals	R:	Chromium	Z:	Zinc	L:	Lithium
K:	Zirconium	H:	Thorium	X:	Calcium	J:	Strontium

1.2.1 Zirconium-free magnesium alloys

Mg-Al-Zn alloy system

The earliest commercially used alloying elements were aluminum, zinc, and manganese. The Mg-Al-Zn-Mn alloys are characterized by low cost together with good strength, ductility, and improved corrosion resistance. The maximum solid solubility of aluminum in magnesium is 12.7 wt.% at 437 °C, decreasing to about 2 % at room temperature. In the as cast condition, a mixture of the α phase (substitution solid solution Al in Mg) and β phase ($Mg_{17}Al_{12}$) forms. The binary $Mg_{17}Al_{12}$ phase is very brittle and therefore, the alloys with the high content of eutectic phase have low usage. Commercial alloys based on Mg-Al and containing Zn as a next alloying element are AZ91, AZ81, AZ61, AZ31. Shape of the β phase depends on presence of Zn in the alloys. Quenching of the alloy with less than 8 % of Al causes formation of the lamellar form precipitates on grain boundaries. Manganese is added for control of corrosion (*Drápala et al.*, 2004).

Mg-Al-Si alloy system

These alloys (AS series) were initially developed for the Volkswagen company around 1970 as a response to the trend to use Mg alloys in applications requiring stress retention and creep-resistance at temperatures up to 150 °C. Alloys of Mg-Al-Si series contain

aluminum for castability and room temperature strength, silicon for creep resistance and manganese for corrosion resistance (*Albright*, 1995). Silicon is one of the inexpensive alloying elements that can provide an improved creep resistance of magnesium alloys (*Hollrigl-Rosta*, 1980).

The addition of 1 % of Si leads to the formation of additional phase, intermetallic compound Mg_2Si having a high melting point (1085–1100 °C) (*Drápala et al.*, 2004). Mg_2Si phase has a face centered cubic crystal structure (*Beer et al.*, 1992). In case of low cooling rate, Mg_2Si phase is in the form of Chinese script and the alloy has a low ductility. The Mg_2Si intermetallic phase is very stable and can impede grain boundary sliding at elevated temperatures.

The castability of the AS41 alloy is relatively good unlike the AS21 alloy. This is because silicon improves the castability of AS alloys for the Al content of not less than 4 % (*Drápala et al.*, 2004). The effect of manganese is related to the removal of iron contaminations from the melt.

1.2.2 Zirconium-containing magnesium alloys

Zirconium is used in magnesium alloys for grain refinement and it is currently the only known element that has potential grain refining effects. However, zirconium cannot be used in alloys containing Al or Mn, because it forms stable compounds with Al and Mn (*Avedesian and Baker*, 1999).

The zirconium-containing magnesium alloys usually show a higher corrosion resistance in comparison with the zirconium-free magnesium alloys (*Ben-Hamu et al.*, 2007). The maximum solubility of zirconium in molten magnesium is 0.6 %, and as the binary Mg-Zr alloy does not have sufficiently hight strength in the cast state for most commercial applications, the addition of other elements is necessary.

In the as cast conditions, the alloys generally consist of α_g grains. Aging causes precipitation that occurs within the grains which improves creep resistance. This improvement can be attributed to the strengthening effect of precipitates both inside of grains and at grain boundaries, reducing grain boundary sliding.

Mg-RE-Zn alloy system

The Mg-RE-Zn alloys have as an addition rare earth elements to improve the creep resistance and zirconium to refine the grain size. Further increase of strength occurs if zinc is also added (*Ben-Hamu et al.*, 2007). The most widely used cast alloy of this system is ZE41 that has a moderate strength when artificially aged.

Extensive investigations have been focused on the phase diagram of Mg-Zn. *Luo et al.* (1993), *Tang et al.* (1993), and *Luo et al.* (1995) identified the Z phase in Mg-Zn-Y(-Zr) alloy as a stable icosahedral quasicrystalline phase (I phase), possessing unusual properties such as high hardness, high thermal stability, low friction coefficient and low surface energy, etc. *Wei et al.* (1995) and *Wei and Dunlop* (1997) concluded that the eutectic ternary phase (T phase) in Mg-Zn-MM alloy has a c-centered orthorhombic crystal structure and exhibits a wide range of stoichiometry, especially Mg52.6Zn39.5MM7.9 in Mg-8 wt.% Zn-1.5 wt.% MM alloy. *Pelcová et al.* (2007) investigated the influence of processing technology on phase transformations in a rare-earth-containing MgZnZr alloy. Also, *Li et al.* (2007) investigated the Mg-Zn-Zr alloys with different amount of Nd and Y additions. The interdendritic phases of as cast Mg-5Zn-0.6Zr alloy were comprised of a small amount of Zn_2Zr_3 and Mg_4Zn_7. When 1 wt.% Nd was added into the Mg-5Zn-0.6Zr alloy, interdendritic T phase crystallized into continuous networks in two different kinds of morphologies, ribbon-shaped precipitates and lamellar eutectics with Mg. With an increasing Nd content up to 2 wt.%, W phase formed, coexisting with T phase, and the continuous lamellar eutectics became predominant. Further addition of 0.5–1 wt.% Y into Mg-5Zn-2Nd-0.6Zr alloy led to the individual formation of W phase in the form of lamellar eutectics with Mg. There is a strong dependence of tensile properties on microstructure. The continuous networks of intergranular phases in Mg-Zn-Nd-Zr alloys significantly deteriorate the tensile strength and elongation, whereas the less continuity of intergranular phases in the Mg-Zn-Nd-Y-Zr alloys favored the tensile strength and elongation.

The potential importance of the Mg-Ag system was recognized discovering that the relatively poor tensile properties of Mg-RE-Zr alloys could be much improved by a silver addition. Substituting neodymium-rich mixtures gave a further increase in strength, and

several compositions have been developed for the applications at elevated temperatures.

The most widely used Mg-Ag cast alloy is QE22A, which has been used for aerospace applications. If the silver content is less than 2 %, the precipitation process is similar to that in Mg-RE alloys and involves the formation of Mg-Nd precipitates. However, for higher amounts of silver, two independent precipitation processes have been reported, both of which lead ultimately to the formation of the equilibrium phase with probable composition as $Mg_{12}Nd_2Ag$ (*Polmear*, 1994; *Svoboda et al.*, 2000). Maximum age hardening and creep resistance appear to be associated with the presence of $\gamma + \beta$ precipitates. The addition of silver also refines the precipitate size. QE alloys exhibit a good high temperature strength but a very poor oxidation resistance (*Polmear*, 1991).

Elevated-temperature properties can be further enhanced by the partial substitution of the RE component by thorium. The cast alloy, QH21A showed the highest values of tensile strength and creep resistance at temperatures up to 250 °C prior to the discovery of the alloys containing yttrium. It should also be noted that Mg-Y alloys, as mentioned, have the advantage of high corrosion resistance. QH21A, like the other Mg-Th alloys, is becoming out of use because of the radioactivity of thorium.

Chapter 2

Magnesium alloy based composites

A composite material is a material consisting of two or more physically and/or chemically distinct suitably arranged or distributed phases (matrix and reinforcements). In case of metal matrix, a composite is called metal matrix composite (MMC). In MMCs, the matrix phase is usually three-dimensional-continuous, whereas the reinforcement phase may be discontinuous, one-, two-, or three-dimensional. The reinforcement phase can have the shape of particles, fibres, platelets, or even consist of a continuous three-dimensional network. A variety of metals and their alloys can be used as matrix materials. The most important and commonly used are magnesium, aluminum, and titanium alloys because of their low density and other properties (*Chawla*, 1993). The aim of developing MMCs is to improve creep resistance and specific strength and to reduce the thermal expansion of the material. Therefore, there is wide interest in the microstructure investigation of thermally loaded MMCs in order to understand their behaviour in the changing temperature environments.

Internal thermal stresses in magnesium alloy based composites

When a composite is subjected to a change in temperature (with/without mechanical loading), the differences in coefficients of thermal expansion (CTE) between matrix and reinforcement will produce an internal strain mismatch and a change in the internal stress state. If changes in temperature, and/or in mechanical loading induce a phase change of one of the components, internal strain mismatch will also occur. If the strain mismatch

(thermal mismatch strain) is small, it is generally accommodated by elastic deformation, which is reversible and determined by the elastic moduli of the matrix and the reinforcement. If the strain mismatch is larger, it induces plastic deformation around fibres. For even larger strain mismatch, the entire volume of a MMC may become plastically deformed: matrix is deformed plastically while fibres are deformed (purely) elastically. Thus, plastic deformation of the matrix may occur even in the absence of an externally applied stress, and it may significantly influence mechanical properties of the composite material. The magnitude of internal stresses may be such that a temperature change induces nonreversible phenomena such as plastic yielding, reinforcement fracture, and void growth in the matrix.

Elastic deformation

If only elastic deformation of matrix and reinforcement is considered, thermal expansion at a given temperature is determined by the elastic constants and CTEs of the matrix and reinforcement, accounting for the possible presence of voids in matrix and/or at interfaces. The magnitude of thermal stresses σ_{TS} relates with the thermal expansion of composites and can be expressed in such a general form:

$$\sigma_{TS} = f(E, a_1, b_1, r_1)\,\Delta\alpha\,\Delta T, \tag{2.1}$$

where $f(E, a_1, b_1, r_1)$ is a function of the Young modulus E and geometrical parameters (a_1, b_1, and r_1), $\Delta\alpha$ is the difference in the thermal expansion coefficients of the components, and ΔT is the temperature change. The term $\Delta\alpha\,\Delta T$ refers to the thermal strain (ε_T).

Local plastic deformation

In case of local plastic deformation, different models exist for estimating the thermal stresses around reinforcements. The simplest model for estimating the magnitude of thermal stresses around particles considers a composite consisting of a sphere of the reinforcement concentric within a hollow sphere of the matrix. In a similar way as for spherical particles, the case of composites reinforced with unidirectional, continuous fibres is modelled by considering infinite coaxial cylinders. Local internal stresses are large and

inherently unstable. Thus, the relaxation of these stresses is probably a process that occurs most frequently.

In recent decades, several studies have been focused on local plastic deformation, which is an important relaxation mechanism, whereby dislocations are rearranged and/or created so as to reduce the stored energy. It is important to note that all misfit strains between an elastic inclusion and plastically deforming matrix are accommodated by a system of geometrically necessary dislocations in the matrix near the interface (*Linholt*, 1994). Complete relaxation by dislocation generation and motion leads to a reduced stress level in the composite, but not to the total removal of stress, since the configuration of these (geometrically necessary) dislocations has itself a stress field, although of low energy, such that

$$\sigma_{max} > \sigma_{complete\ relax} > 0. \tag{2.2}$$

In equation (2.2) the stresses are understood as numerical values. The individual dislocation processes have been studied in metals on a fundamental basis, in terms of energy aspects and by direct observation (electron microscopy) (*Linholt*, 1994).

Full matrix plastic deformation

Theoretical analyses of the elastoplastic deformation due to thermal loading of a metallic matrix reinforced with ceramic particles have been presented by *Lee et al.* (1980) and *Olsson et al.* (1995) using a simple concentric spheres model. According to these analyses it should be pointed out that, as the stress state in the inner sphere is purely hydrostatic, a spherical metal particle embedded in a ceramic matrix is always protected from plastic deformation. If the metal matrix surrounds a ceramic particle, the onset of yielding in the matrix is governed by the value of the effective stress in the outer sphere (*Olsson et al.*, 1995). As a consequence the effective stress has a maximum at the interface and the plastic deformation will spread outwards in the radial direction. A similar analytical analysis of the conditions for the onset of plastic yielding and for full matrix plasticity in a perfectly plastic matrix reinforced with unidirectional continuous fibres is possible on the basis of the stresses for the infinite coaxial cylinders model. The von Mises effective stress σ_{meff} has a maximum at the interface, which means that yielding starts there and

extends outwards in the matrix cylinder. *Vedula et al.* (1988) used the Tresca criterion to estimate the temperature drop for the onset of plasticity in a unidirectional aluminum-graphite composite. *Yano et al.* (1988) and *Dumant et al.* (1988) reported that full matrix plasticity will be reached quite quickly after the onset of yielding at the interface. The dislocation density gradient will tend balance the continued thermal loading (*Delannay*, 2000).

Chapter 3

Evidence on microstructure of plastically deformed Mg alloys and its composites

3.1 Deformation modes in magnesium alloys

This section is an overview on the activity of different slip systems ($<a>$, $<c+a>$, and $<c>$ dislocations) of plastically deformed Mg based alloys as observed by TEM. The investigations were most intensively carried out on AZ series magnesium alloys, and some examples will be given in this section to demonstrate this series of alloys.

It is well known that the activity of any slip system depends on its critical resolved shear stress (CRSS). According to the results of *Stohr and Poirier* (1972) and *Obara et al.* (1973), the CRSS for a basal slip system with a direction of $1/3<11\bar{2}0>$ (or $<a>$-type dislocations) at room temperature is much lower than those of the non-basal slip systems on prismatic and pyramidal planes. It means that the activity of a non-basal slip system requires a higher stress. *Koike et al.* (2003a,b) reported the activity of non-basal (prismatic) $<a>$ slip during room temperature deformation of AZ31 extruded alloy by directly observing dislocations using TEM. They suggested that strain compatibility at grain boundaries was responsible for the enhanced cross slip of $<a>$ dislocations from basal to non-basal planes (*Koike et al.*, 2003a) as well as grain-boundary sliding (*Koike*

et al., 2003b). *Kobayashi et al.* (2003) also showed that the region affected by the strain compatibility was restricted to several μm from grain boundaries, which resulted in the grain-size dependence on the relative extent of non-basal slip to basal slip. The activation of prismatic $<a>$ slip may be attributed to the localized inhomogeneous stressing caused by various constraints imposed on a grain by its neighbors (*Koike and Ohyama*, 2005). These authors have also reported that prismatic $<a>$ slip is responsible for a relatively good tensile ductility in AZ61 magnesium alloy. As mentioned in Section 3, twinning is another principle deformation mode in magnesium alloys at room temperature. An extensive twinning in AZ31 Mg alloy deformed at room temperature (as opposed to 200 °C) was observed by *Janeček et al.* (2007a). This is in good agreement with the results obtained from acoustic emission (AE) investigations (*Máthis et al.*, 2006; *Meza-García et al.*, 2007; *Hellmig et al.*, 2007). In addition to its temperature dependence, twinning also depends on grain size and solute atom content (*Bohlen et al.*, 2007).

The CRSS for the non-basal slip systems of Mg and its alloys depends significantly on testing temperature, decreasing rapidly with increasing temperature (*Trojanová and Lukáč*, 2005). For example, *Somekawa et al.* (2003) observed by TEM $<c+a>$ dislocations in AZ31 alloy after the thermo-mechanical treatment at 573 K . The increased activity of non-basal, $<c+a>$ dislocations provides an explanation for the observed changes in the strain rate sensitivity, anisotropy and texture evolution with increasing temperature. Thus $<c+a>$ slip appears to be the mechanism responsible for the improved formability of magnesium alloys at elevated temperatures (*Agnew and Duygulu*, 2003). *Máthis et al.* (2004) studied the evolution of non-basal dislocations as a function of deformation temperature in pure magnesium determined by X-ray diffraction. They found that at higher temperatures the fraction of $<a>$ dislocations decreases, whereas the fraction of $<c+a>$ dislocations increases, which is in agreement with TEM observations. The fraction of $<c>$ dislocations remains practically unchanged and very low. The source of $<c>$ dislocations is determined to be either a dissociation of $<c+a>$ dislocations (*Agnew et al.*, 2002) or a reaction between $<c+a>$ and $<a>$-type dislocations (*Agnew and Duygulu*, 2005; *Balík et al.*, 2007). The activity of the $<c+a>$ slip in Mg-Li single crystals was also found to increase with increasing Li concentration (*Ando and Tonda*, 2000). *Agnew et al.* (2002) investigated textured polycrystalline samples of pure Mg and Mg-15

at. pct Li for the presence of $<c+a>$ dislocations by TEM after 1 to 3 pct deformation, which forced the majority of grains to compress along their c-axis. The higher density and more uniform distribution of $<c+a>$ dislocations in the Li-containing magnesium alloy were observed compared to pure Mg. This supports that Li additions promote the activity of these dislocations. Because the $1/3<11\bar{2}3>\{11\bar{2}\bar{2}\}$ pyramidal slip mode together with the basal slip offers five independent slip systems, it provides a satisfying explanation for the enhanced ductility of Mg-Li alloys. An enhanced activity of pyramidal $<c+a>$ slip in Mg-Li alloys was also observed using X-ray diffraction techniques (*Agnew et al.*, 2001).

Koike and Ohyama (2005) investigated the texture effect on the active slip systems in rolled Mg sheets and tried to provide a geometrical criterion for the activation of the non-basal slip systems. The basal-plane tilt angle was considered as a geometrical criterion for the activation of the prismatic $<a>$ slip at room temperature. *Agnew et al.* (2001, 2002) demonstrated by TEM that the $<c+a>$ dislocations play an important role in the texture evolution of Mg alloys. An analysis of texture evolution showed that the critical role that $<c+a>$ dislocations play in the deformation texture evolution of Mg alloys (*Agnew et al.*, 2003), and the enhanced secondary slip deformation was rationalized in terms of the source and mobility issues on $<c+a>$ dislocations for the pyramidal slip (*Tonda and Ando*, 2002; *Agnew et al.*, 2003; *Ando et al.*, 2003). *Yi et al.* (2006) analyzed the mechanical behaviour of AZ31 alloy in tension at various temperatures and the accompanying texture evolution. The activity of the non-basal slip systems were investigated using synchrotron X-ray diffraction and electron backscatter diffraction (EBSD). Texture components corresponding to a high activation of $<c+a>$ slip systems were observed above 200 °C. We can conclude that the activity of non-basal slip systems is significant for the deformation behaviour of Mg alloys.

3.2 Dislocation evolution in the plastically deformed Mg alloy based composites

The plastic deformation behaviour of MMCs is influenced by both reinforcement phases and matrix properties. There is a strong interest in understanding the role of dislocations in MMCs, mostly because they control the plastic behaviour of the matrix phase and thus play a significant role in the mechanical response of MMCs. It is well documented that, if the thermal stresses are high enough, new dislocations are generated in MMCs near fibres, whiskers or particles. For instance, an increase in the dislocation density in the matrix after thermal cycling of Al-SiC composites was demonstrated by *Arsenault and Fisher* (1983). *Vogelsang et al.* (1986) investigated the dislocation generation in 6061 Al alloy MMC reinforced with 20 vol.% SiC whiskers under thermal cycling using in situ TEM observations. *Barlow and Hansen* (1995) studied Al/SiCw under applied load and thermal cycling using TEM. Investigation of misorientations around whiskers in a MMC has demonstrated the presence of plastic strain fields which are supported by arrays of dislocations. A high density of dislocations generated by the thermal stresses has been demonstrated during thermal cycling of SiC particle reinforced magnesium alloy QE22 and Mg composites using acoustic emission (AE) technique (*Lukáč et al.*, 1995; *Kiehn et al.*, 1997; *Chmelík et al.*, 1998, 2002).

It is therefore important to understand how the presence of reinforcing phases affects the dislocation behaviour in the matrix, the microstructure (dislocation geometry, density, and evolution), and the properties (effect of dislocations on mechanical properties). TEM has revealed a variety of dislocation configurations surrounding the reinforcing phases, including long dislocations along fibres, dislocations emitted at whisker end and corners as well as various loops and tangles (*Calhoun and Dunand*, 2000). Two main types of thermal mismatch dislocation structures have been observed in MMCs: rows of prismatic loops and dislocation tangles. Loop shape is affected by the residual stress field of the reinforcement or by other long-range sources (*Calhoun and Mortensen*, 1999). Complex tangles of dislocations are almost always observed in MMCs with differently shaped reinforcements and large misfit strains, a result of entanglement between dislocations emitted from a particle, its neighbors, and statistically stored matrix dislocations created during

plastic deformation (*Calhoun and Dunand*, 2000). *Kim et al.* (1990) studied by TEM the dislocation structures in the 2024 aluminum alloy matrix reinforced with small SiC particles 0.8 μm in diameter, and large SiC particles 7.4 μm in diameter. They found that the reinforcement size influences the dislocation interaction. Small particles punch only a small number of dislocations while large particles punch large number of dislocations of various shapes. Many studies of the dislocation density have been done. For instance, *Kim et al.* (1990) measured the dislocation densities as a function of distance from the reinforcement and found that the dislocation density is highest near the reinforcement. *Arsenault et al.* (1991) measured the dislocation densities in Al/SiC composites and found that the dislocation densities increased with reinforcement volume fraction and with decreasing particle size over the range of 0.5–250 μm.

Together with experimental investigations of dislocations, models predicting dislocation structure evolution and dislocation impact on properties are widely proposed. These models are mainly based on a suggestion that lattice dislocations are forced, by the microstructural constraint, to bow out or pile up, and their movement requires an external stress dependent on microstructural parameters (*Kouzeli and Mortensen*, 2002). *Barlow and Liu* (1998) studied matrix orientations around whisker reinforced MMCs and applied a dislocation-array model in order to explain some of the discrepancies in continuum models. *Kouzeli and Mortensen* (2002) investigated the particle size dependence of the flow stress in infiltrated particle reinforced aluminium composites $Al_2O_3 - Al$. The authors showed that the flow stress in these composites is a strong function of the interparticle distance, increasing with decreasing interparticle distance. The thermophysical properties of the reinforcements also influence the tensile flow behaviour. The concept of geometrically necessary dislocations is combined with a continuum mean-field approach in order to rationalize the experimental data (the effects on the yield behaviour of the composites).

3.3 Thermally activated processes in magnesium alloys and its composites

Motion of dislocations in polycrystals is affected by different types of obstacles as it was shown in previous two sections. The applied stress σ necessary for deformation of polycrystals is usually divided into two components (e.g., *Caillard and Martin*, 2003):

$$\sigma = \sigma_i + \sigma^*, \tag{3.1}$$

where σ_i is the internal stress (athermal component) and σ^* is the effective stress. In polycrystal materials, the applied stress is related to the resolved shear stress (τ) and its corresponding components by the Taylor factor ψ: $\sigma = \psi\tau$. The resolved shear stress necessary for the dislocation motion in the slip plane can be divided as $\tau = \tau_i + \tau^*$ (*Trojanová et al.*, 2007a), where τ_i is athermal contribution to the stress, resulting from long-range internal stress impending the dislocation movement, and τ^* is the effective shear stress which acts on dislocations during their thermally activated motion by overcoming short-range obstacles.

In a composite, the athermal component includes two components, in particular the stresses necessary for deformation due to the load transfer, σ_{LT}, and σ_i^D the stress necessary for generation of dislocations, their movement and storage (*Trojanová et al.*, 2007b). The flow stress σ_{LT} necessary for composite deformation due to the load transfer can be calculated as (*Aikin and Christodoulu*, 1991):

$$\sigma_{LT} = \sigma_m \left[1 + \frac{(L + d_t)A}{4L}\right] f + \sigma_m(1 - f), \tag{3.2}$$

where σ_m is the yield stress of the matrix, f is the volume fraction of fibres, L is the fibre size in the direction of the applied stress, d_t is the fibre size in the perpendicular direction and A is the fibre aspect ratio (L/d_t). The model is based on the simplifying assumption of uniform matrix deformation and it yields therefore a very simplified expression for stiffness and strength contribution. The internal stress σ_i^D resulting from long-range internal stresses impeding the dislocation movement may be expressed as (*Trojanová et al.*, 2007b):

$$\sigma_i^D = \gamma G b \Delta\rho^{1/2}, \tag{3.3}$$

where γ is a constant describing the interaction between dislocations; G is the shear modulus; b is the Burgers vector of dislocations; $\Delta\rho$ is the total dislocation density. The effective shear stress σ^* acts on dislocations during their thermally activated motion when they overcome short range obstacles. The mean velocity of dislocations v is connected with the plastic strain rate by the Orowan equation:

$$\dot{\varepsilon} = (1/\psi)\rho_m b v, \tag{3.4}$$

where ρ_m is the density of mobile dislocations and ψ is the Taylor factor. The plastic strain rate $\dot{\varepsilon}$ for a single thermally activated process can be expressed as:

$$\dot{\varepsilon} = \dot{\varepsilon}_0 \, exp[-\Delta G(\sigma^*)/kT], \tag{3.5}$$

where $\dot{\varepsilon_0}$ is a pre-exponential factor containing the mobile dislocation density, the average area covered by the dislocations in every activation act, the Burgers vector, the vibration frequency of the dislocation line, and the geometric factor. T is the absolute temperature and k is the Boltzmann constant. $\Delta G(\sigma^*)$ is the change in the Gibbs free enthalpy depending on the effective stress $\sigma^* = \sigma - \sigma_i$ and its simplest form is

$$\Delta G(\sigma^*) = \Delta G_0 - V\sigma^* = \Delta G_0 - V(\sigma - \sigma_i). \tag{3.6}$$

Here ΔG_0 is the Gibbs free enthalpy necessary for overcoming a short range obstacle without the stress and $V = bdL_c$ is the activation volume, where d is the obstacle width and L_c is the mean length of dislocation segments between obstacles. The nature and the distribution of obstacles determine the activation parameters (activation volume and activation energy). For a given arrangement of obstacles in a material, the thermally activated process determines the temperature and strain rate dependence of the flow stress. The activation volume is needed to identify the thermally activated mechanisms (various kinds of thermally activated processes, e.g. crossing the dislocation forest, overcoming the Peiers-Nabarro stress, nonconservative motion of screw dislocations, interaction between the dislocation and point obstacles, climb of edge dislocations, cross slip, etc.). Stress relaxation (SR) tests are very often used for the estimation of the parameters of dislocation moion (e.g., *Trojanová et al.*, 2007a).

Chapter 4

The aims of the thesis

Magnesium alloys and their composites have attractive properties such as low density, high specific strength and stiffness, excellent castability, good dimensional stability, and high damping capacity. These properties are controlled by the material microstructure/substructure. Therefore, understanding the links between the microstructure and properties of materials can lead to improvement of their properties and to new applications of the materials. In this thesis, microstructure of selected magnesium alloys and composites has been investigated by TEM. The main investigated topics can be divided as:

(i) microstructure and substructure after the thermal and mechanical loading (AS21 and AZ31 alloys and AS21 composite);

(ii) microstructure and substructure evolution after rolling and ECAP (AZ31 and AZ61 alloys);

(iii) microstructure and substructure after thermo-mechanical treatment (ZRE1[1] and QE22 alloys). The selected alloys are attractive materials for many structural applications.

The first topic is focused on the influence of thermal history on substructure of the thermally and mechanically loaded alloys and composites: investigations of the thermally activated processes and dislocation density; estimation of the internal stresses by the SR tests; evolution of the dislocation structure with strain at various deformation temperatures. The second topic includes the study of the influence of plastic deformation on the substructure evolution of the wrought alloys and, in particular, the comparison of the

[1] Another abbreviation for ZRE1 alloy is EZ33 (according to ASTM).

internal structure of the rolled and ECAPed alloys and the evolution of the dislocation structure. The third topic is focused on the investigation of the microstructural conditions for superplastic properties in thermo-mechanically treated alloys.

Chapter 5

Experimental methods and materials

In this work, transmission electron microscopy (TEM) was used for observation of material substructures of magnesium alloys and composites. Additionally, a basic method for the microstructure observations — the light microscopy (LM) — was used to examine the general structure, to distinguish phase structures of specimens, and to estimate grain sizes and the fibre distribution in composites. Measurement of Vickers microhardness (HV) was applied on selected magnesium alloys. Deformation tests of samples were carried out on an Instron testing machine.

5.1 Electron microscopy

Applications of materials is based on their properties such as strength, toughness, electric and thermal conductivity, and numerous others. All these properties depend on the internal structure of materials. Structural features of materials include their atomic and electronic structure, local configuration of atoms, and arrangements of these configurations in the microstructure. The structure characterization on all spatial scales is often best estimated by TEM, which is based on the interaction between high energy electrons and atoms (or arrays of atoms) in solids. The unique role of TEM is given by the fact that electrons are charged particles, and therefore, unlike X-rays or neutrons, they may be accelerated and precisely focused by electromagnetic fields. The scattered beams can be collected by a lens, and refocused to form a true real space image, where each point in the image corresponds to a specific point in the object. Electrons also interact much more

strongly with matter and electron diffraction can be performed on materials of nanometer dimensions.

5.1.1 Contrast initiation and imaging modes in TEM

The electron wave, which can be expressed in the form of a plane wave $\Psi = \Psi_0 \exp(2\pi i k_0 r)$ (Ψ_0 is the wave amplitude, k_0 is the wave vector magnitude, r is the position vector), can change its amplitude and phase as it traverses the specimen. These changes can give rise to the "image contrast" in TEM. In most situations, both types of contrast actually contribute to the image, although the amplitude contrast dominates.

A fundamental distinction between the amplitude and phase contrasts in TEM can be made. Amplitude contrast is seen if a single beam is selected while phase-contrast is seen if more than one beam contribute to the imaging. In general, the more beams collected, the higher the resolution of the image. Thus, phase contrast is often thought to be synonymous with high resolution TEM. In TEM, phase contrast appears at relatively low magnification as moiré fringes and Fresnel contrasts.

There are two principal types of the amplitude contrast, namely the mass-thickness contrast and the diffraction contrast. The mass-thickness contrast is the most important for the observation of polymers and it is also the critical contrast mechanism for biological specimens. The diffraction contrast arises in crystalline specimens such as metals and composites (*Williams and Carter*, 1996) and it will be discussed in detail in the following chapter.

In general, the contrast (C) may be defined quantitatively in terms of difference in intensity (I) between two adjacent areas:

$$C = \frac{(I_1 - I_2)}{I_2} = \frac{\Delta I}{I_2}. \tag{5.1}$$

TEM contrast is seen as different levels of intensity on the viewing screen and as different gray levels on the photograph. Both strong and weak contrasts can be obtained. Figure 5.1 shows dependence of the contrast on the intensity of incident electrons. The strongest contrast is generally obtained under illumination conditions that lower the total intensity, while an increase of the number of electrons falling on the screen, by condensing the

beam onto a reduced area of the specimen, usually decreases the image contrast (*Williams and Carter*, 1996).

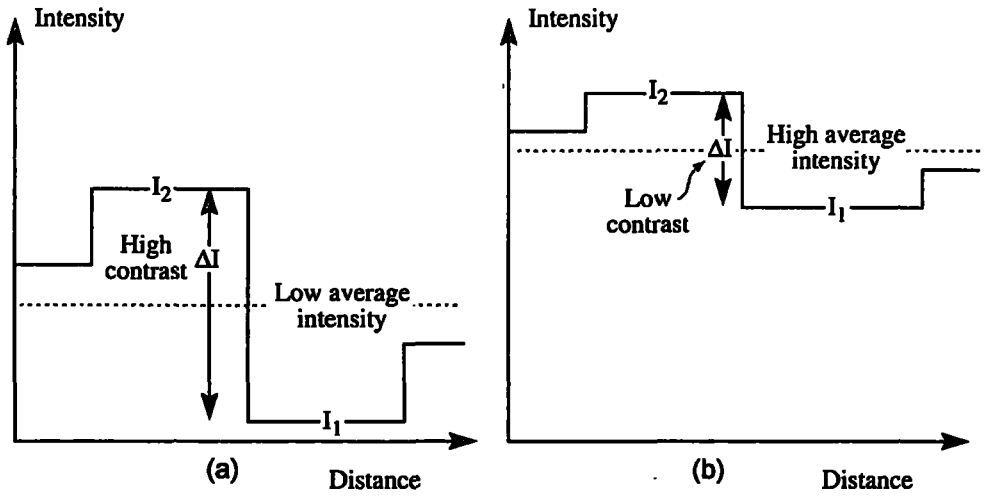

Figure 5.1: Schematic intensity profiles across an image: (a) high contrast for low average intensity; (b) low contrast for high average intensity (*Williams and Carter*, 1996).

Amplitude contrast in TEM images is obtained by selecting specific electrons or excluding them from the imaging system. Using the diffraction, it is possible to form two types of amplitude contrast, either bright field (BF) or dark field (DF) selecting direct or scattered electrons, respectively, by the objective aperture. Figure 5.2 shows diffraction patterns (DP) from an Al single-crystal with a schematic indication of the objective aperture. In this figure, the aperture in the position A is selecting the direct beam only and thus a BF image will be formed in the image plane of the lens (Figure 5.3a). Such arrangement will produce amplitude contrast in specimen whether the specimen is crystalline or amorphous. If the aperture is in the position B, it will select only electrons scattered in that specific direction. In Figure 5.3b the electrons selected by the aperture travel off the axis since the aperture is displaced to select the scattered electrons. These off-axis electrons suffer aberrations and astigmatism and the DF image is difficult to focus. To avoid this, the beam tilt coils above the objective lens should be adjusted so that the incident beam hits the specimen at an angle equal and opposite to the scattering angle. In this way the scattered electrons travel down to the optic axis, as shown in Figure 5.3c. This operation is called centered dark field (CDF) imaging and it is the way of DF imaging in TEM, if

one needs to record the best, focused image (*Williams and Carter*, 1996).

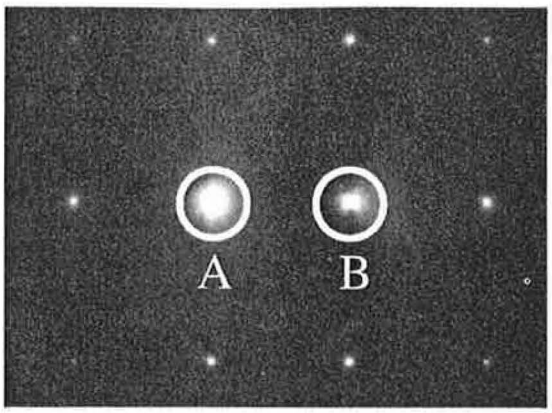

Figure 5.2: The relationship between the objective aperture and the diffraction pattern for forming BF (A) and DF (B) images (*Williams and Carter*, 1996).

The electron image (BF or DF) obtained in this way is a highly magnified image of the variation in the intensity of the selected beam across the bottom surface of the crystal. Contrast in the BF image arises, therefore, if the intensity of the direct beam varies significantly from one region of the specimen to another, and corresponding variations will generally be obtained in the DF image. Contrast in BF and DF TEM images is usually "diffraction contrast". Diffraction contrast is simply a special form of amplitude contrast.

5.1.2 Diffraction contrast

Diffraction-contrast imaging is realized if the intensity in a diffracted beam depends strongly on the deviation parameter and crystal defects distort the diffracting planes. Therefore, the diffraction contrast from regions close to a defect depend on the properties (in particular, the strain field) of the defect. The mechanism of diffraction contrast is visible from the schematic diagram in Figure 5.4. The edge dislocation shown in this figure will bend the crystal planes, so that the Bragg condition for diffraction is locally satisfied. The intensity of the direct beam leaving the crystal is therefore reduced to a greater extent in this part of the crystal than in the regions remote from the dislocation which do not diffract as strongly. Thus, for the simple diagram shown it could be expected that the amplitude of the diffracted beam at the exit surface of the crystal would be

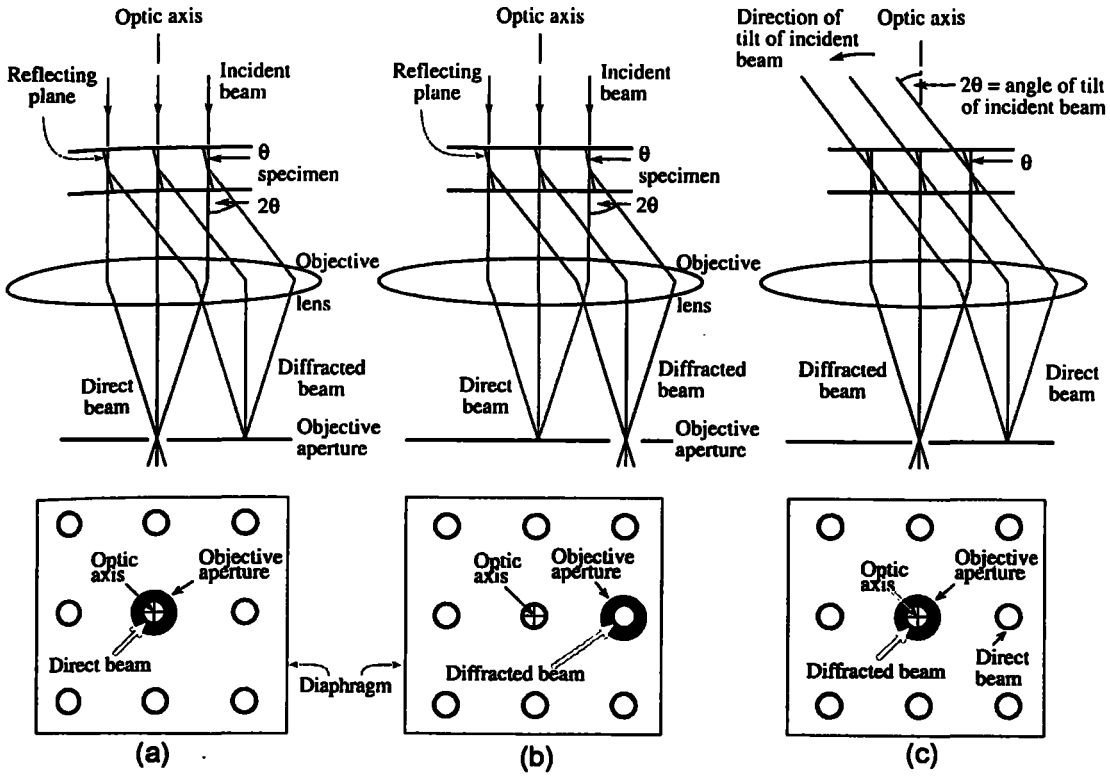

Figure 5.3: Diagrams showing how the objective lens/aperture are used in combination to produce (a) a BF image formed from the direct beam, (b) displaced-aperture DF image formed with a specific off-axis scattered beam, and (c) CDF image where the incident beam is tilted so that the scattered beam remains on axis. The area selected by the objective aperture, as seen on the viewing screen, is shown below each diagram (*Williams and Carter*, 1996).

small everywhere except in the region close to the dislocation where the amplitude would be large. The diffraction lens magnifies the information contained in the first image. Thus, the final image obtained from a specimen will be the representation of the variation in intensity of the electrons leaving the crystal in the direction defined by the beam selected by the objective aperture. In Figure 5.4 it can be seen that the image formed in bright field would show a dark line associated with the image of the dislocation line and conversely, that the dark-field image will be a bright line. The figure also shows that the image that is observed when using the technique of diffraction contrast depends on the orientation of the crystal, i.e. on the diffraction conditions. Thus, if the observed contrast is to be interpreted correctly it is essential that the crystal orientation and diffraction conditions be accurately defined.

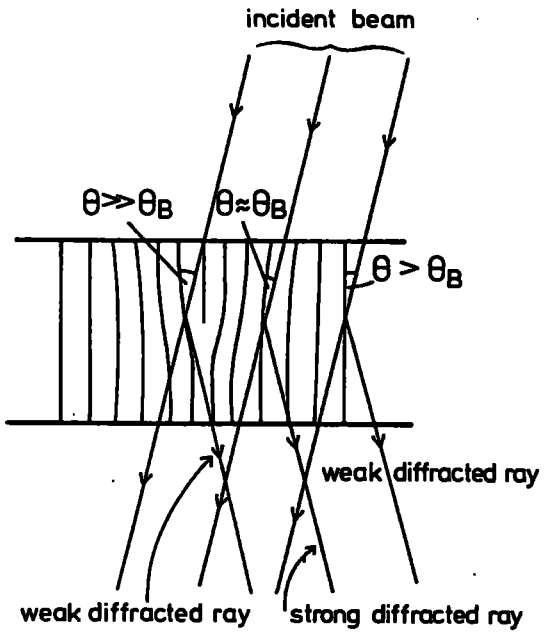

Figure 5.4: Schematic diagram illustrating the mechanism of diffraction contrast (*Loretto and Smallman*, 1975).

Two-beam condition

Two-beam condition for the creation of the good strong contrast in the BF and DF images exists. For this, only one diffracted beam is necessary to be strong. The direct beam is the

only other strong spot in the pattern. Two-beam condition is realized by specimen tilting. Figure 5.5 shows examples of correct contrast. In Figure 5.5a, Al_3Li precipitate phase seen as tiny spheres in the grain and coarse lamellae at the boundary is diffracting strongly and appears dark. In Figure 5.5b, showing a precipitate spot, only diffracting precipitates appear bright. Thus, two-beam condition is not only necessary for good contrast but it also greatly simplifies the interpretation of the images.

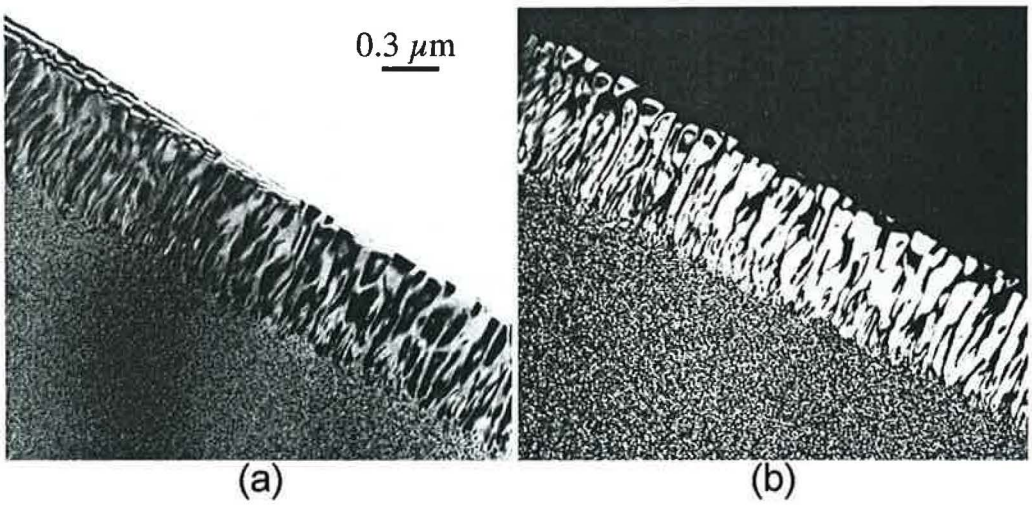

Figure 5.5: Al_3Li precipitate phase imaged in BF (a) and in DF (b) (*Williams and Carter*, 1996).

Thickness and bending effects

Diffraction contrast is observed both in crystals with defects and in perfect crystals for two reasons: either the thickness of the specimen varies or the diffraction conditions change across the specimen. When the thickness of the specimen is not uniform, the coupling of the direct and diffracted beams occurs over different distances, thus producing a thickness effect. Whenever the orientation of the diffracting planes changes, i.e. when the diffracting planes bend, the contrast changes, and producing consequently the bending effect. Therefore, the bending may arise in thin specimens or it may be caused by strains which are present in the bulk material. Consequently, in a real specimen, bending and thickness effects often occur together. These two contrast phenomena are called "bend contours" and "thickness fringes", respectively.

Contrast on defects

If the beam is exactly parallel to any zone axis then, according to the Laue conditions, there should be no spots in the diffraction pattern. However, in reality there are many spots, so the diffracted beams appear even when the Bragg condition is not exactly satisfied. The actual intensity will depend on how far the diffracted beams are from the Bragg condition. This distance is measured by a vector s in reciprocal space such that

$$K = g + s, \tag{5.2}$$

where K is the vector of scattering which represents a change in the wave vector k due to diffraction, g is the vector of reciprocal space.

Hence, to get the best contrast from defects the specimen should not be exactly at the Bragg conditions ($K = g$, $s = 0$) as shown in Figure 5.6a. If s is small and positive (the excess hkl Kikuchi line is just outside the hkl spot), this will give the best possible strong-beam image contrast, as in Figure 5.6b. If s increases further, as shown in Figure 5.6c, the defect images become narrow but the contrast is reduced.

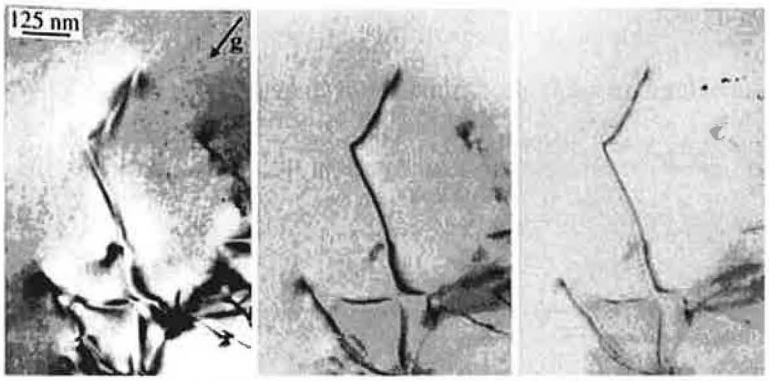

Figure 5.6: Variation in the diffraction contrast when s varies from (a) zero to (b) small and positive and (c) larger and positive (*Williams and Carter*, 1996).

5.2 Methods of thin film preparation for TEM

Specimens for TEM must be thin enough (less than 100 nm) to transmit a sufficient number of electrons and to provide sufficient intensity on the screen or film, and consequently

to give an interpretable image. All methods of thin film preparation for TEM observations consist of two steps: mechanical thinning and final thinning that makes the plates gloss and transparent for electrons. The choice of the final thinning method depends on the purpose of the study and the physical characteristics of the material (whether it is soft or hard, ductile or brittle, single-phase or a composite, etc.) Two main methods of final thinning — electropolishing and ion milling — were used for our magnesium specimens.

5.2.1 Mechanical thinning

The mechanical thinning involves three parts: thinning to make a slice of material between 100 μm and 200 μm, cutting the 3 mm disk from the slice, and prethinnig the central region of the disk from one or both sides to a few micrometers. Microstructure of the investigated specimens must not be damaged during the preparation of thin films. Therefore, very careful preparation is needed. Also, for preparation of thin foils from magnesium specimens, we took into account a soft nature of the magnesium matrix, the fact that magnesium readily reacts with water, and the hardness of intermetallic phases in the AS21 magnesium based composite. All investigated samples were cut by the diamond saw to the thickness of 1 mm and thinned on both sides manually using SiC paper of different grains (600, 800, 1000, and 1200). Finally, the specimens were washed in ethanol.

5.2.2 Electropolishing

Electropolishing is the method that can only be used for electrically conducting samples such as metals and alloys. This method can produce foils without mechanical damage but it may change specimen surface chemistry. Therefore, it is necessary to choose an electrolyte thinning specimen and glossing its surface simultaneously. During electropolishing the electrolyte current is jetted on the disc specimen and preferentially thinned the center of the disc (Figure 5.7). The specimen is held in a Teflon holder and embedded into the electrolyte (*Smola*, 1983). The polishing is stopped when a hole is created, which is detected by laser beam or light sensor. Usually, the transparent area near the hole is used for the TEM observations.

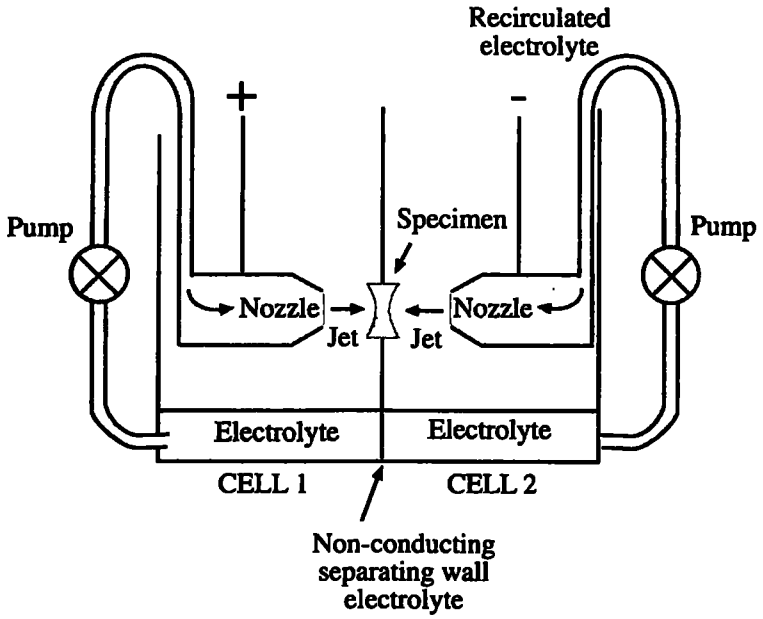

Figure 5.7: Schematic of a twin-jet electropolishing apparatus (*Williams and Carter*, 1996).

The conditions for obtaining the good polished surface require the formation of a viscous film between the electrolyte and the specimen surface (Figure 5.8). The electropolishing curve in this figure shows the current increase between the anode and cathode as the applied voltage increases. The polishing occurs on the current plateau. The thick viscous layer provides rough polishing on the surface while the thin layer on the surface provides for fine polishing. The plateau on the curve of the voltage dependence of current expands with increasing temperature. At the formation of the hole, the electrolyte flow must be cut off immediately to prevent loss of thin area, and the disc must be rapidly removed from the electrolyte and washed in solvent to remove any residual electrolyte film that may etch the surface. For the electropolishing the following parameters should be set: temperature, electrolyte solution chemistry, stirring rate, applied voltage, and polishing current.

5.2.3 Ion milling

Ion milling involves bombarding of thin TEM specimen with energetic ions or neutral atoms and sputtering material of thin film until it is thin enough to be studied in TEM. The parameters which need to be controlled include voltage, temperature of the speci-

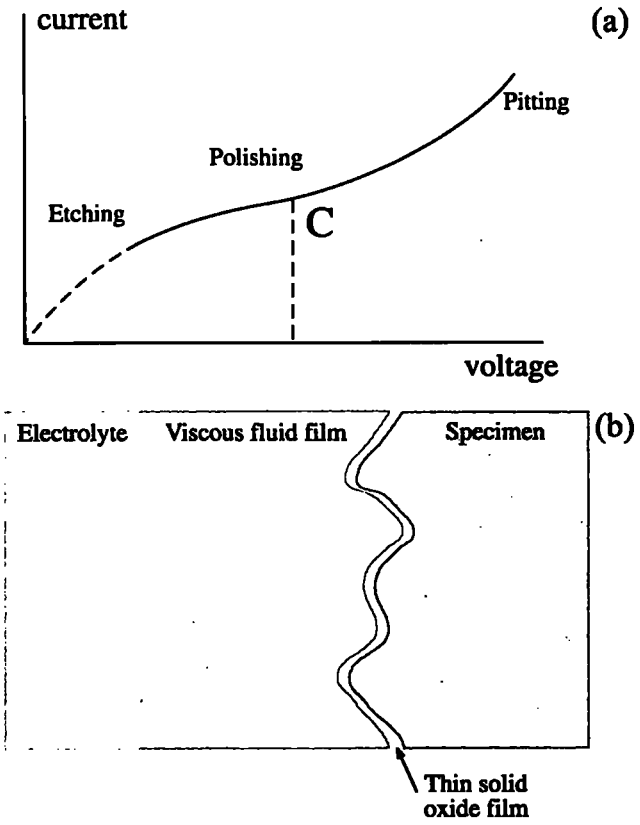

Figure 5.8: Dependence of current between the anode and cathode on the applied voltage (*Williams and Carter*, 1996).

men, the nature of the ion (Ar, He), and the geometry (the angle of incidence). Most of the thinning parameters are generally fixed except for the ion energy, the angle of ion incidence, and the rotation rate and the temperature of the specimen. An accelerating voltage of 4–6 kV is usually used. The ion beam will always penetrate the specimen to some extent, while can be minimized by inclining the incident ion beam with respect to the surface of the specimen. Ar is mostly used because it is inert, heavy and not naturally present in most samples. The effect of incidence angle on the thinning process is shown in Figure 5.9. High incidence angles promote implantation, which is undesirable. The rate of thinning reaches maximum at $\sim$ 20° incidence, above which the beam penetrates rather than sputters the sample surface. The initial thinning should start at 20–30° and reduces to less than 5° as perforation approaches. Cooling of the specimen is recommended for almost all materials; otherwise, it is possible that the ion beam might heat it up to 200 °C or higher. The specimen is usually rotated during thinning to incline the grooves which run in certain directions.

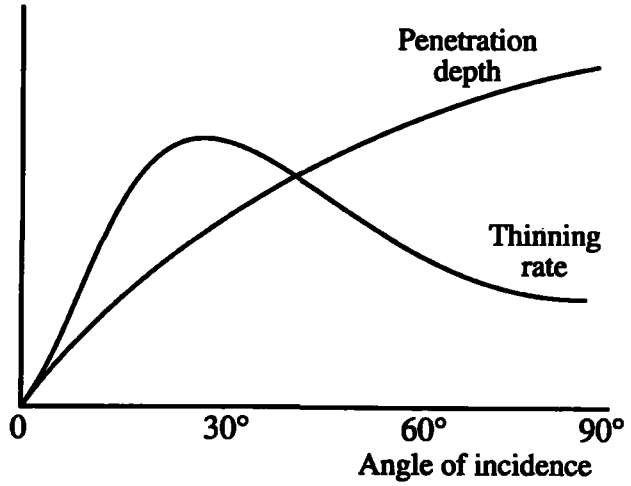

Figure 5.9: Variation in ion penetration depth and thinning rate with the angle of incidence, schematically (*Williams and Carter*, 1996).

Schematic diagram of a simplified model of ion milling apparatus is shown in Figure 5.10. Two ion guns are usually available to thin from each side. Ar gas is blown into an ionization chamber where a potential up to 6 keV creates a beam of Ar ions that impinge on a rotating specimen. The whole apparatus is under vacuum. The specimen may

be cooled by liquid N_2 and the perforation is detected by the penetration of ions through the specimen.

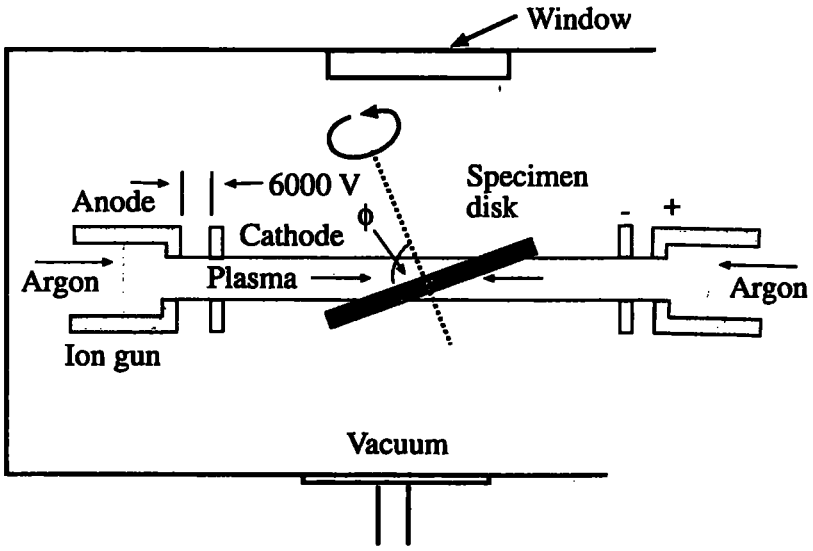

Figure 5.10: Schematic diagram of a ion-beam thinning device (*Williams and Carter*, 1996).

Ion milling is the most versatile thinning process, being used for ceramics, composites, alloys, and many cross-section specimens. Operation of the following devices depends on this method: Precision Ion-Milling System (PIMS) and Precision Ion-Polishing System (PIPS). The PIMS is useful for prethinned specimens where it is possible to locate a very small area ($\sim$ 1 μm $\times$ 1 μm) that needs further thinning. The PIPS combines high-powered ion guns and a low angle of incidence (4°) to thin one side of a specimen with minimum surface damage and heating. The low incidence angle removes any surface roughness and differential thinning problems, while the high-power guns ensure reasonable thinning rates.

5.3 Stress relaxation method

The SR technique is a very useful method to study the thermally activated processes, internal stresses, and to reveal the dominant process occurring during plastic deformation of polycrystalline and composite materials. The principle of SR tests (Figure 5.11) is

as follows. The specimen is deformed to a certain stress σ_0, at which the machine is stopped. The stress starts to decrease with time t. Subsequently, the specimen is reloaded and deformed to a higher stress (strain) and the relaxation is repeated. The time derivative

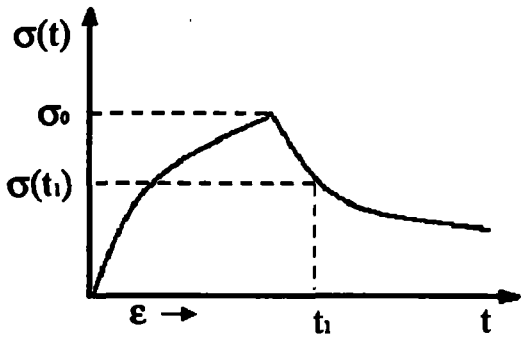

Figure 5.11: Scheme of the stress relaxation test.

$\dot{\sigma} = d\sigma/dt$ is the stress relaxation rate and $\sigma = \sigma(t)$ is the flow stress at time t during the SR. The stress relaxation tests are very often analysed under the assumption that the SR rate is proportional to the strain rate $\dot{\varepsilon}$, according to the following relation (*Dotsenko*, 1979):

$$\dot{\varepsilon} = -\dot{\sigma}/M, \tag{5.3}$$

where M is the combined modulus of the specimen machine set. The stress decrease with the time during the SR can be described by the well known Feltham equation (*Feltham*, 1963):

$$\Delta\sigma(t) = \sigma(0) - \sigma(t) = \alpha \ln(\beta t + 1), \tag{5.4}$$

where $\sigma(0) \equiv \sigma_0$ is the stress at the beginning of the stress relaxation at time $t = 0$, β is a constant, and

$$\alpha = \frac{kT}{V}. \tag{5.5}$$

The SR curves were fitted to the power law function in the form:

$$\sigma - \sigma_i = [a\beta\,(m-1)]^{1/1-m}\,(t + t_0)^{1/1-m}, \tag{5.6}$$

where t_0 is a model constant. SR tests were performed in an Instron 1186 machine at increasing flow stresses during the compression tests. The duration of all SR tests was 300 seconds.

5.4 Microhardness testing

Microhardness testing is an indentation method for measuring the hardness of a material on a microscopic scale. The indentations are made by a square-based pyramid at indenter (Vickers hardness) or an elongated, rhombohedral-shaped indenter (Knoop hardness). We used the Vickers microhardness indenter.

The hardness according to the Vickers is presented as a ratio of trial load F to the indentation surface area, which is a rectilineal tetragonal pyramid with diagonals $d1$ and $d2$ and with the vertex angle equal to the indenter angle (Figure 5.12). The following equation was used for the calculation of hardness:

$$HV = \frac{2\,F\,sin\frac{136^\circ}{2}}{d^2}; \quad HV = 1.854\,\frac{F}{d^2}\,approximately, \tag{5.7}$$

where F is the load [Kg], d is the arithmetic mean of the two diagonals, $d1$ and $d2$ [mm].

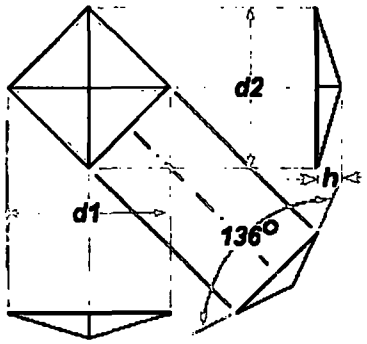

Figure 5.12: Vickers pyramid diamond indenter.

The surface being tested generally requires a metallographic polishing. Precision microscope was used to measure the indentation; it had a magnification of around 500 and measured with an accuracy of $\pm 0.5\mu$m.

5.5 Experimental materials

The squeeze cast AS21, QE22, ZRE1 magnesium alloys and AS21 composite, the rolled AZ31 sheets, and the wrought AZ31 and AZ61 alloys were used for the investigation. The nominal compositions of the alloys are shown in Table 5.1. The AS21 composite

was reinforced with 25 vol.% of Al_2O_3 short fibres (Saffil). The mean diameter of Saffil fibres and the mean length was 3 μm and 87 μm, respectively. Fibres exhibited 2D plane arrangement (Figures 5.13a,b). Fibres plane was parallel to the longitudinal axis of the samples.

Table 5.1: Nominal compositions of AS21, AZ31, AZ61, QE22, and ZRE1 magnesium alloys, %.

Alloy	Al	Mn	Zn	Si	Cu	Fe	RE	Zr	Ag	Nd
AS21	2			1						
AZ31	3	0.2	1							
AZ31 wrought	2.96	0.09	0.23							
AZ61 wrought	5.92	0.15	0.49	0.037	0.003	0.007				
ZRE1		< 0.03	2.5	< 0.01	0.01	0.003	3.1	0.6		
QE22								0.6	2.5	2.0

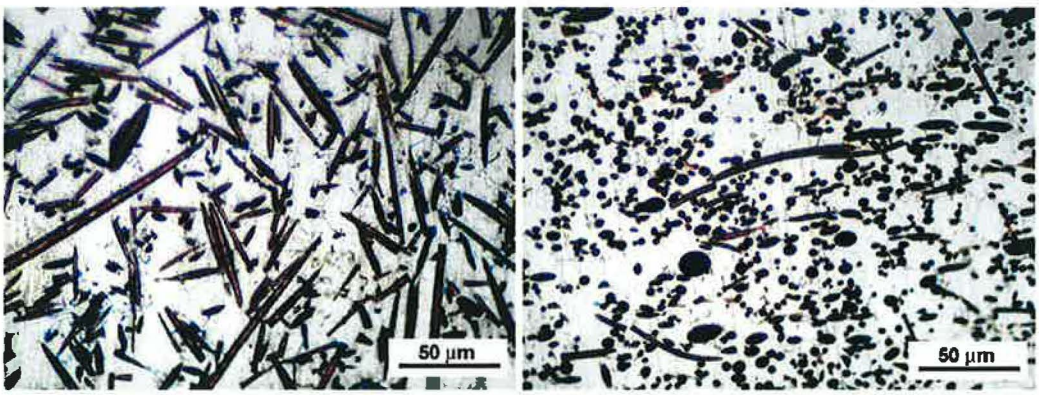

Figure 5.13: LM micrograph of as cast AS21 composite from the surface planes parallel (a) and perpendicular (b) to the sample axis.

5.5.1 Zirconium-free magnesium alloys and its composites

AS21 alloy and its composite

In order to extend the knowledge of deformation mechanisms which control mechanical and physical properties, the microstructure of pre-deformed AS21 alloy and its composite

were investigated by TEM. Additionally, the relation between the internal stresses and substructure was investigated. AS21 alloy and its composite in four states — as cast (state after the squeeze casting), after thermal treatment, and pre-deformed in compression and in tension — were subjected to the substructure investigation.

An Olympus C2000Z Light Microscope with a digital camera was used for the microstructure investigations. AS21 alloy and its composite specimens for metallographic examination were etched for 5–60 seconds in acetic-picral solution (10 ml acetic acid, 4.2 g picric acid, 10 ml H_2O, 70 ml 95% ethanol).

Thermal treatment of samples was conducted from room temperature to 380 °C at heating and cooling rates of 5 K/min in two thermal (heating and cooling) cycles. Deformation tests of the AS21 alloy and composite were carried out in an Instron testing machine (type 1186). Samples for the compression tests (50 mm length, 6 mm in diameter) and for the tension tests (74 mm length, 6 mm in diameter) were taken after thermal treatment and then pre-deformed at a constant crosshead speed giving the initial strain rate of 3×10^{-5} s^{-1}. The samples were deformed at room temperature parallel to their longitudinal axis. The plastic prestrain of samples was about 0.5 % in compression and 1 % in tension. Internal stresses of the AS21 alloy and composite were estimated by the SR tests.

AZ31 alloy deformed at various temperatures

The microstructure of the rolled AZ31 alloy in stress-relieved (H24) state deformed at various temperatures (room temperature, 100, 200, and 300 °C) were investigated. Strain rate jump tension tests of the AZ31 alloy were carried out on an Instron testing machine (type 1195) at cross-head speeds vp_1 = 0.2 mm/min and vp_2 = 2 mm/min giving an initial strain rate of 1.3×10^{-4} s^{-1}. Specimens of 25 mm gauge lenght, 5 mm with and with thickness of 1.6 mm were used for deformation. Specimens for the metallographic examination were etched for 20–30 seconds in the solution of 5 ml acetic acid, 6 g picric acid, 100 ml ethanol, and 10 ml H_2O.

AZ31 and AZ61 alloys prepared by rolling and ECAP

ECAP is a modern method of technology producing materials with ultra-fine grains. In the ECAP process, a workpiece is pushed through an angular die with two channels having identical cross-sections. The channels intersect at an angle, which is usually 90°. If the process is repeated several times, the shear strain is accumulated in the workpiece, which leads to structural refinement. The materials after ECAP processing have improved properties such as high yield strength, ductility, formability at high temperatures, and crystallographic texture changes.

Magnesium alloys AZ31 and AZ61 in four states[1] — after one rolling pass, after one rolling pass followed by ECAP, after three rolling passes, and after three rolling passes followed by ECAP — were investigated by LM and TEM. The samples were rolled at a temperature of 380 °C. The rolling rate was about 366 mm/s and the strain rate varied between 3.9 and 8.9 s^{-1}. The samples of a prism shape had the dimensions of 150×15×10 mm^3. Some samples after rolling were subjected to ECAP. The samples for ECAP had dimensions of 60×8×8 mm^3. The ECAP processing consisted of two stages: the samples were pressed for four passes at a temperature of 250 °C using route B_C (where the specimens are rotated by 90° in the same sense between the consecutive passes) followed by one pass at a temperature of 180 °C. Tensile specimens with 40 mm in gauge length, 5 mm width and with a thickness of 2 mm were machined.

AZ31 and AZ61 alloy specimens for metallographic examination were etched for 20–30 seconds in the solution of 5 ml acetic acid, 6 g picric acid, 100 ml ethanol, and 10 ml H_2O. Microhardness (HV) was measured on the polished surfaces along and perpendicular to the longest sample axis under a load of 100 g for 15 s.

5.5.2 Zirconium-containing magnesium alloys

QE22 and ZRE1 alloys

Superplasticity is the capability of a material to endure strains while applying low flow stresses without constriction and practically no strain-hardening. The elongation to failure

[1]The samples were kindly supplied by Doc. Ing. Miroslav Greger, CSc. from VŠB Technical University of Ostrava.

may exceed 300%, and in some cases even 1000%. A characteristic of the superplastic behaviour of materials is a strong strain rate dependence of flow stress. This dependence is described by the strain rate sensitivity parameter (m) that is part of the flow equation for structural superplasticity (*Hart*, 1967):

$$\sigma = k_1 \dot{\varepsilon}^m, \tag{5.8}$$

with material constant k_1. In order for a material to be superplastic, the strain rate sensitivity parameter must be higher than 0.3. Another condition for superplastic deformation is a fine microstructure with grain sizes of $d < 10$ μm. The value of the strain rate sensitivity parameter normally increases with decreasing grain sizes (*Padmanabhan and Davies*, 1988; *Kaibyshev*, 1992; *Mugrabi and Höppel*, 2001; *Rosochowski*, 2000; *Zhu and Langdon*, 2004). Fine grain structure may be obtained by various processes such as severe plastic deformation, phase transformation, recrystallisation, rapid solidification, or hot rolling (*Mugrabi and Höppel*, 2001; *Rosochowski*, 2000; *Zhu and Langdon*, 2004; *Zehetbauer*, 2003). Another method is thermo-mechanical treatment (hardening, overageing, and hot extrusion).

In Section 6.4, the microstructure of the superplastic QE22 and ZRE1 magnesium alloys prepared by a special thermo-mechanical procedure was investigated. The thermo-mechanical treatment was conducted in the following manner: oval specimens with dimensions of 72×80 mm cut from ingots of the ZRE1 and QE22 alloys were exposed for 10 hours to homogenizing annealing at 470 °C with the following cooling on air. After hardening, artificial ageing of the alloys was conducted for 10 hours at temperatures between 200 and 380 °C. After that, the overaged specimens were heated at 350 °C in a container of isothermal pressing device. The device consists of a press with a rated strain of 4000 kN and a tube furnace which heats instrumental rigging (container with a diameter of 75 mm, matrix and punch). Pressing was done with elongation coefficients (ratio of the area section of the container chamber to area of matrix orifice) of 20 and 26 through a two-step matrix.

5.5.3 Details of the specimen preparation for TEM

Two methods were used for the thin foil preparation for TEM: ion thinning and electropolishing. The methods and conditions used for the preparation of each experimental material are as follows. Foils from QE22 and AS21 alloys, and AS21 composite were prepared by the ion thinning method using ion-miller (LINDA) and PIPS (PIPS IV3) machines, respectively. The follows thinning conditions were used: small incidence angles of ion beam (to avoid artefacts in the substructure of the foils) and voltage of 4–5 kV between cathodes. Foils from AZ31, wrought AZ31, wrought AZ61, and ZRE1 alloys were thinned by the electropolishing method using the TENUPOL 3. The specimens were etched in the solution of 15.9 g of LiCl, 335 g of Mg perchlorate, 1500 ml of methanol, and 300 ml of butoxy-ethanol in the temperature range -55 to -40 °C. After electropolishing, the foils were washed in methanol. To prevent the formation of oxide surface layer, TEM foils of all experimental materials had to be stored in vacuum.

Investigations of substructure of the materials were carried out with JEOL 2000FX and Philips CM 200 Transmission Electron Microscopes operating at 200 kV and equipped with an energy dispersive X-ray analyzer (EDAX) which provides the analysis of individual phase composition.

Chapter 6

Results and discussion

6.1 Microstructure of thermally and mechanically loaded AS21 alloy and its composite

6.1.1 Microstructure and substructure evolution of AS21 alloy

The microstructure of the as cast samples is illustrated in Figure 6.1. Silicon is practically insoluble in magnesium and it is bounded in Mg_2Si particles. The Mg_2Si phase in two morphologies can be seen: a Chinese-script type (marked by a) and characteristic massive particles (marked by b). The majority of precipitates are of the Chinese-script type. The Mg_2Si particles are present at grain boundaries and within the grains as visible in Figure 6.2. The grain size varies in the range of 15–30 μm. No $Mg_{17}Al_{12}$ particles were observed by LM or TEM, which is in agreement with the substructure observation by *Janeček et al.* (2004) as well as with results of *Pekguleryuz and Kaya* (2003) or *Bronfin et al.* (2001) who found that the amount of $Mg_{17}Al_{12}$ phase in AS21 alloy is negligible.

Mg_2Si forms a very stable compound with a high hardness and a melting point of 1085 °C (*Raynor*, 1959; *Drápala et al.*, 2004). Due to a low CTE value of Mg_2Si (11.5 μm/m °C, 20 °C) compared to other matrix components (26.1 μm/m °C, 20 °C) for Mg; 24 μm/m °C, 20 °C for Al; 22.8 μm/m °C, 20 °C for Mn) (*http://www.matweb.com*), AS21 alloy can be considered as a two-phase composite. There is no chemical interaction between the matrix and Mg_2Si particles. Furthermore, Mg_2Si is known as a potential

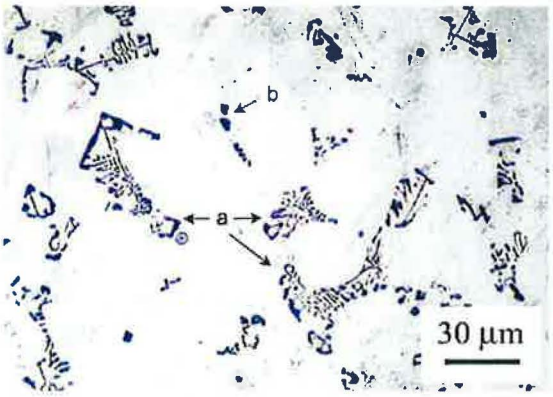

Figure 6.1: LM micrograph of the as cast AS21 alloy. Mg_2Si particles in Chinese script form (marked by a) and polygonal Mg_2Si particles (marked by b) are visible.

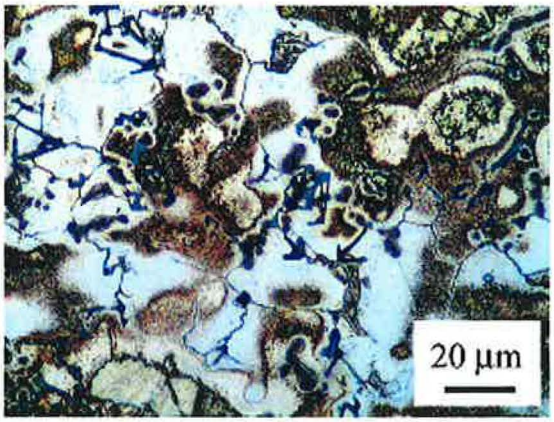

Figure 6.2: LM micrograph of the as cast AS21 alloy. Grain boundaries are visible.

reinforcement for producing MMCs (*Zhang et al.*, 2000).

The substructure of the AS21 alloy in the as cast state (Figure 6.3) is similar to the substructures in the states after thermal treatment and pre-deformation in compression and tension. Mg_2Si particles in oblate and elongated forms distributed throughout the volume of a sample are typical for all these states. Since Mg_2Si particles are thermally stable, their existence, configuration and location are not changed by heat treatment.

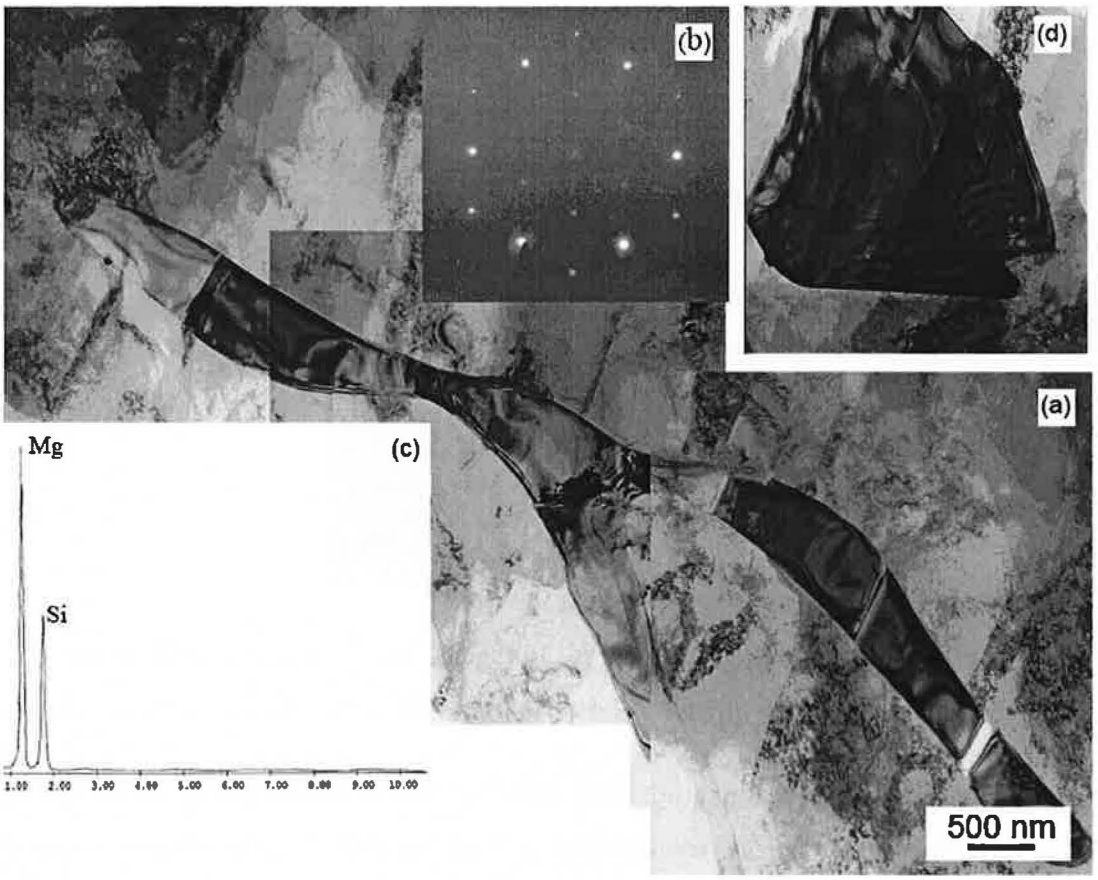

Figure 6.3: TEM micrograph (BF image) of the AS21 alloy in the as cast state. Mg_2Si particle (a), diffraction from the Mg_2Si particle (B = [111], g = ($\bar{2}$20)) (b), spectrum of the Mg_2Si particle (c), oblate Mg_2Si particle (B = [01$\bar{1}$]) (d).

Substructure of the AS21 alloy in the as cast state is characterized by a high number of long parallel twins with a relatively high dislocation density (Figure 6.4). The substructure of the samples after thermal treatment is similar to that of the as cast samples. Twins and Mg_2Si particles are observed throughout the volume of the samples (Figure 6.5).The

difference between the substructure of the samples after thermal treatment and as cast samples is the lower dislocation density in the former case. As temperature of AS21 alloy decreases from near the melting point of the matrix during processing, the large difference in CTE between Mg_2Si and matrix leads to the development of high thermal stresses. These high thermal stresses are partially relieved during cooling by the generation of dislocations. Additionally, *Hu et al.* (2007) found that the amount and the distribution of Mg_2Si phase can markedly influence the dislocation network in Mg-Si alloys and the dislocation density increases with increasing amount of Mg_2Si phase.

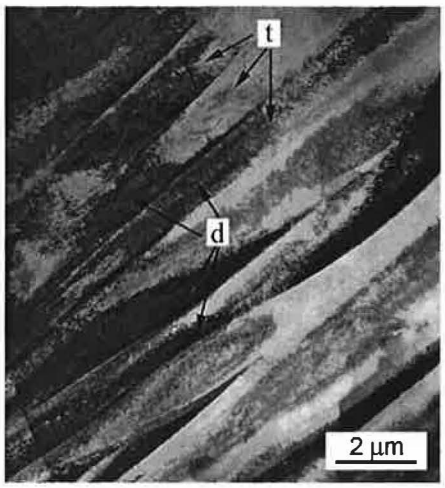

Figure 6.4: TEM micrograph (BF image) of the AS21 alloy in the as cast state. Parallel twins (marked by t) with a relatively high dislocation density (marked by d) are visible.

Our investigations using TEM show that pre-deformation both in compression and in tension increases the dislocation density. Dislocations between the parallel twins are characteristic for the substructures of the samples pre-deformed in compression and tension (Figure 6.6). High dislocation densities near the Mg_2Si particles in the specimens pre-deformed in compression and tension are observed (Figure 6.7). The dislocations in specimen pre-deformed in compression are shown in Figure 6.8. For the alloy pre-deformed in tension, some single AlMn particles are twinned (Figure 6.9).

The as cast and pre-deformed alloys posses a relatively high dislocation density around the Mg_2Si precipitates. Similarly, *Hu et al.* (2007) found a high dislocation density around the Mg_2Si precipitates in the Mg-2.3 wt.%Si alloy. An increased dislocation density in the as cast and pre-deformed samples relates to the thermal stresses and thermal strains

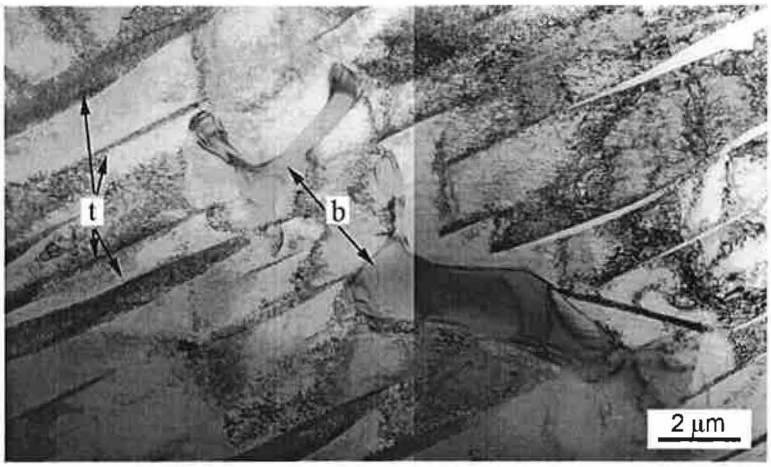

Figure 6.5: TEM micrograph (BF image) of the AS21 alloy after thermal treatment. Parallel twins (marked by t) and Mg_2Si particles (marked by b) are visible throughout the volume of the sample.

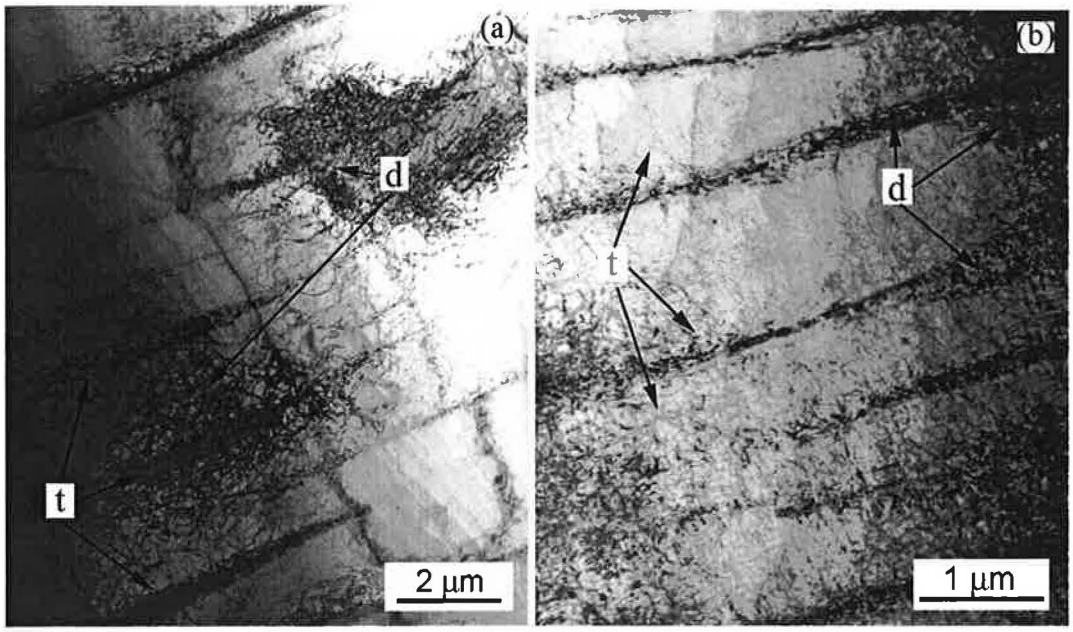

Figure 6.6: TEM micrograph (BF image, B = $[1\bar{2}13]$, g = $(\bar{1}010)$) of AS21 alloy showing parallel twins (marked by t) and dislocations (marked by d): (a) sample pre-deformed in compression; (b) sample pre-deformed in tension.

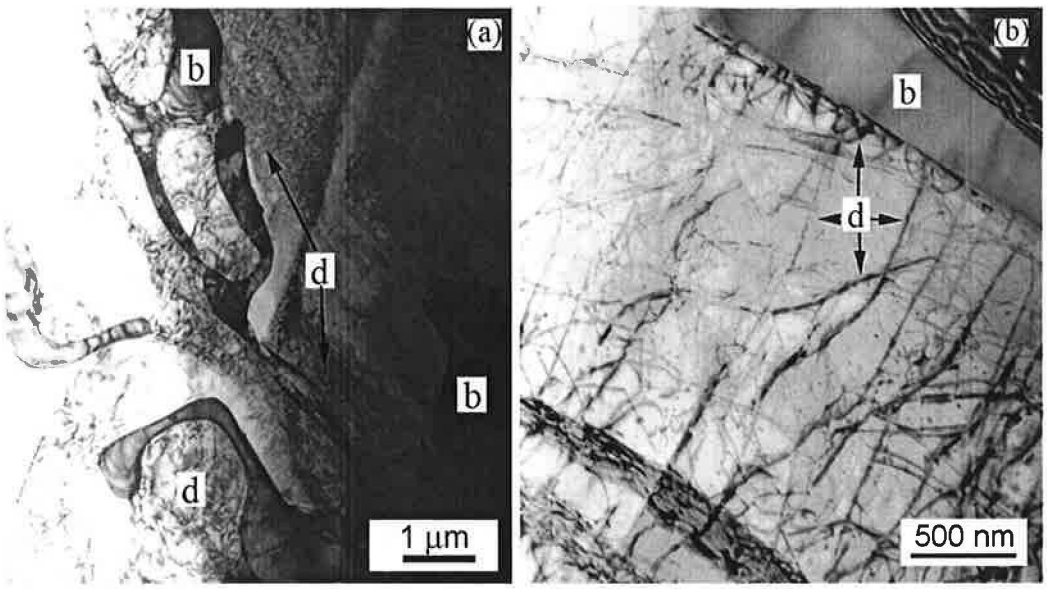

Figure 6.7: TEM micrograph (BF image) of AS21 alloy showing dislocations (marked by d) near the Mg_2Si particles (marked by b): (a) sample pre-deformed in compression; (b) sample pre-deformed in tension.

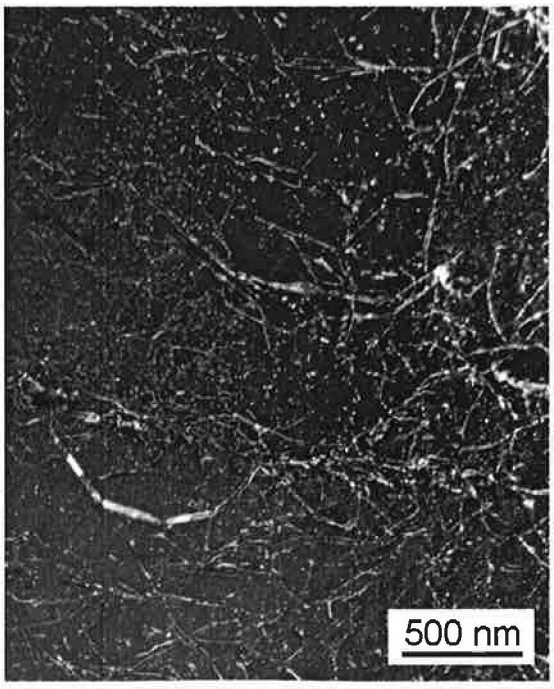

Figure 6.8: TEM micrograph (DF image) of the dislocations in the AS21 alloy pre-deformed in compression.

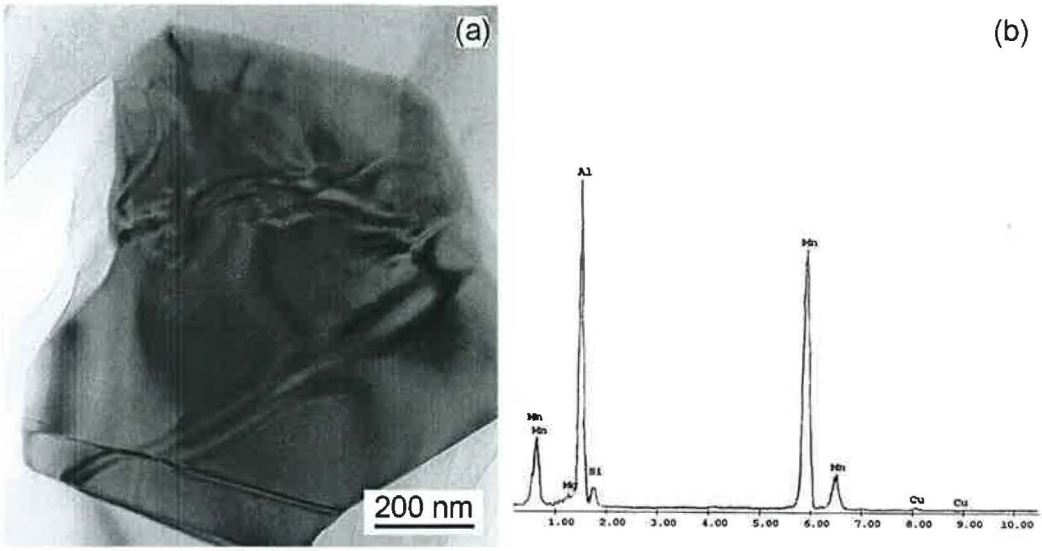

Figure 6.9: TEM micrograph (BF image) of the AS21 alloy pre-deformed in tension: (a) AlMn particle with a twin; (b) spectrum from the AlMn particle.

established during the manufacturing cooling or pre-deformation.

Substructures of the AS21 alloy in the as cast, after thermal treatment, pre-deformation in compression and tension states was investigated. Substructure of as cast and thermally treated samples differ namely in the dislocation density; due to thermal treatment the density is lower. The substructure of the AS21 alloy in the as cast state is characterized by a high number of long parallel twins with a relatively high dislocation density. The substructure of samples after thermal treatment is similar to that of the as cast samples. Predeformation both in compression and in tension increases the dislocation density. High dislocation densities near the Mg_2Si particles in the specimens pre-deformed in compression and tension are observed.

6.1.2 Microstructure and substructure evolution of AS21 composite

The microstructure of the as cast AS21 composite is presented in Figure 6.10. It consists of Saffil fibres (marked by a) and Mg_2Si phase in two morphologies (similar to the AS21 alloy): Chinese-script type (marked by b) and characteristic massive particles (marked by c). The size of grains seen in Figure 6.10 is in ranges from 15 to 30 μm. The AS21 composite exhibits no chemical interaction between the matrix and the reinforcement

during preparation. No porosity was found in the AS21 composite.

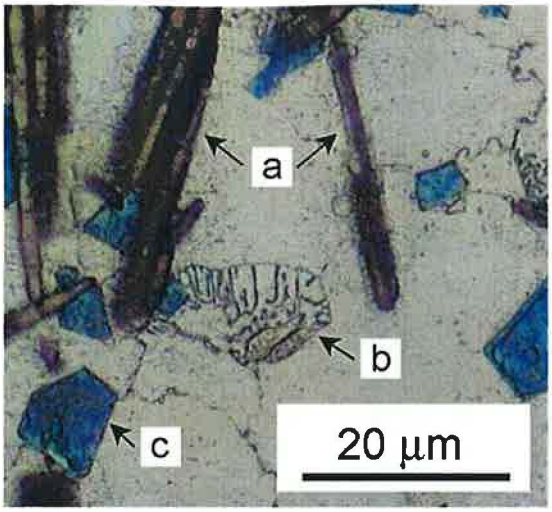

Figure 6.10: LM micrograph of the as cast AS21 composite microstructure. Saffil fibres (marked by a), Mg_2Si particles in Chinese script form (marked by b), and polygonal Mg_2Si particles (marked by c) are visible.

Substructure investigations may enable to draw more general conclusions concerning internal thermal stresses developed in composites and mechanisms occuring during the pre-deformation. Substructures of the AS21 composite in the as cast state, state after thermal treatment, and states after pre-deformation in compression and tension were observed.

Substructure of the AS21 composite in the as cast state is characterized by a high number of long parallel twins with a relatively high dislocation density (Figure 6.11). Dislocations nearby Mg_2Si particles are seen in Figure 6.12. Broken Saffil fibres were also found in the as cast sample (Figure 6.13).

After thermal treatment of the composite, linear dislocations are present inside (Figure 6.14) and near Mg_2Si particles (Figure 6.15), and both inside and near twins (Figure 6.16). The dislocation density of the composite after thermal treatment is lower than in the as cast specimen.

Substructure of pre-deformed specimens is represented by a high dislocation density and twins. Figure 6.17 shows a high density of dislocations between the parallel twins. Overview of the specimen pre-deformed in tension with a high dislocation density near

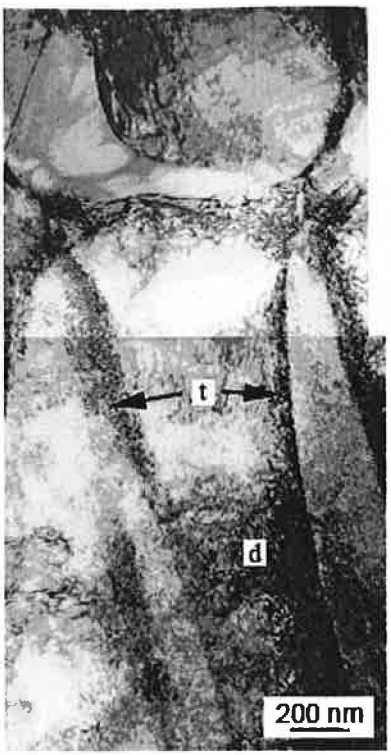

Figure 6.11: TEM micrograph (BF image) of the AS21 composite in the as cast state. Long parallel twins (marked by t) with a relatively high dislocation density (marked by d) are visible.

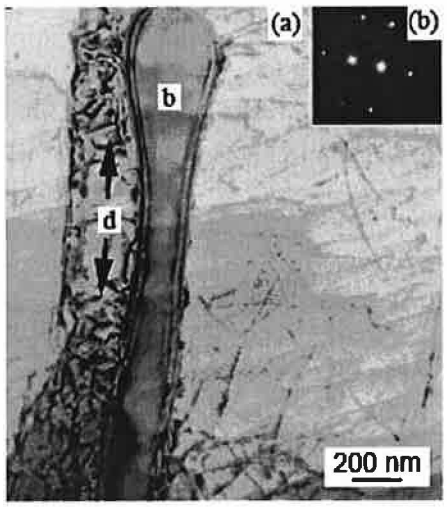

Figure 6.12: TEM micrograph (BF image) of the AS21 composite in the as cast state. Dislocations (marked by d) nearby Mg_2Si particles (marked by b) are visible.

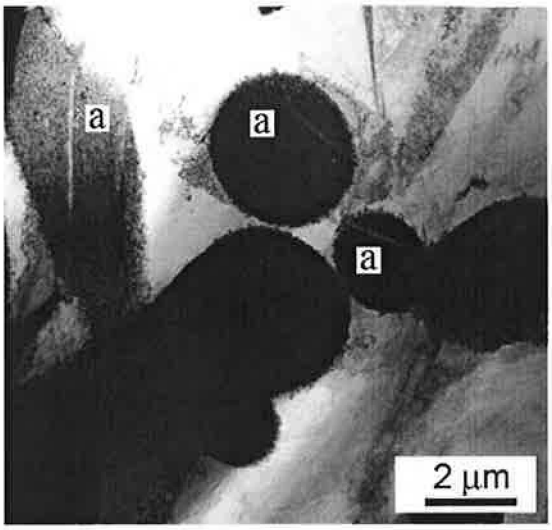

Figure 6.13: TEM micrograph (BF image) of the AS21 composite in the as cast state. Broken Saffil fibres (marked by a) are visible.

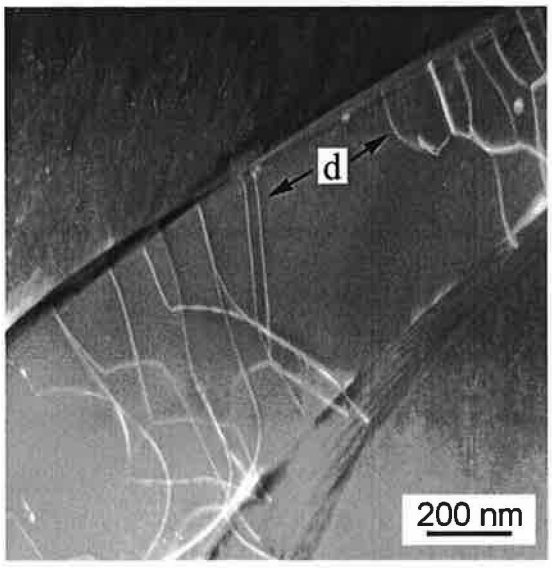

Figure 6.14: TEM micrograph (DF image) of the AS21 composite after thermal treatment. Dislocations (marked by d) are visible inside Mg_2Si particle.

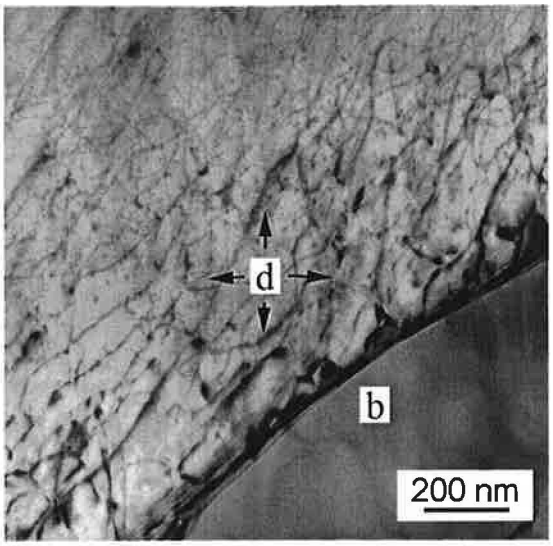

Figure 6.15: TEM micrograph (BF image) of the AS21 composite after thermal treatment. Dislocations (marked by d) located near Mg_2Si particles (marked by b) are visible.

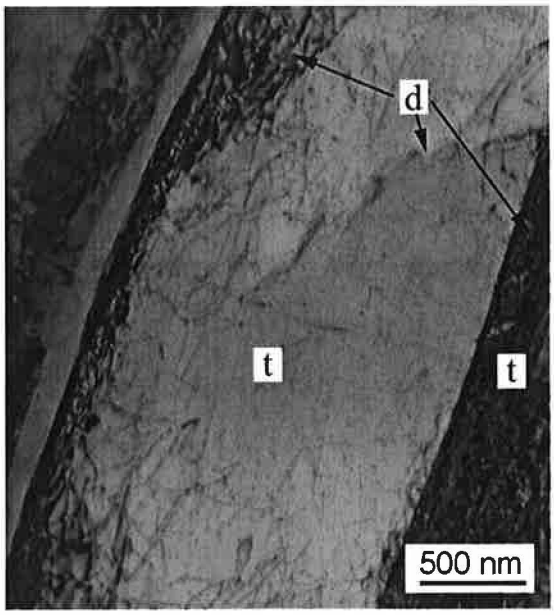

Figure 6.16: TEM micrograph (BF image) of the AS21 composite after thermal treatment. Dislocations (marked by d) inside twins (marked by t) are visible.

the Mg_2Si particle and Saffil fibre is presented in Figure 6.18. Typical pile-up dislocations stored in the vicinity of the Mg_2Si precipitates are shown in Figure 6.19. Twinning starts in the area without Saffil fibres.

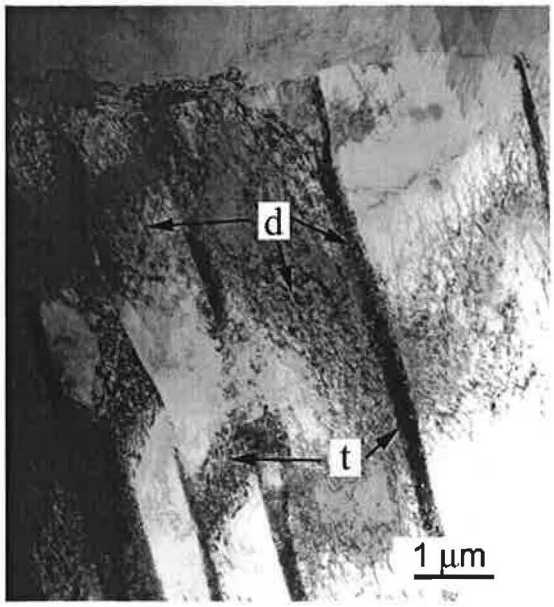

Figure 6.17: TEM micrograph (BF image) of the AS21 composite pre-deformed in compression. Parallel twins (marked by t) and high dislocation density (marked by d) between the twins are visible.

Finally, it is possible to summarize that TEM revealed a higher dislocation density in the vicinity of Saffil fibres and Mg_2Si particles than in the matrix. The deformation mechanisms of magnesium alloys pre-deformed at a constant strain rate in tension are different from those of Mg alloys pre-deformed in compression (*Mann et al.*, 2004; *Meza-García et al.*, 2007). While the tensile deformation is mainly controlled by dislocation glide (see Figure 6.19), the compression deformation is realized at the yield stress also by twinning. TEM analysis shows a high density of twins in the AS21-25 vol.% Saffil after deformation in the compression test (Figure 6.17). In this connection it is interesting to note that reversible movement of twin boundaries may cause a pseudoelastic behaviour, as observed by *Cáceres et al.* (2003).

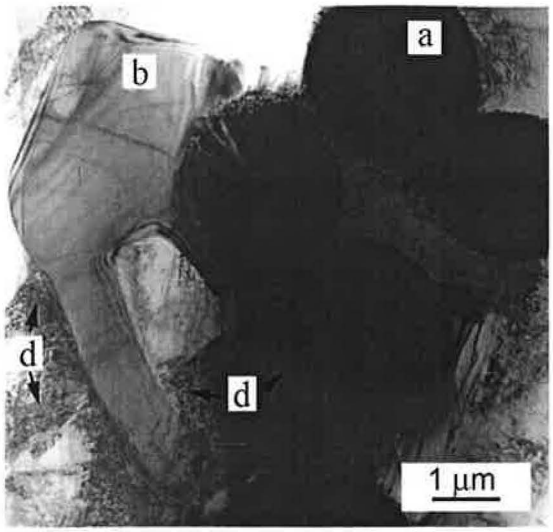

Figure 6.18: TEM micrograph (BF image) of the AS21 composite pre-deformed in tension. High dislocation density (marked by d) near the Mg_2Si particle (marked by b) and Saffil fibre (marked by a) are visible.

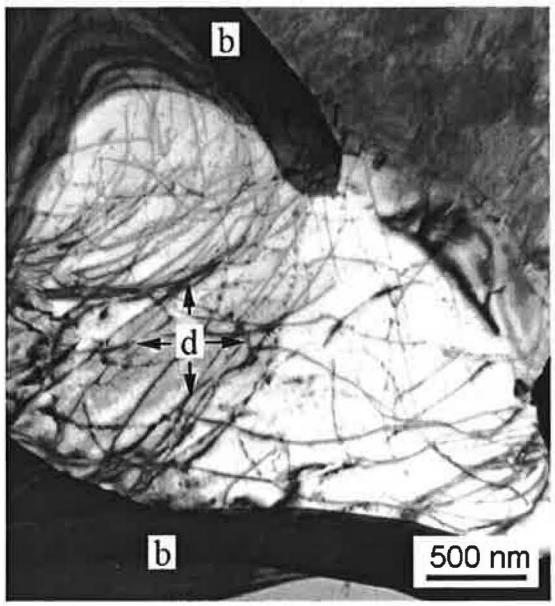

Figure 6.19: TEM micrograph (BF image) of the AS21 composite pre-deformed in tension. Dislocations (marked by d) near Mg_2Si particle (marked by b) are visible.

6.1.3 Stress relaxation in AS21 alloy and composite at elevated temperatures

Internal stress in AS21 alloy and its composite

The true stress-true strain curves of AS21 alloy obtained at 100, 250, and 300 °C are presented in Figures 6.20a, b, and c, respectively. In these figures, the internal stress is also plotted against strain. The internal stresses were estimated using the equation (5.6). It is obvious from the figures that the internal stress σ_i forms a substantial contribution to the applied stress σ_{ap} at all temperatures. The internal stress first increases with increasing strain (up to 12% at 100 °C, 4% at 250 °C, and 2% at 300 °C) and then decreases. The decreasing of the internal stress with strain indicates softening. This is connected with dynamic recovery. The internal stress also decreases with increasing test temperature. In Figures 6.20a,b, and c, the effective stress is also plotted as a function of strain.

Figure 6.21 shows the dependence of the internal stress on the applied stress in AS21 alloy at different temperatures. The values of the internal stress are close to the applied stress in the whole measured range at room temperature. However, the internal stress deviates from the applied stress with increasing test temperature. At 300 °C, the internal stress is almost independent of the applied stress. A rapid decrease in the ratio of the internal stress to the applied stress with temperature (Figure 6.22) indicates that the activity of dynamic recovery process increases with increasing test temperature.

The true stress-true strain curves of AS21 composite obtained at 100, 200, and 300 °C are presented in Figures 6.23a, b, and c, respectively. For all temperatures, the internal stress increases with strain at the very beginning of deformation, and then it is nearly constant or it decreases with strain. The stress component due to load transfer σ_{LT} is calculated using the equation (3.2). The internal stress σ_i is a substantial contribution to the matrix stress σ_m for the AS21 composite. The figures also show that the internal stress decreases with increasing temperature. The internal stress depends on the dislocation density (deformation gradient) in materials and decreases with strain at higher temperatures as a result of recovery processes (dislocation annihilation) (*Trojanová et al.*, 2006).

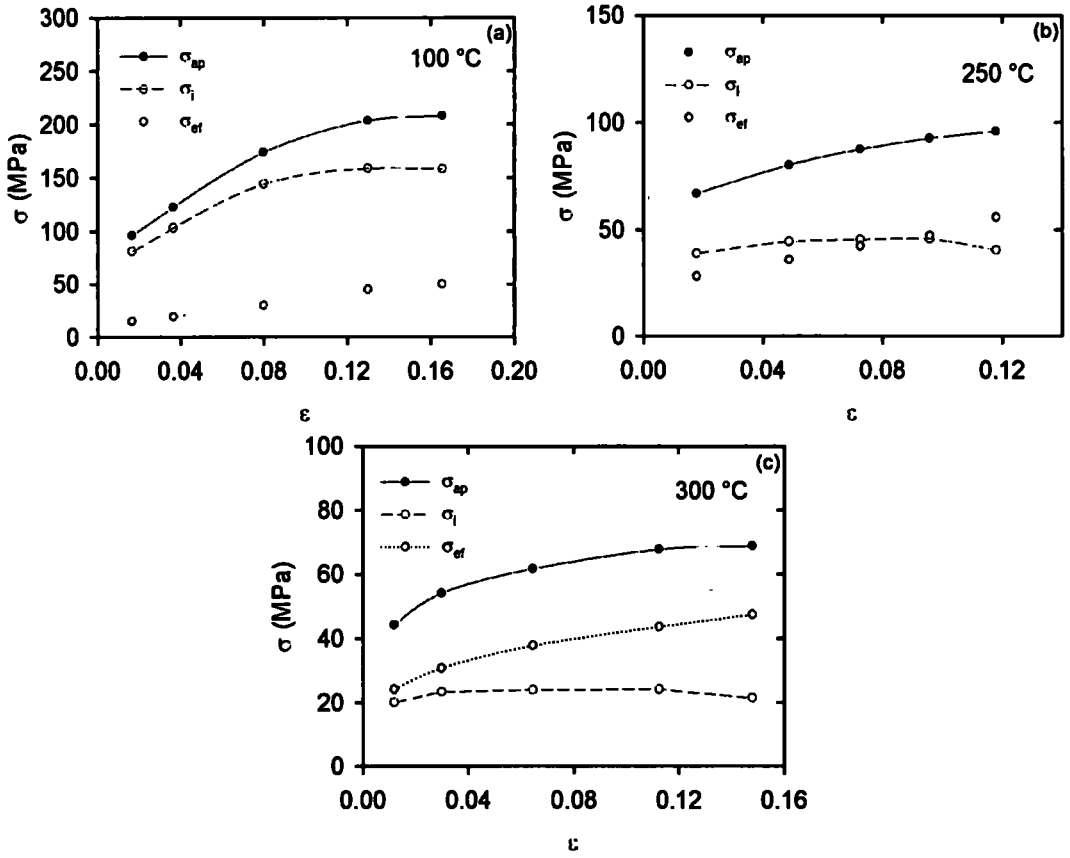

Figure 6.20: A part of the true stress-true strain curve at 100 (a), 250 (b), and 300 °C (c) obtained for AS21 alloy. The full points on the upper curve indicate the stresses at which the SR tests were performed.

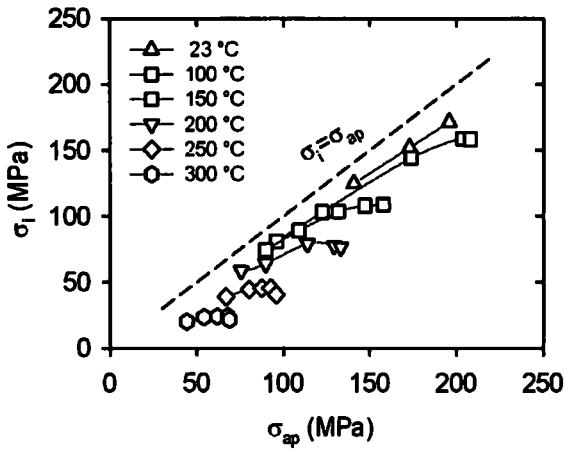

Figure 6.21: Dependence of the internal stress on the applied stress in AS21 alloy.

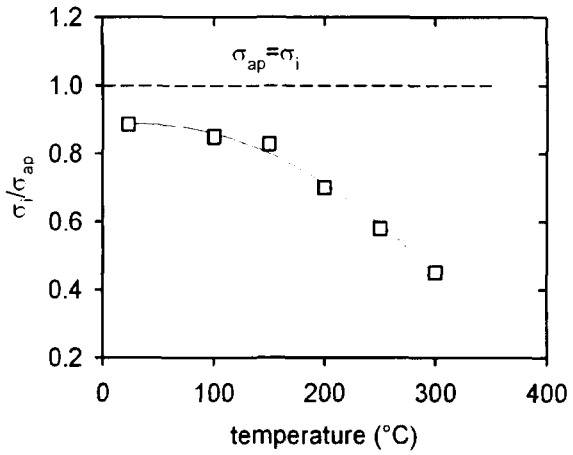

Figure 6.22: Temperature dependence of the ratio of the internal stress to the applied stress in AS21 alloy.

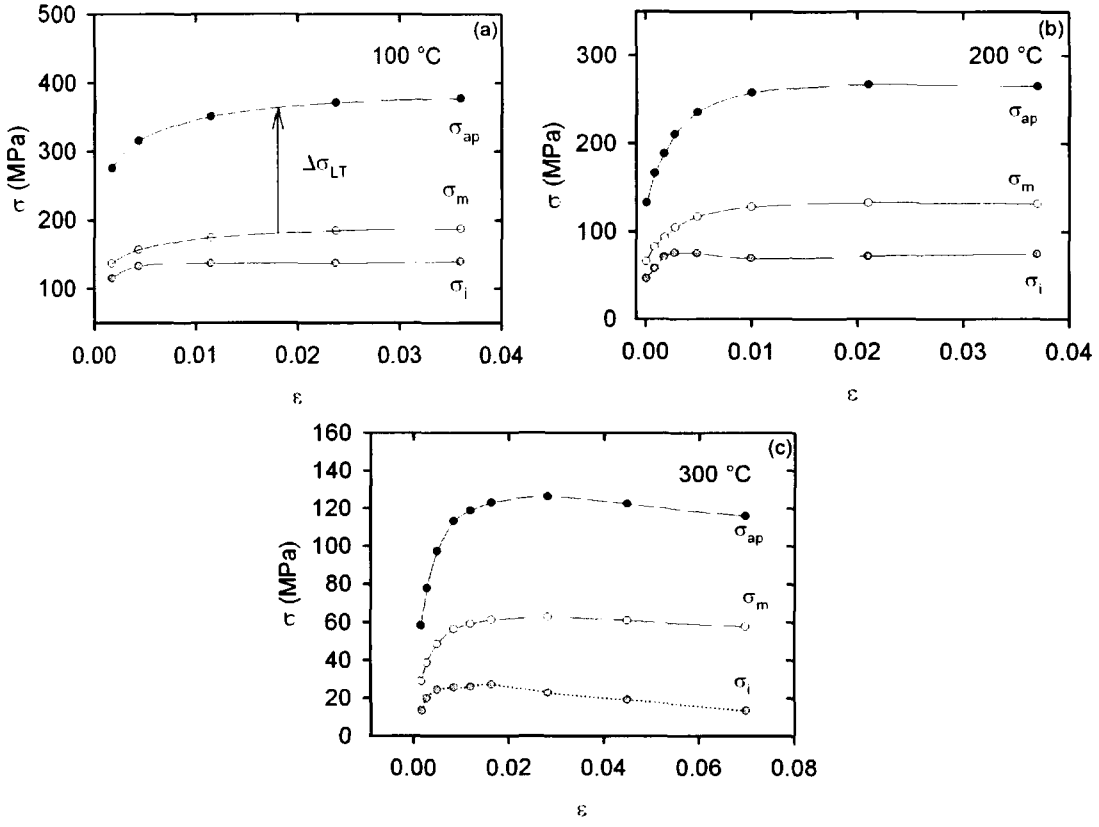

Figure 6.23: A part of the true stress-true strain curve at 100 (a), 200 (b), and 300 °C (c) obtained for AS21 composite. The points on the curve indicate the stresses at which the SR tests were performed.

Thermally activated deformation of AS21 alloy and its composite

The values of the activation volume V of AS21 alloy as a function of the effective stress at different temperatures are shown in Figure 6.24a. The values of the activation volume V of AS21 composite (Figure 6.24b) were estimated from equations (5.4) and (5.5) using the stress decrease in the matrix ($\sigma_m = \sigma_{ap} - \sigma_{LT}$). The values of the activation volume are in b^3 units.

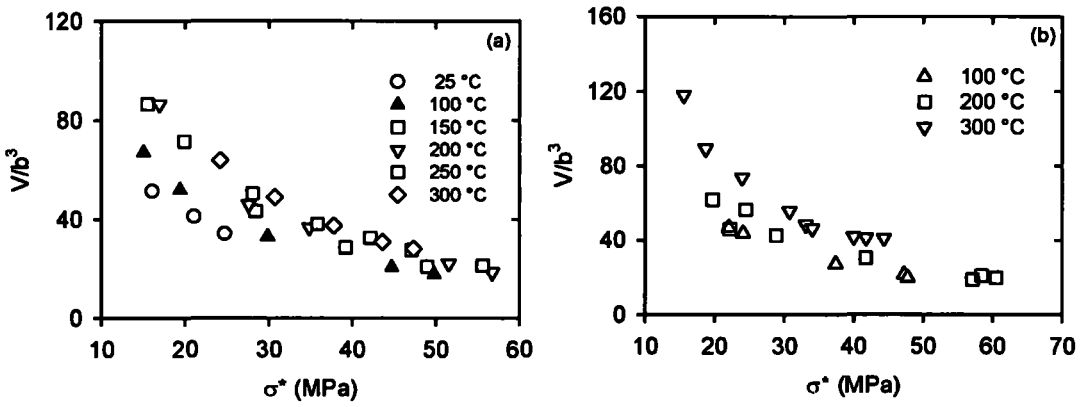

Figure 6.24: The plot of the activation volume in b^3 against the effective stress for AS21 alloy (a) and composite (b) at different temperatures.

For comparison, Figure 6.25 shows the values of the activation volume estimated for AS21 composite at temperatures of 100 and 300 °C together with the values of the AS21 alloy at the same temperatures. Because the values of the activation volume for the alloy and composite are very similar, we can conclude that the thermally activated processes are the same.

Kocks et al. (1975) suggested an empirical equation between the Gibbs enthalpy ΔG and the effective stress σ^* in the following form:

$$\Delta G = \Delta G_0 \left[1 - \left(\frac{\sigma^*}{\sigma_0^*}\right)^p\right]^q, \tag{6.1}$$

where ΔG_0 is the Gibbs enthalpy for the zero effective stress and σ_0^* is the effective stress at 0 K. The effective stress as a function of temperature and strain rate may be described as:

$$\sigma^* = \sigma_0^* \left[1 - \left(\frac{kT}{\Delta G_0} ln \frac{\dot{\varepsilon}_0}{\dot{\varepsilon}}\right)^{1/q}\right]^{1/p}, \tag{6.2}$$

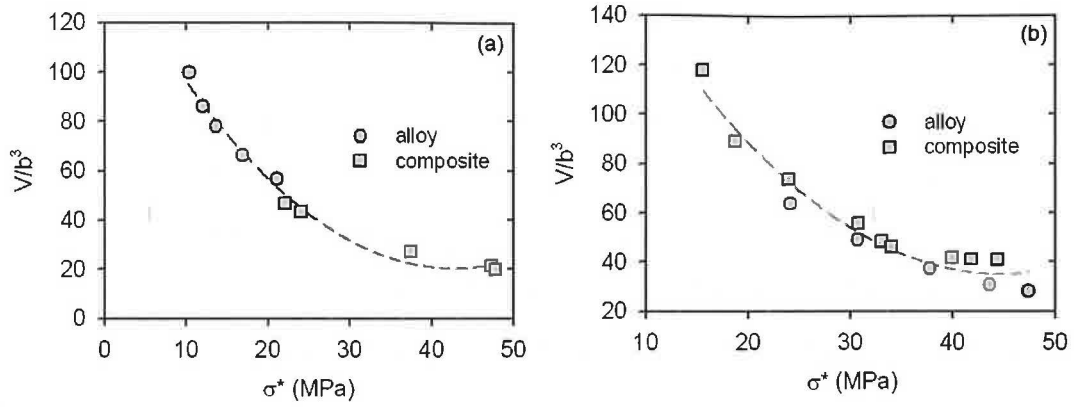

Figure 6.25: The plot of the activation volume in b^3 against the effective stress for AS21 alloy and composite at 100 (a) and 300 °C (b).

where p and q are phenomenological parameters reflecting the shape of a resistance obstacle profile (force-distance profile of the obstacles). The possible ranges of values p and q are limited by the conditions $0 < p \leq 1$ and $1 \leq g \leq 2$ (*Kocks et al.*, 1975; *Trojanová et al.*, 2007b). For the calculations, the values $p = 1/2$ and $q = 1/3$ were taken according to *Ono* (1968), who suggests that these values describe a barrier shape profile that fits many predicted barrier shapes. Thermodynamics generally defines the activation volume as:

$$V = -\left(\frac{d\Delta G}{d\sigma^*}\right)_T . \tag{6.3}$$

One may estimate V experimentally as:

$$V = kT\left(\frac{d\ln\dot{\varepsilon}}{d\sigma^*}\right)_T = kT\left(\frac{d\ln(-\dot{\sigma})}{d\sigma^*}\right)_T . \tag{6.4}$$

The equation (6.4) may be rewritten as:

$$V = \frac{\Delta G_0 pq}{\sigma_0^*}\left[1-\left(\frac{\sigma^*}{\sigma_0^*}\right)^p\right]^{q-1}\left(\frac{\sigma^*}{\sigma_0^*}\right)^{p-1} . \tag{6.5}$$

As it is obvious from Figure 6.25, the values of the activation volume follow the curve curve given by equation (6.5).

The internal stress increases due to dislocation storage in the matrix, $\sigma_i^D \propto \Delta\rho^{1/2}$, because the total dislocation density $\Delta\rho$ increases due to two reasons: (a) the generation of thermal dislocations and (b) the presence of geometrically necessary dislocations. Typically, CTE of the matrix is higher than CTE of the ceramic reinforcement. When the metal

matrix composite is cooled from a higher temperature to room temperature, misfit strains occur at the matrix-reinforce interface because of different thermal contractions between matrix and reinforcement. These strains induce thermal stresses that may be higher than the yield stress of the matrix. It means that the thermal stresses may generate new dislocations at the interfaces. Therefore, after cooling a composite, the dislocation density in the matrix increases. The density of newly formed dislocations (thermal dislocation density) near reinforcements (fibres, particles) can be calculated according to *Arsenault and Shi* (1986) as:

$$\rho_T = \frac{B f \Delta\alpha \, \Delta T}{b(1-f)} \frac{1}{d_t}, \tag{6.6}$$

where f is the volume fraction of the reinforcement, d_t is its minimum size, b is the magnitude of the Burgers vector of dislocations, B is a geometrical constant, $\Delta\alpha$ is the difference in the coefficients of thermal expansion, and ΔT is the temperature change. For our calculations we used the following values of the parameters: $B = 10$, $d_t = 3$ mm, $f = 0.25$, $b = 3.21 \times 10^{-10}$ m (*Mabuchi, M. and K. Higashi*, 1996). The calculated thermal dislocation density is $3.47 \times 10^{13}\,\mathrm{m}^{-2}$.

The incompatibility between the matrix and the fibres causes generation of geometrically necessary dislocations during deformation, resulting in an increase of strain hardening rate. The density of these dislocations can be approximated by the following formula (*Luster et al.*, 1993):

$$\rho_G = \frac{f\, 8\, \varepsilon_p}{b\, d_t}, \tag{6.7}$$

where ε_p is the plastic strain. The factor 8 is an approximate value (*Ashby*, 1970): it depends on the geometrical configuration. It is obvious that the density ρ_G increases with increasing plastic deformation. The calculated value of geometrically necessary dislocations during deformation is $2.01 \times 10^{13}\,\mathrm{m}^{-2}$ (at $\varepsilon = 0.01$).

Due to the thermal dislocations and geometrically necessary dislocations, the internal stress level in composites is higher than in monolitic alloys. The difference between the internal stresses of AS21 composite and the alloy obtained from the experiment is 85.5 MPa, and it agrees well with the corresponding theoretical value $\Delta\sigma = \gamma \psi G b \Delta\rho^{1/2} = 84.4$ MPa.

To conclude, the load transfer from the matrix to the reinforcing phase (fibres) is

an important contribution to the deformation mechanisms. The internal stress estimated from the SR tests decreases with increasing deformation temperature. The values of the activation volumes are in the order of $10 - 10^2\ b^3$. The estimated values of the activation volume indicate that the main thermally activated process is very probably the glide of dislocations.

6.2 Internal structure evolution of the AZ31 alloy deformed at various temperatures

6.2.1 Microstructure of the AZ31 alloy deformed at various temperatures

Microstructure of the AZ31 alloy deformed at room temperature, 100, 200, and 300 °C are shown in Figures 6.26, 6.27, 6.28, and 6.29, respectively. Samples deformed at room temperature have heterogeneous microstructure with fine ($\sim$ 500 nm–3 μm) and coarse ($\sim$ 5–15 μm) grains arranged in zones (Figure 6.26). Many twins are present inside grains. As it is well known, twinning is one of the deformation mechanisms in magnesium alloys at room temperature (*Bohlen et al.*, 2004; *Mordike and Lukáč*, 2006; *Dobroň et al.*, 2007; *Meza-García et al.*, 2007). Similar microstructure is observed in the specimen deformed at 100 °C (Figure 6.27). Figure 6.28 shows microstructure of the AZ31 specimens deformed at 200 °C. It can be seen that the microstructure is homogeneous with recrystallized grains. A significant grain refinement is achieved. The grain size range (3–6 μm) differs from that of the two previous specimens. Twins are not observed inside grains. The microstructure examination of the AZ31 alloy deformed at 300 °C reveals homogeneities (Figure 6.29) as similar in the AZ31 alloy deformed at 200 °C . Grain sizes increase with deformation temperature and vary in the range of 6–20 μm. Similar to the specimen deformed at 200 °C, grains are recrystallized and twins are not present inside grains.

We could summarize that homogeneity of the microstructure is achieved in specimens deformed at 200 and 300 °C. Recrystallized grains and the absence of twins are character-

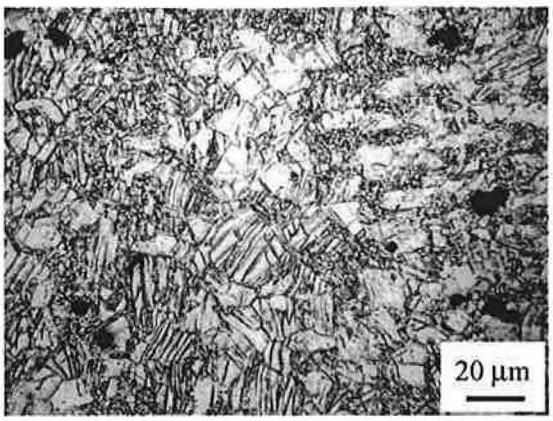

Figure 6.26: LM micrograph of the AZ31 alloy deformed at RT.

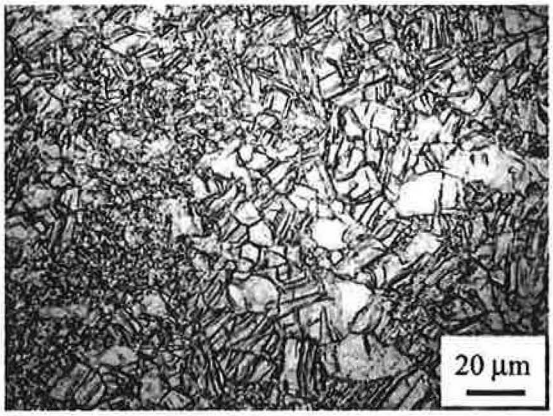

Figure 6.27: LM micrograph of the AZ31 alloy deformed at 100 °C.

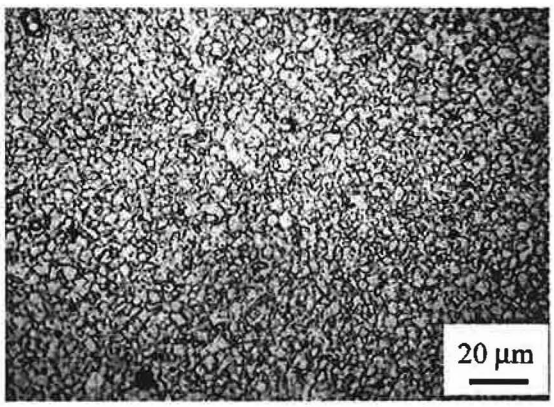

Figure 6.28: LM micrograph of the AZ31 alloy deformed at 200 °C.

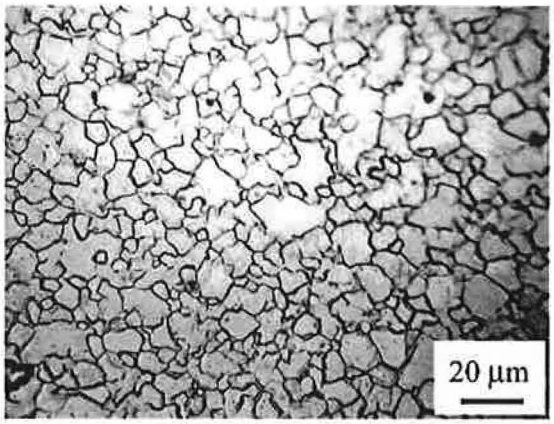

Figure 6.29: LM micrograph of the AZ31 alloy deformed at 300 °C.

istic for the specimens deformed at higher temperature in contrast to specimens deformed at room temperature and 100 °C.

6.2.2 Substructure of the AZ31 alloy deformed at various temperatures

The following figures show characteristic dislocation arrangements observed in the AZ31 alloy deformed in tension at room temperature (Figure 6.30), 100 °C (Figure 6.31), 200 °C (Figure 6.32), and 300 °C (Figure 6.33). A highly deformed substructure (Figures 6.30a,b) was observed in the specimens deformed at room temperature. Many twins (crossed and parallel) are present inside grains (Figure 6.30c). Some grains without dislocations are also observed (Figure 6.30d). Figures 6.31a and b present twins and grains without dislocations in the specimens deformed at 100 °C. The dislocation structure of the specimen deformed at 100 °C is similar to the microstructure of the specimen deformed at room temperature. Recrystallized grain boundaries are seen in the AZ31 alloy deformed at 200 °C (Figure 6.32a). Grains without dislocations were also observed (Figure 6.32b) as in the previous two specimens. ZnAl particles lie in grain boundaries. Dislocation structure of the AZ31 alloy deformed at 300 °C is shown in Figures 6.33a, b, and c. Coarse grains with low density of dislocations are frequently observed (Figures 6.33a,b). Some of the dislocations present zigzag contrast, which means that they are tilted with respect to the incident electron beam. Figures 6.33a,c show dislocations pinned on fine Mn particles.

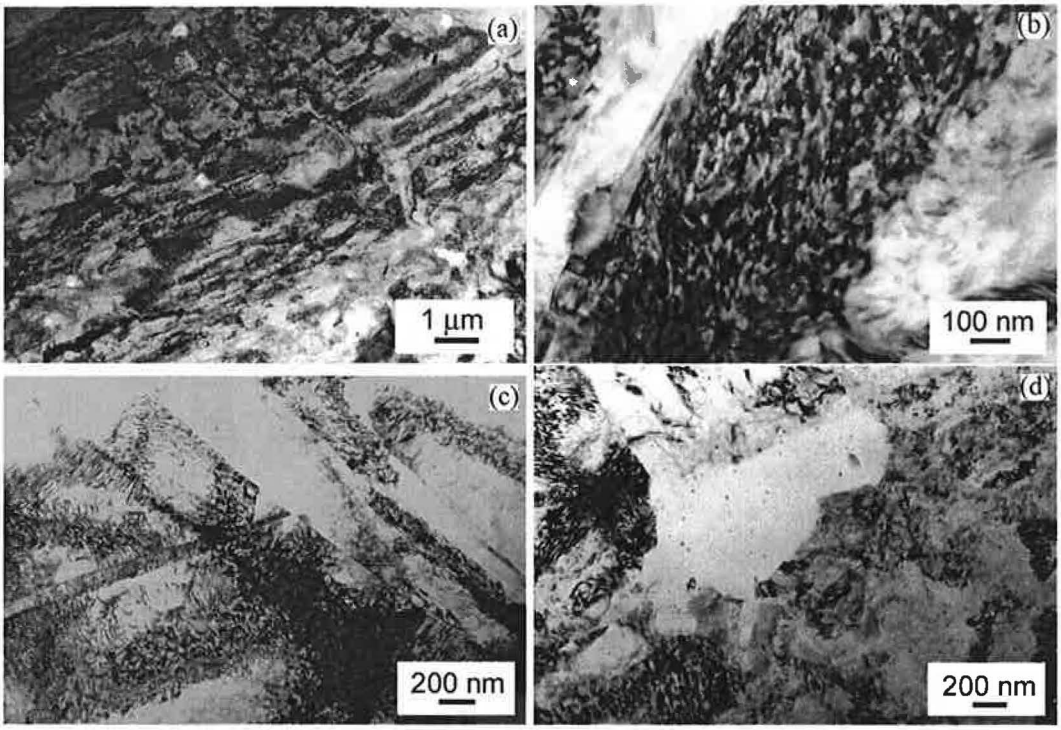

Figure 6.30: TEM micrograph of the AZ31 alloy deformed at room temperature.

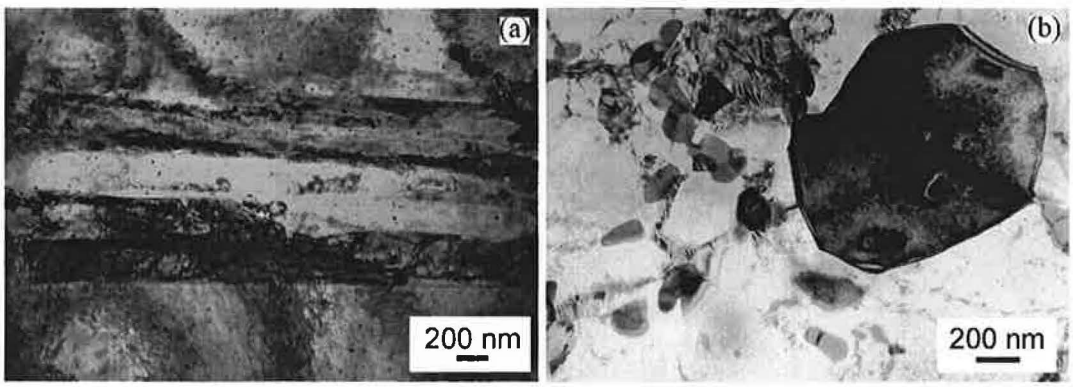

Figure 6.31: TEM micrograph of the AZ31 alloy deformed at 100 °C.

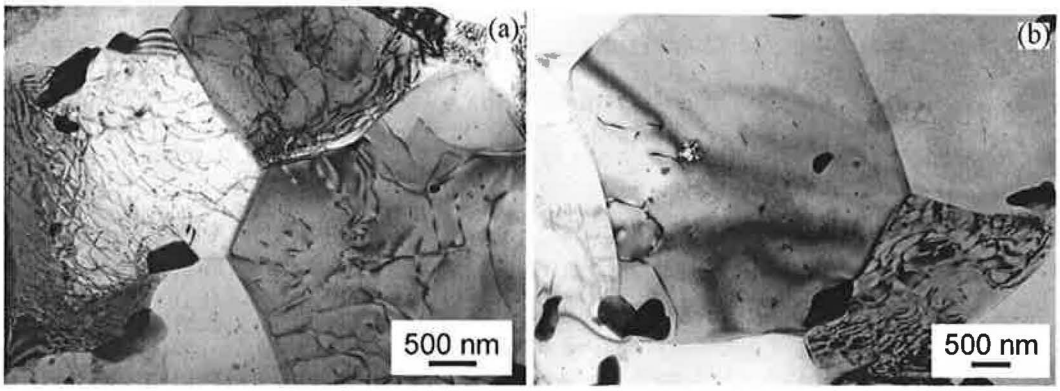

Figure 6.32: TEM micrograph of the AZ31 alloy deformed at 200 °C.

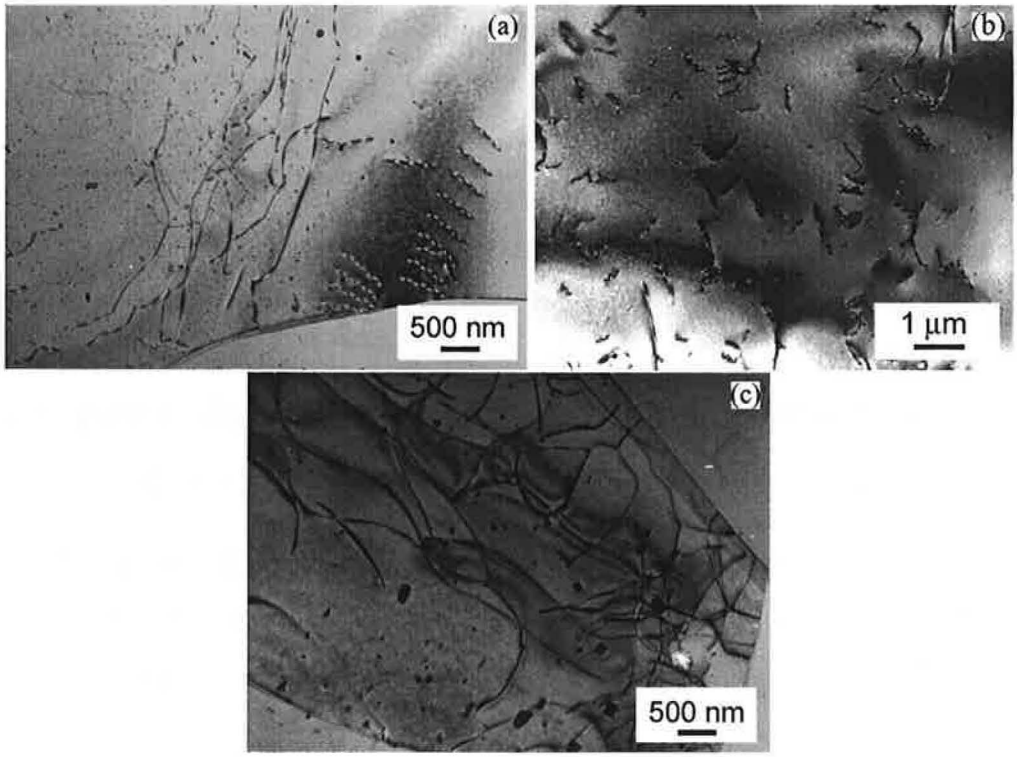

Figure 6.33: TEM micrograph of the AZ31 alloy deformed at 300 °C.

The specimens deformed at room temperature and 100 °C have similar heterogeneous substructures with high dislocation densities, marble-like structures of dislocations, i.e high dislocation density, intense twinning, twins with high dislocation densities, and some grains without dislocations. However, the amount of grains without dislocations for the specimen deformed at 100 °C is higher than in the specimen deformed at room temperature.

The substructures of the specimens deformed at 200 and 300 °C are homogeneous with recrystallized grains, without twins, and with some grains without dislocations. Grains in specimens deformed at 300 °C are coarser than grains in specimens deformed at 200 °C. The highest dislocation density was observed in the specimens deformed at room temperature and 100 °C while the density of dislocations is significantly lower in the specimens deformed at 200 °C and reaches its minimum value for the specimens deformed at 300 °C.

To conclude, the specimens deformed at room temperature and 100 °C have high dislocation densities, whereas the dislocation density of the specimens deformed at 200 °C and 300 °C is low. Recrystallized grains are characteristic for the AZ31 alloy deformed at 200 °C and 300 °C. The observed dislocation behaviour, including recrystallization, agrees with experimental study of the deformation behaviour of AZ31 alloy (*Balík et al.*, 2007). The flow stress decrease with increasing defomation temperature indicates a decrease of the dislocation density as observed in this work.

6.2.3 Stress relaxation in the AZ31 alloy deformed at various temperatures

Figure 6.34 demonstrates example of the stress-strain curve obtained at 100 °C for AZ31 alloy. The activation volume values were estimated from experiments in which the strain rate $\dot{\varepsilon}_1$ is suddenly changed to $\dot{\varepsilon}_2$ and the resulting change in the flow stress $\Delta\sigma$ is measured.

$$V = kT\frac{\ln(\dot{\varepsilon}_1/\dot{\varepsilon}_2)}{\Delta\sigma}. \tag{6.8}$$

The strain dependences of the activation volume V in b^3 for AZ31 alloy at different

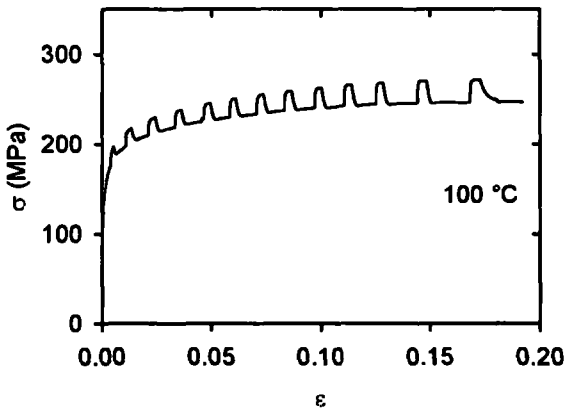

Figure 6.34: Stress-strain curve obtained at 100 °C for AZ31 alloy.

temperatures are shown in Figure 6.35. The activation volume increases with temperature, which indicates the operation of recovery processes, the decrease of the dislocation density, and possible dynamic recrystallization. This agrees with TEM observations shown in Section 6.2.2, where the amount of recrystallized grains and grains with low dislocation density increases with increasing deformation temperature.

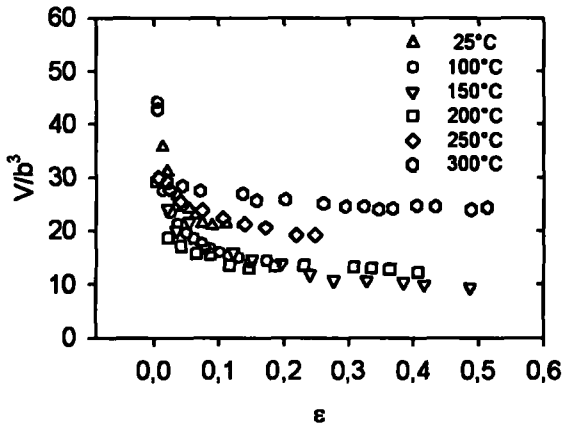

Figure 6.35: Strain dependence of the activation volume in b^3 for AZ31 alloy.

6.3 Microstructure of the AZ61 and AZ31 alloys prepared by rolling and ECAP

6.3.1 Microstructure of the AZ61 and AZ31 alloys after one rolling pass and after one rolling pass followed by ECAP

Light micrograph in Figure 6.36 shows a typical microstructure of the AZ61 specimens after one rolling pass. The microstructural observations revealed inhomogeneous grain size distribution, which corresponds to the microhardness variations along the longest sample axis (*Lukáč et al.*, 2007). Grain sizes vary in the range of 15–30 μm. Grains with precipitates or very small grains (~ 0.5 μm) observed at grain boundaries. Twins are present inside some grains. Shear structures throughout the grains (the deformed layers) are observed in AZ61 specimens after one rolling pass followed by ECAP, as seen in Figure 6.37. The microstructure is heterogeneous, with small grains having the size of 5 μm and less. Zones (layers) with the grain sizes of about 5 μm alternate with zones with grains of 1 μm.

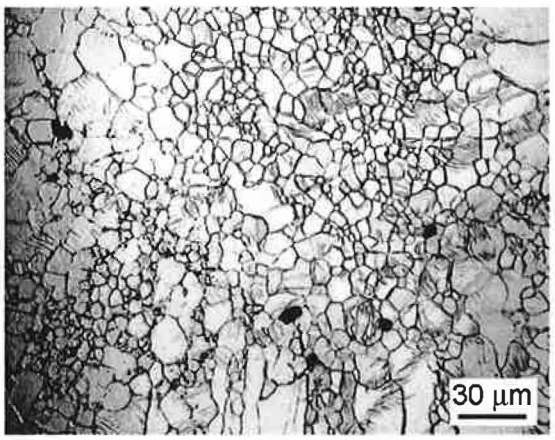

Figure 6.36: LM micrograph of the AZ61 alloy after one rolling pass.

A typical microstructure of the AZ31 specimens after one rolling pass is shown in Figure 6.38. The microstructure is heterogeneous with the grains varying between 5 and 50 μm. Twins are present inside many grains. Partial recrystallization after one rolling pass is observed. Figure 6.39 shows the microstructure of AZ31 specimens after one rolling pass followed by ECAP. It can be seen that the microstructure is heterogeneous.

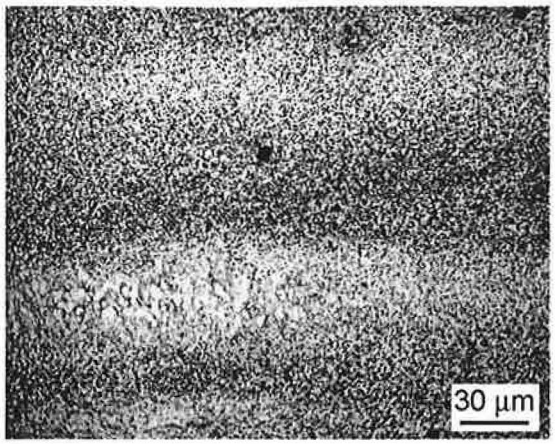

Figure 6.37: LM micrograph of the AZ61 alloy after one rolling pass followed by ECAP.

Small grains (about 3–5 μm) are arranged in deformed layers. Grain boundaries of the samples after rolling are well distinguishable in contrast to the samples after ECAP. It is obvious that the variations of microhardness (Figures 6.40–6.42) are caused by heterogeneous microstructures (*Lukáč et al.*, 2007). The observed shear band formation may be explained by the model proposed by *Ion et al.* (1982). The authors assumed that the shear zones form as a result of rotation dynamic recrystallization. It should be mentioned that the mechanism of this rotation dynamic recrystallization is different from conventional dynamic recrystallization.

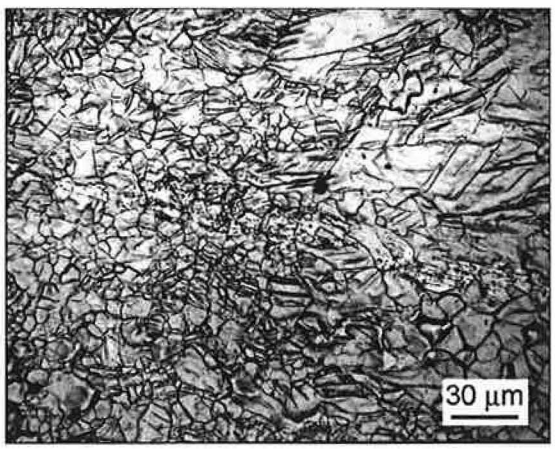

Figure 6.38: LM micrograph of the AZ31 alloy after one rolling pass.

As mentioned above, the heterogeneity of the microstructure of AZ61 and AZ31 alloys agrees with the measurements of the HV. Microhardness of the ECAP processed

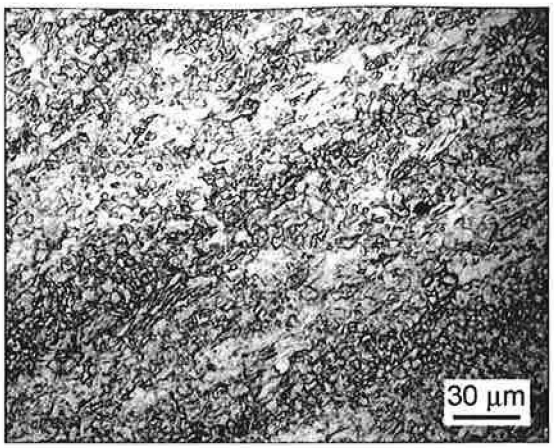

Figure 6.39: LM micrograph of the AZ31 alloy after one rolling pass followed by ECAP.

AZ61 alloy (Figure 6.40) is higher than that of the AZ61 alloy before ECAP (Figure 6.41). The increase in the microhardness after ECAP is caused by an increase in the dislocation density due to ECAP processing and/or grain refinement. The variation of microhardness of the AZ31 alloy after one rolling pass is shown in Figure 6.42.

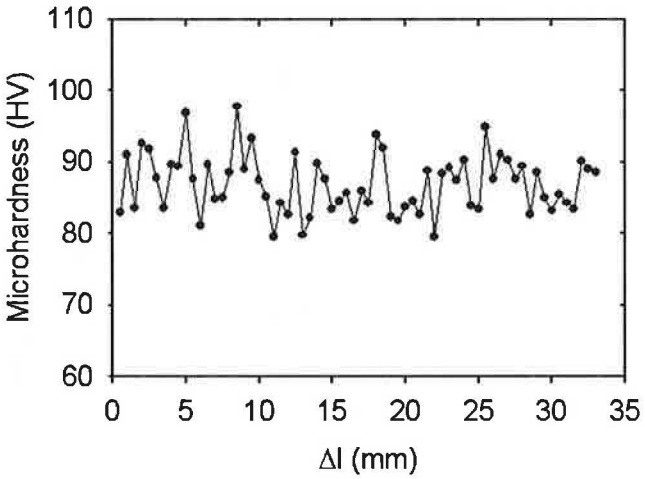

Figure 6.40: Microhardness of the AZ61 alloy after one rolling pass followed by ECAP measured along the longest specimen axis.

LM micrographs of the AZ61 and AZ31 specimens after one rolling pass and after one rolling pass followed by ECAP show that the mean grain size was reduced but the microstructure remained heterogeneous. The microhardness also exhibits heterogeneity.

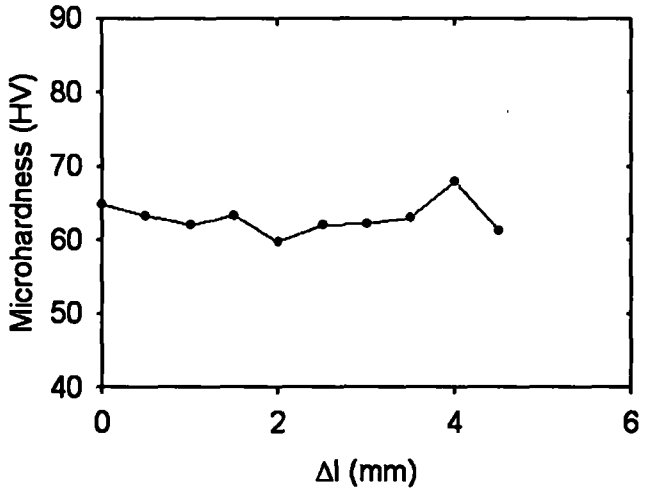

Figure 6.41: Microhardness of the AZ61 alloy after one rolling pass measured along the longest specimen axis.

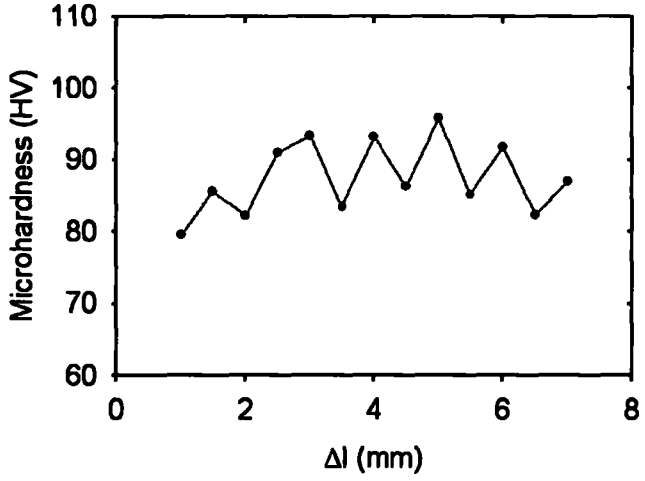

Figure 6.42: Microhardness of the AZ31 alloy after one rolling pass followed by ECAP measured along the longest specimen axis.

6.3.2 Substructure of the AZ61 and AZ31 alloys after one rolling pass and after one rolling pass followed by ECAP

The TEM observations presented in Figures 6.43, 6.44, 6.45, and 6.46 provide additional details to the light microscopy. Figure 6.43 shows TEM micrograph of the AZ61 specimens after one rolling pass. Figure 6.43a illustrates grains without dislocations and equiaxed subgrains. Small grains in a coarse grain are shown in Figure 6.43b.

TEM micrographs of the AZ61 specimens after one rolling pass followed by ECAP are presented in Figure 6.44. Grain structure is visible in Figure 6.44a, whereas Figure 6.44b shows high dislocation density and twins. Dynamic recrystallization takes place preferably in the regions with the highest dislocation density (Figure 6.44a). Similar results were reported by *Janeček et al.* (2007b).

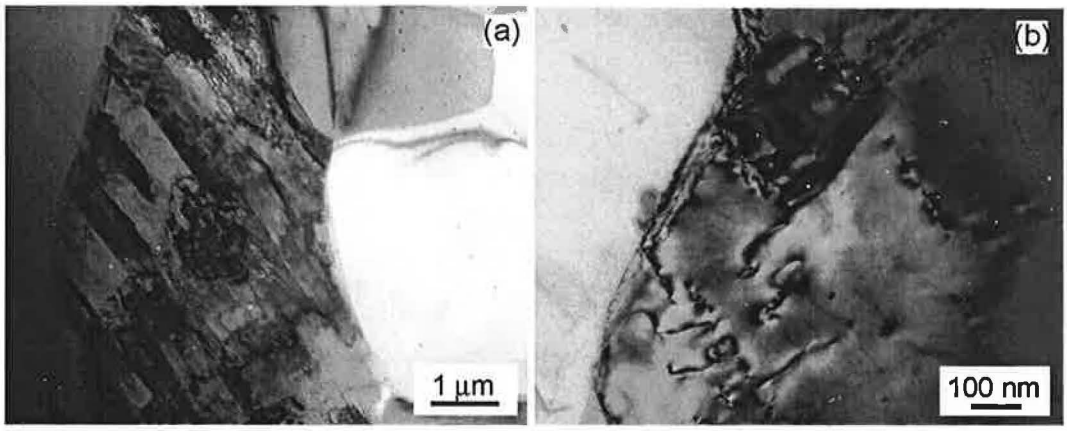

Figure 6.43: TEM micrograph (BF image) of the AZ61 alloy after one rolling pass. Grains without dislocations, subgrains (a), and small grains in a coarse grain (b) are visible.

TEM micrographs of the AZ31 specimens after one rolling pass are shown in Figure 6.45a. Grains with and without dislocations are shown in Figure 6.45a. Detailed view of the dislocations arranged inside the grain (Figure 6.45b) shows some dislocations pinned on precipitates. The rolled specimens indicate formation of new grains inside the original ones. *Janeček et al.* (2007a) performed electron diffraction analysis in the AZ31 rolled samples and found that most of grains were aligned along the [0001] zone axis. It means that basal planes, that were oriented in the original material, rotated during rolling to the position parallel to the rolling plane. Then, we can assume a similar process in our

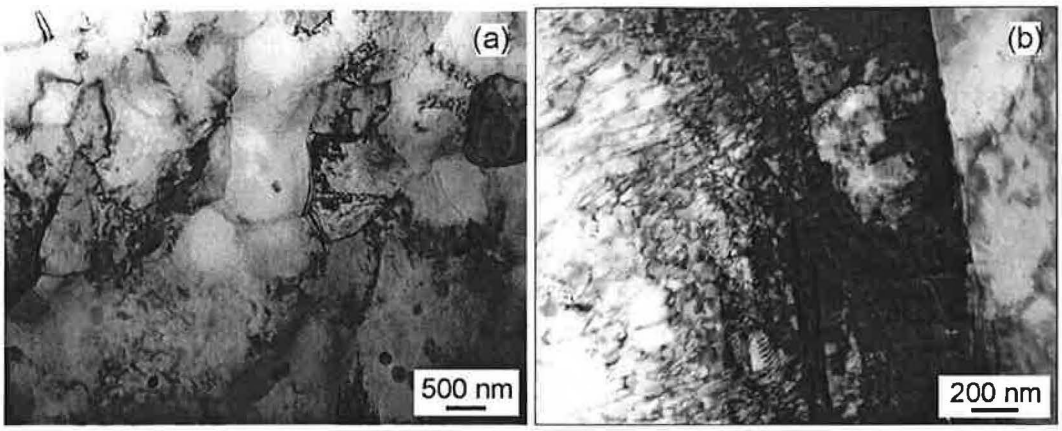

Figure 6.44: TEM micrograph (BF image) of the AZ61 alloy after one rolling pass followed by ECAP. Grain structure (a) and high dislocation density in a grain and twins (b) are visible.

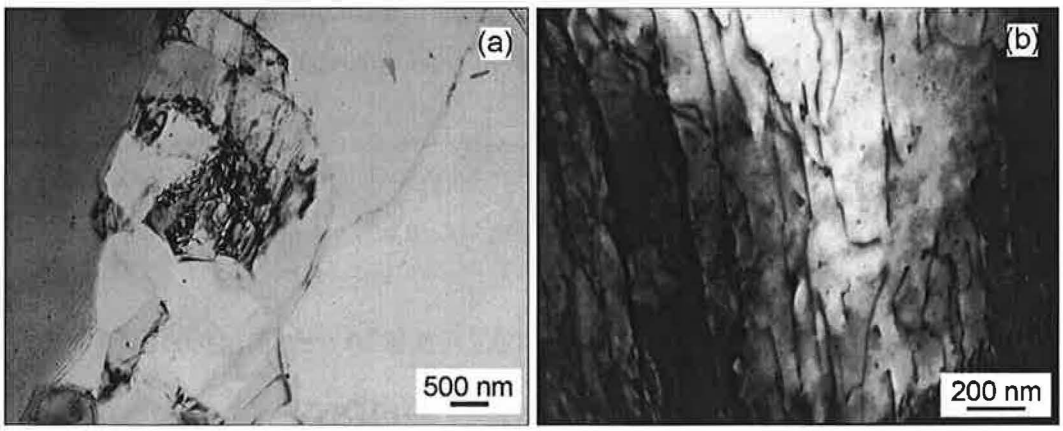

Figure 6.45: TEM micrograph (BF image) of the AZ31 alloy after one rolling pass. Grains with and without dislocations (a) and dislocations pinned on precipitates (b) are visible.

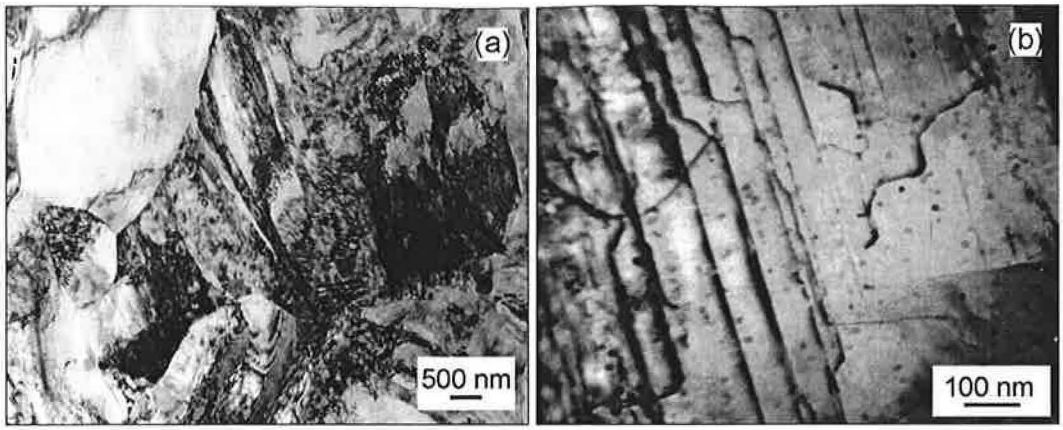

Figure 6.46: TEM micrograph (BF image) of the AZ31 alloy after one rolling pass followed by ECAP. Grains with a low dislocation density, grains without dislocations (a), and dislocation slide (b) are visible.

case. Grains with a low dislocation density and grains without dislocations are characteristic for the substructure of the AZ31 alloy after one rolling pass followed by ECAP (Figure 6.46a). Few dislocations visible in the grain interior indicate the occurrence of dynamic recrystallization. Elongated grains and twins are also visible. The presence of dislocations in some recrystallized grains is probably a result of large strains imposed by ECAP. Figure 6.46b illustrates a detailed view of dislocation slide. This may be the consequence of the high mobility of the atoms at the ECAP temperature (250 °C).

To conclude, TEM observations of the AZ61 and AZ31 specimens after one rolling pass and after one rolling pass followed by ECAP show grains with a high density of heterogeneously distributed dislocations and grains without dislocations. Some recrystallized grains were also found. The microhardness values exhibited heterogeneity.

6.3.3 Microstructure of the AZ61 and AZ31 alloys after three rolling passes and after three rolling passes followed by ECAP

A typical microstructure of the AZ61 alloy specimens after three rolling passes is shown in Figure 6.47. Zones (layers) with the grain sizes of about 1–5 μm alternate with zones with grains of about 20 μm. The mean grain size in this specimen is greater than in the specimen after one rolling pass. Twins are present inside many grains. Recrystallized

grain boundaries are also seen. The microstructure of the AZ61 specimen after three rolling passes followed by ECAP (Figure 6.48) is heterogeneous. No twins were observed in the microstructure. There are many grains with low angle grain boundaries. Similarly to the AZ61 alloy after three rolling passes, zones with the fine grains of about 1–5 μm alternate with zones with larger grains of about 20 μm. Specimens after three rolling passes contain many recrystallized grains with twins. However, the grains are not as small as in the case of the specimen after one rolling pass followed by ECAP. Thus, it is possible to suggest that ECAP processing (four passes in our case) does not reduce the size of the mostly recrystallized grains.

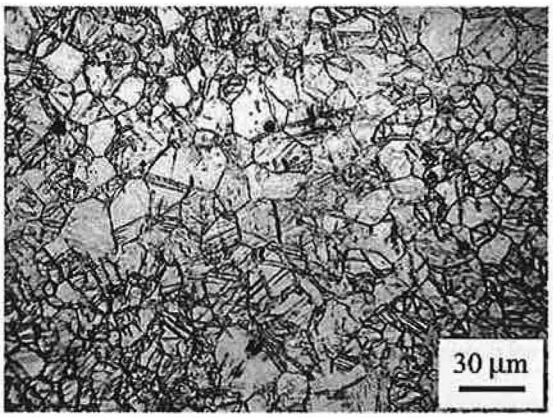

Figure 6.47: LM micrograph of the AZ61 alloy after three rolling passes.

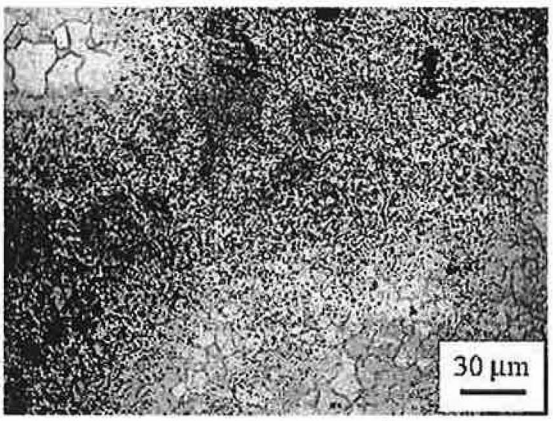

Figure 6.48: LM micrograph of the AZ61 alloy after three rolling passes followed by ECAP.

A typical microstructure of the AZ31 specimens after three rolling passes followed by

ECAP is shown in Figure 6.49. The microstructure is heterogeneous, with grains of 5–15 μm. Small grains (less than 5 μm in diameter) are arranged chaotically in the observed surface. There are no twins inside the grains.

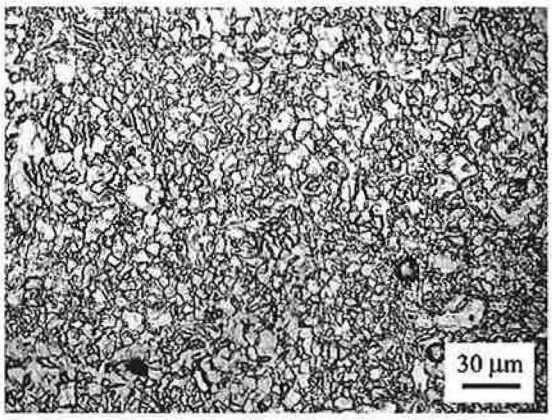

Figure 6.49: LM micrograph of the AZ31 alloy after three rolling passes followed by ECAP

Measurements of the HV confirm the heterogeneity of the microstructure of the AZ61 and AZ31 alloys after three rolling passes and after three rolling passes followed by ECAP as in the case of the samples after one rolling pass and after one rolling pass followed by ECAP. Microhardness of the AZ61 specimen after three rolling passes (Figure 6.50) is higher than that of the ECAP processed AZ61 specimen (Figure 6.51). The difference in the microhardness measured along and perpendicular to the longest ECAP specimen axis can be seen from Figures 6.51 and 6.52.

The microhardness of the AZ61 specimen after three rolling passes is higher than the microhardness of the AZ61 specimen after one rolling pass. However, the microhardness of the AZ61 specimen after three rolling passes followed by ECAP is lower than that of the AZ61 specimen after one rolling pass followed by ECAP. The microhardness increases with decreasing grain size.

The variation of microhardness of the AZ31 alloy after three rolling passes followed by ECAP is shown in Figure 6.53. The microhardness is lower than that of the AZ31 specimen after one rolling pass followed by ECAP. This also agrees with the determined grain size: the AZ31 samples after three rolling passes followed by ECAP have coarser grains than the AZ31 specimen after one rolling pass followed by ECAP.

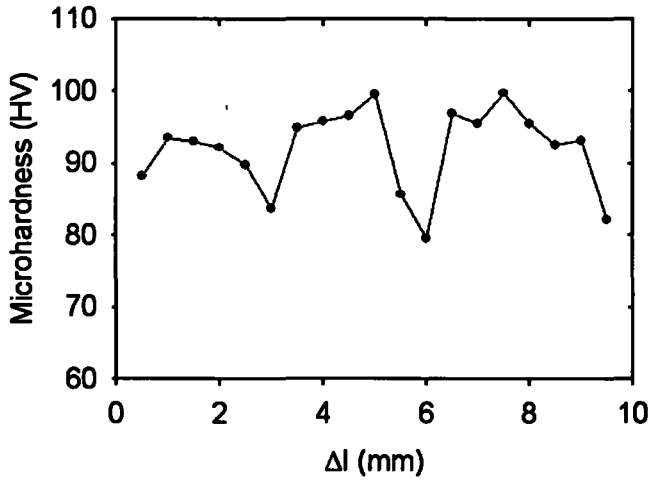

Figure 6.50: Microhardness of the AZ61 alloy after three rolling passes measured along the longest specimen axis.

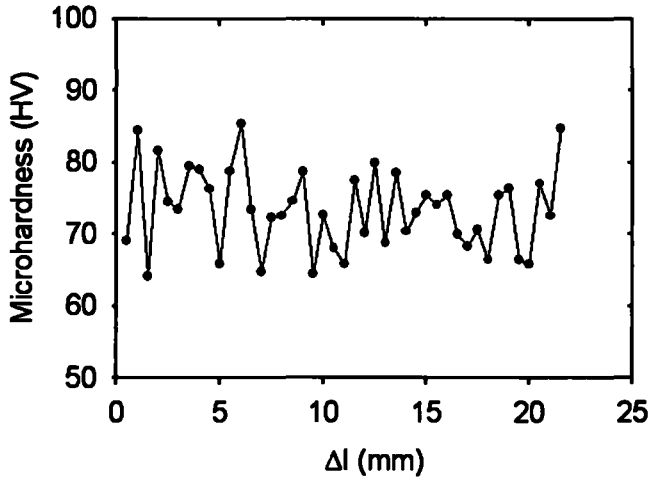

Figure 6.51: Microhardness of the AZ61 alloy after three rolling passes followed by ECAP measured along the longest specimen axis.

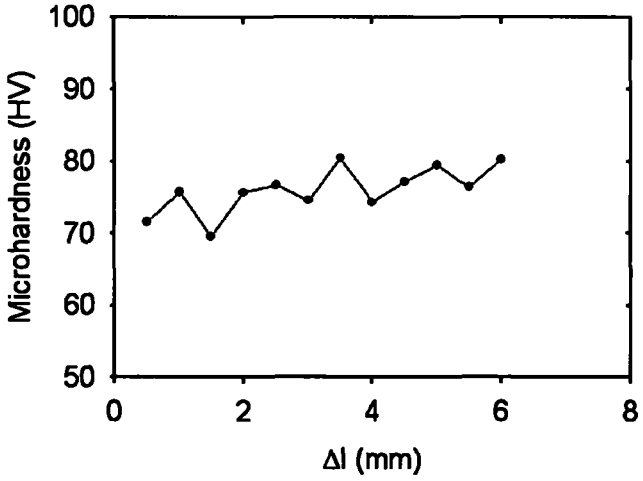

Figure 6.52: Microhardness of the AZ61 alloy after three rolling passes followed by ECAP measured perpendicular to the longest specimen axis.

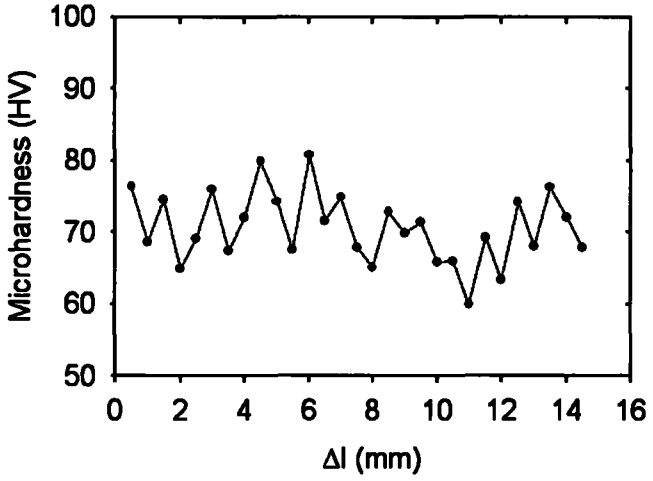

Figure 6.53: Microhardness of the AZ31 alloy after three rolling passes followed by ECAP measured along the longest specimen axis.

Finally, we can summarize that the heterogeneity of the microstructure of the AZ61 and AZ31 alloys after three rolling passes and after three rolling passes followed by ECAP was observed as in the case of the samples after one rolling pass and after one rolling pass followed by ECAP. The microhardness also exhibits heterogeneity and depends on the specimen grain size.

6.3.4 Substructure of the AZ61 and AZ31 alloys after three rolling passes and after three rolling passes followed by ECAP

Figure 6.54a illustrates small grains (500 nm) inside the coarse grain and a high dislocation density inside a coarse grain in the AZ61 specimens after three rolling passes. Dislocations that form tangles are seen in Figures 6.54b and c. Dislocations stored on coarser particles are shown in Figure 6.54d. The presence of grains without dislocations and grains with a low dislocation density are characteristic features of the specimen. TEM micrographs of the AZ61 specimens after three rolling passes followed by ECAP are presented in Figure 6.55. A grain containing subgrains and dislocations is visible in Figure 6.55a, whereas Figure 6.55b shows grains ($\sim$5 μm) with a low dislocation density and without dislocations.

TEM micrographs of the AZ31 specimen after three rolling passes followed by ECAP is shown in Figure 6.56. Typical dislocation interlacing inside the grain is in Figure 6.56a. The presence of subgrains with a relatively high dislocation density is illustrated by Figure 6.56b. As for the other states, grains with dislocations and grains without dislocations are present in this specimen.

Dislocations that form tangles were observed in the AZ61 specimens after three rolling passes. Grains without dislocations and grains with a low dislocation density are characteristic features for all specimens, which is the consequence of the recrystallization process.

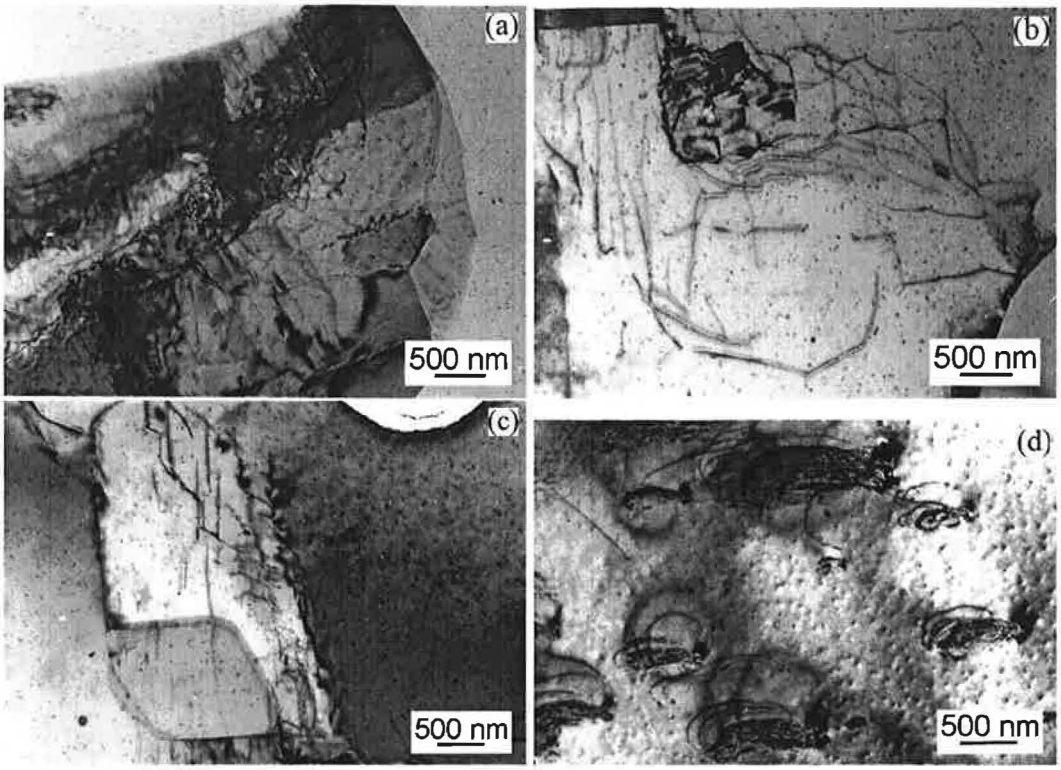

Figure 6.54: TEM micrograph of the AZ61 alloy after three rolling passes.

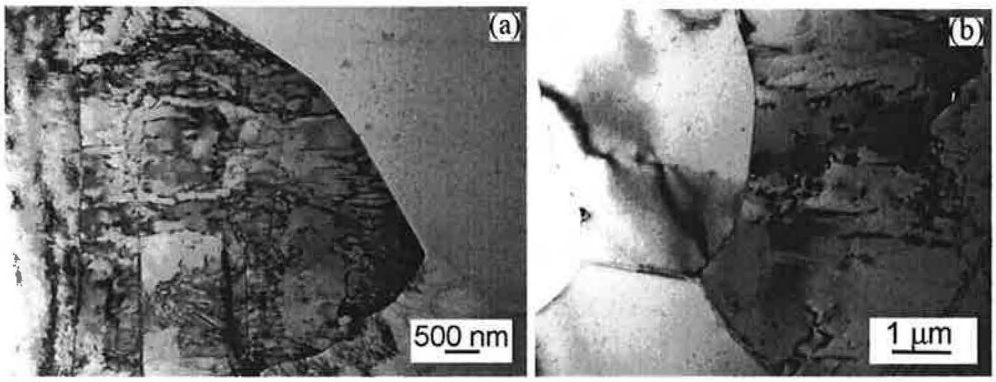

Figure 6.55: TEM micrograph of the AZ61 alloy after three rolling passes followed by ECAP.

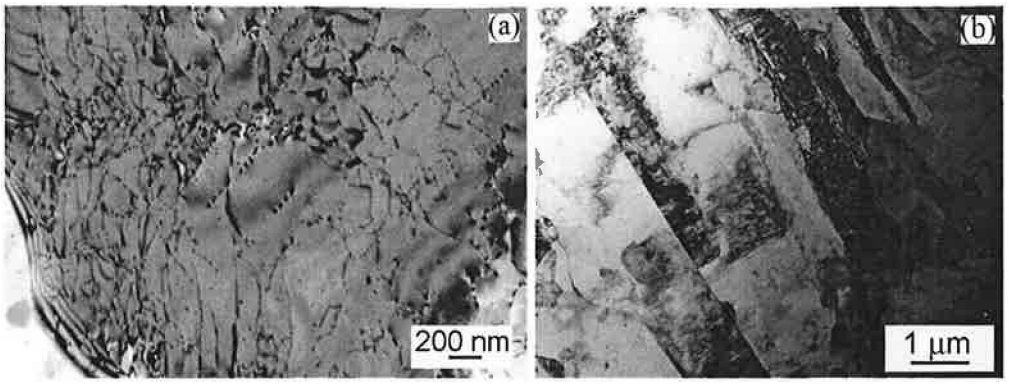

Figure 6.56: TEM micrograph of the AZ31 alloy after three rolling passes followed by ECAP.

6.4 Microstructure conditions for superplastic behaviour of QE22 and ZRE1 magnesium alloys

Microstructure investigations of the QE22 and ZRE1 in the state after the thermo-mechanical treatment (homogenisation, ageing and hot extrusion) show reduced average grain sizes in comparison to the as cast state (*Ryspaev et al.*, 2007). Average grain sizes of QE22 and ZRE1 alloys are higher than 100 μm in the as cast state, while in the state after the thermo-mechanical treatment the average sizes are 0.7 μm for QE22 alloy (Figure 6.57a) and 1.2 μm for ZRE1 alloy (Figure 6.57b). This can be seen from Figure 6.57 where coarse grains among smaller ones are situated. Moreover, the microstructures of both alloys after the thermo-mechanical treatment correspond to conditions required for the occurrence of structural superplasticity.

Superplastic deformation at elevated temperatures of the thermo-mechanically treated QE22 and ZRE1 alloys has been observed by *Wesling et al.* (2007) and *Ryspaev et al.* (2007). The elongation to failure ε_f measured for various strain rates at 420 °C is introduced in Figure 6.58 together with the values of the strain rate sensitivity parameter m. The values of the parameter m were estimated using the tensile tests with stepwise changes of the strain rate. A very good correlation between the elongation to failure and the parameter m is obvious (Figure 6.58). It is interesting to note that the elongation to failure and the parameter m values in QE22 and ZRE1 were found to be higher than those for superplastic AZ91 and AE42 Mg alloys investigated by *Wesling et al.* (2007).

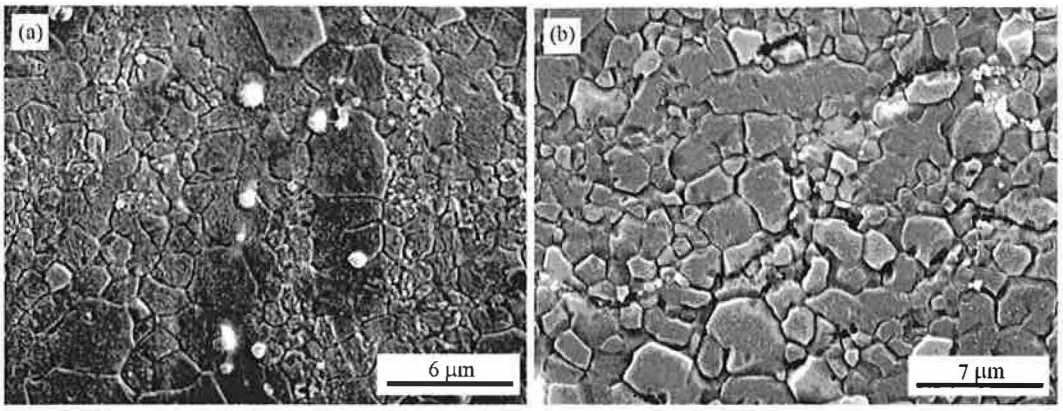

Figure 6.57: SEM micrograph of the QE22 alloy (a) and ZRE1 (b) obtained from the section perpendicular to the extrusion direction.

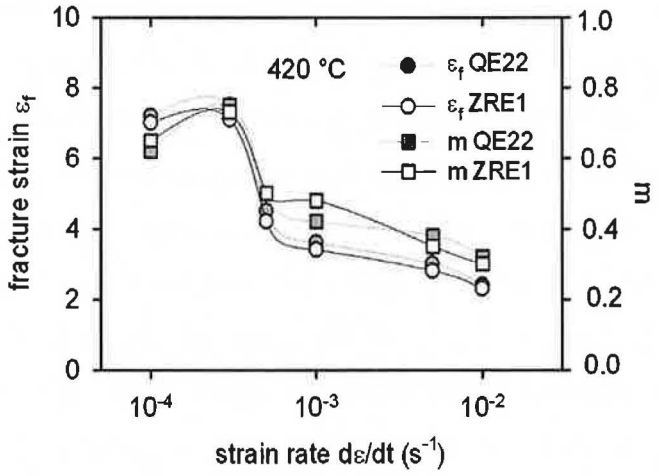

Figure 6.58: Strain rate dependence of the elongation to failure and the strain rate sensitivity obtained at 420 °C.

In order to understand possible mechanisms and to investigate microstructure conditions for superplastic deformation of QE22 and ZRE1 alloys, the dislocation substructures of the alloys were investigated in as cast and after the thermo-mechanical treatment states.

Microstructure of the as cast QE22 alloy consists of α-grains decorated at grain boundaries by the second phase particles (*Wesling et al.*, 2007). TEM revealed chains of smaller particles containing Nd and Ag located at grain boundaries (Figure 6.59). These particles were dissolved during homogenisation annealing (470 °C for 10 h). TEM showed only groups of small and bigger non-dissolved zirconium particles that are visible in Figure 6.60a. These Zr particles are very stable and they were not influenced by the k homogenisation treatment. Dislocation network and fine particles of Zr are also visible in Figure 6.60b. After thermo-mechanical treatment (age annealing at 350 °C for 10 h and hot extrusion) the particles at grain boundaries appeared again (see Figure 6.61) and they were found together with the smaller Zr particles also after deformation at 420 °C. On the other hand, no dislocations were found in the deformed sample. Interior of grains after deformation at 420 °C was clear without dislocations. This behaviour may be explainend as follow. Deformation at 450 °C is superplastic. The main mechanism of superplastic deformation is grain boundary sliding. The dislocation mechanism is restricted. The changes in the grain shapes may be attributed to diffusional flow in the vicinity of the grain boundaries. Round particles appeared after the thermo-mechanical treatment were identified as Mg_3 (Ag, Nd) phase. There are two kinds of round particles of Mg_3 (Ag, Nd) phase: coarser particles with an average diameter of 0.2–0.5 m lying along the grain boundaries and at the triple points and smaller particles with an average diameter of 50-100 nm situated in the grains interior. The obtained results of the Mg_3 (Ag, Nd) phase distribution agree with results presented by *Svoboda et al.* (2000) who investigated the creep behaviour of QE22 alloy; similar two particle sizes were found in QE22 alloy after T6 treatment. Particles placed at grain boundaries contribute to the microstructure stability, hereby they hinder to the grain growth during heating in the deformation machine and during deformation at higher temperature. Precipitates at grain boundaries were found also after the high temperature deformation practically unaffected by the 2 h exposition at 420 °C.

Similar situation has been found also in ZRE1 alloy. The microstructure of the al-

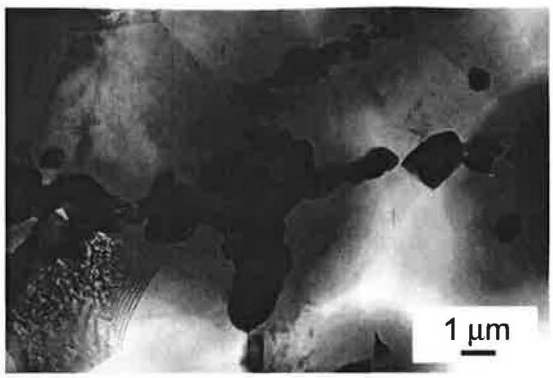

Figure 6.59: TEM micrograph of the as cast QE22 magnesium alloy showing particles of Mg_3 (Ag, Nd) phase.

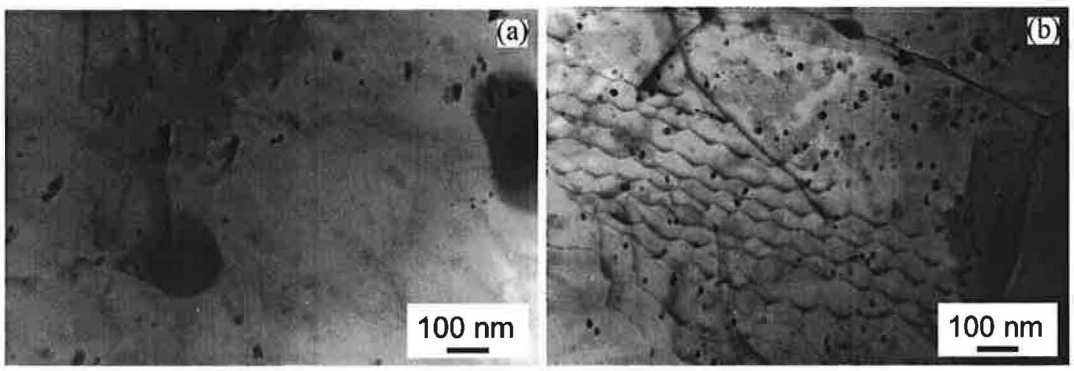

Figure 6.60: TEM micrographs of the QE22 magnesium alloy after the thermo-mechanical treatment: (a) precipitation of Zr, (b) partially visible dislocation network and fine particles of Zr.

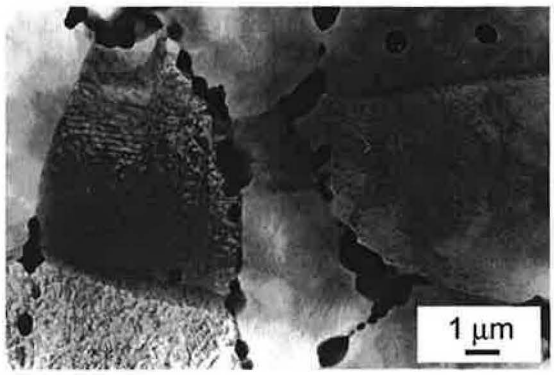

Figure 6.61: TEM micrographs of the QE22 magnesium alloy after thermo-mechanical treatment showing particles of Mg_3 (Ag, Nd) phase.

loy after thermo-mechanical treatment (Figure 6.62a) exhibits small grains with small particles at the grain boundaries, very probably T phase. *Wei et al.* (1995) studied the solidification path and phase constituents of alloys in the magnesium rich corner of the Mg-Zn-misch metal system. They found that the T phase has a c-centred orthorhombic crystal structure which exhibits a wide range composition of Mg, Zn and RE depending on the alloy composition. The Zr particles (200–100 nm) were observed in the whole volume. In the sample after high temperature exposition during deformation, the same particles were found; T phase at grain boundaries and small Zr particles in the grains interior (Figure 6.62b).

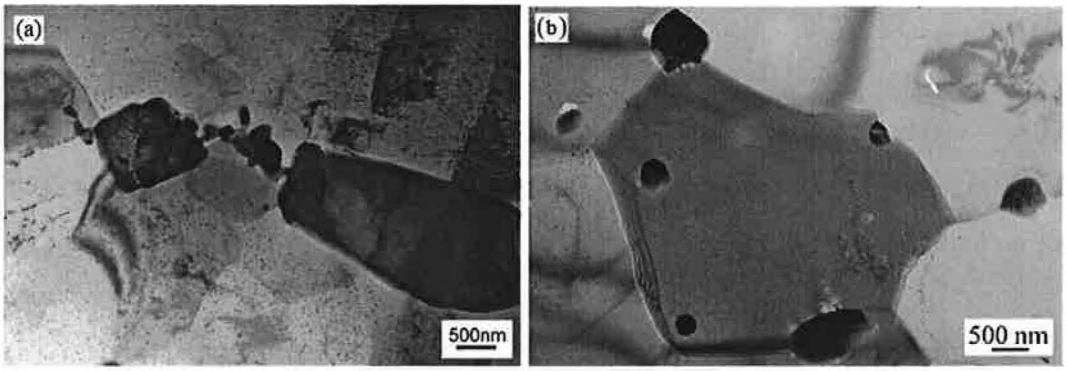

Figure 6.62: Particles located at grain boundaries in the aged ZRE1 sample (a), particles in the grain boundary after deformation at 420 °C. Small Zr particles inside the grain (b).

The high values of the elongation to failure and the strain rate sensitivity are caused by the fine grain size of about 1 μm. After the thermo-mechanical treatment, fine grain structures with a grain size in order of 0.7 μm (QE22) and 1.2 μm (ZRE1) were observed. Small Zr particles in the Mg matrix refine grain size to $\sim$1 μm. Very high stability of the grain structure is supported by the stable particles in the grain boundaries: Mg_3 (Ag, Nd) and T phases in the QE22 and ZRE1 alloys, respectively.

Chapter 7

Conclusions

The thesis was devoted to the investigation of the internal structure and mechanical properties of selected magnesium alloys and composites. The investigated materials — AS21 composite and zirconium free (AS21, AZ31, AZ61) and zirconium containing (QE22 and ZRE1) alloys — were exposed to a variety of thermal and mechanical loading and thermo-mechanical treatment.

Different deformation processes in the AS21 composite matrix acting during tension as well as compression straining were considered. While the tensile deformation is controlled mainly by the dislocation motion, the compression deformation is realized at low strains in the vicinity of the yield stress almost by twinning. Investigations of the AS21 alloy and its composite qualitatively confirmed the relation between the dislocation structure and mechanical properties. SR tests conducted on the AS21 alloy and composite deformed in compression show that the internal stress forms a substantial part of the applied stress at low deformation temperatures and it increases with the strain. The internal stress depends on the dislocation density (deformation gradient) in the material and decreases with strain at higher temperatures as a result of recovery processes (dislocation annihilation). The values of the activation volume of the AS21 composite are very similar to those in AS21 alloy. Consequently, the thermally activated processes in the alloy and in the composite are the same.

A significant homogeneity of the microstructure is achieved with increasing deformation temperature in plastically deformed AZ31 alloys. Recrystallized grains and the

absence of twins are characteristic for specimens deformed at higher temperatures in contrast to the specimens deformed at room temperature and 100 °C, where non-recrystallized grains, twins, and high dislocation density were observed. The amount of the recrystallized grains increases with increasing deformation temperature. A relation between the stress and dislocation density was confirmed. The activation volume increases with increasing temperature, which indicates the presence of the recovery processes, the decrease of the dislocation density, and possibly the dynamic recrystallization.

The investigation of the substructure evolution of the modified commercial magnesium alloys AZ31 and AZ61 prepared by rolling and ECAP revealed that the mean grain size during rolling and ECAP was reduced but the microstructure remained heterogeneous. Grains with a high density of heterogeneously distributed dislocations and grains without dislocations were observed. Some recrystallized grains were also found. The microhardness values also exhibited heterogeneity. A relation between the sample preparation (i.e. the imposed strain) and the dislocation density was confirmed.

Microstructure analysis of QE22 and ZRE1 magnesium alloys showed the fine grain structure with the grain size of 0.7 μm (QE22) and 1.2 μm (ZRE1) which is the good condition for the superplasticity. Fine grain structure is caused by small Zr particles in the Mg matrix. Very high stability of the grain structure was found which is supported by the existence of stable particles of Mg_3 (Ag, Nd) phase and T phase in grain boundaries. Precipitates in the grain boundaries were found also after the superplastic deformation. Hence, a qualitative relation between the microstructure and substructure and superplasticity was found.

Bibliography

Agnew, S. R., and O. Duygulu (2003), A mechanical understanding of the formability of magnesium: examining the role of temperature on the deformation mechanisms, *Mater. Sci. Forum, 419–422*, 177–188.

Agnew, S. R., and O. Duygulu (2005), Plastic anisotropy and the role of non-basal slip in Mg alloy AZ31B, *Int. J. Plasticity, 21*, 1161–1193.

Agnew, S. R., M. H. Yoo, and C. N. Tomé (2001), Application of texture simulation to understanding mechanical behavior of Mg and solid solution alloys containing Li or Y, *Acta Mater., 49*, 4277–4289.

Agnew, S. R., J. A. Horton, and M. H. Yoo (2002), Transmission electron microscopy investigation of $<c+a>$ dislocations in Mg and α solid solution Mg-Li alloys, *Metall. Mater. Trans. A, 33*, 851–858.

Agnew, S. R., C. N. Tomé, D. W. Brown, T. M. Holden, and S. C. Vogel (2003), Study of slip mechanisms in a magnesium alloy by neutron diffraction and modeling, *Scripta Mater., 48*, 1003–1008.

Aikin, R. M. J., and L. Christodoulu (1991), The role of euiaxed particles on the yield stress of composites, *Scripta Metall. Mater., 25*, 9–14.

Albright, D. (1995), Current trends in the development and utilization of magnesium alloys, in *IMA Proceedings*, pp. 30–37.

Ando, S., and H. Tonda (2000), Non-basal slip in magnesium-lithium alloy single crystals, *Mater. Trans. JIM, 41*, 1188–1191.

Ando, S., M. Tanaka, and H. Tonda (2003), Pyramidal slip in magnesium alloy single crystal, *Mater. Sci. Forum, 419–422*, 87–92.

Arsenault, R. J., and R. M. Fisher (1983), Microstructure of fiber and particulate SiC in 6061 Al composites, *Scripta Metall., 17*, 67–71.

Arsenault, R. J., and N. Shi (1986), Dislocation generation due to differences between the coefficients of thermal expansion, *Mater. Sci. Eng., 81*, 175–187.

Arsenault, R. J., L. Wang, and C. R. Feng (1991), Strengthening of composites due to microstructural changes in matrix, *Acta Metall. Mater., 39*, 47–57.

Ashby, M. F. (1970), The deformation of plastically non-homogeneous materials, *Phil. Mag.*, *21*, 399–424.

Avedesian, M. M., and H. Baker (1999), *Magnesium and Magnesium Alloys*, ASM International, Metal Park.

Balík, J., P. Lukáč, J. Bohlen, and K. U. Kainer (2007), Effect of temperature on tensile properties of hot rolled AZ31 Mg alloy sheets, *Kovove Mater.*, *45*, 135–140.

Barlow, C. Y., and N. Hansen (1995), Dislocation configurations in metal-matrix composites correlated with numerical predictions, *Acta Metall. Mater.*, *43*, 3633–3648.

Barlow, C. Y., and Y. L. Liu (1998), Microstructure, strain fields and flow stress in deformed metal matrix composites, *Acta Mater.*, *46*, 5807–5817.

Beer, S., G. Frommeyer, and E. Schmid (1992), Development of Mg-Mg_2Si light weight alloys, in *Conf. on Magnesium Alloys and Their Applications*, pp. 317–324.

Ben-Hamu, G., D. Eliezer, K. S. Shin, and S. Cohen (2007), The relation between microstructure and corrosion behavior of Mg-Y-Zr alloys, *J. Alloys Comp.*, *431*, 269–276.

Bohlen, J., F. Chmelík, F. Kaiser, D. Letzig, P. Lukáč, and K. U. Kainer (2002), Acoustic emission generation during tensile deformation of an AZ31 magnesium sheet, *Kovove Mater.*, *5*, 290–297.

Bohlen, J., F. Chmelík, P. Dobroň, P. Lukáč, and K. U. Kainer (2004), Acoustic emission during testing of magnesium AZ alloys, *J. Alloys Comp.*, *378*, 214–219.

Bohlen, J., P. Dobroň, J. Swiostek, D. Letzig, F. Chmelík, P. Lukáč, and K. U. Kainer (2007), On the influence of the grain size and solute content on the AE respounse of magnesium alloys tested in tension and compression, *Mater. Sci. Eng. A*, *462*, 302–206.

Bronfin, B., M. Katsir, and E. Aghion (2001), Preparation and solidification features of AS21 magnesium alloy, *Mater. Sci. Eng. A*, *302*, 46–50.

Cáceres, C. H., T. Sumimoto, and M. Veidt (2003), Pseudoelastic behaviour of cast magnesium AZ91 alloy under cyclic loading-unloading, *Acta Mater.*, *51*, 6211–6218.

Caillard, D., and J. L. Martin (2003), *Thermally activated mechanisms is crystal plasticity*, Elsevier.

Calhoun, R. B., and D. C. Dunand (2000), Dislocations in metal matrix composite, in *Comprehensive Composite Materials*, edited by A. Kelly and C. Zweben, Pergamon Press, Amsterdam.

Calhoun, R. B., and A. Mortensen (1999), Equilibrium shape of prismatic dislocation loops under uniform stress, *Acta Mater.*, *47*, 2357–2365.

Chawla, K. K. (1993), Metal matrix composites, in *Structure and Properties of Composites*, edited by T. W. Chou, Springer-Verlag, Berlin.

Chmelík, F., J. Kiehn, P. Lukáč, B. L. Mordike, and K. U. Kainer (1998), Acoustic emission and dilatometry for non-destructive characterisation of microstructural changes in Mg based metal matrix composites submitted to thermal cycling, *Scripta Mater.*, *38*, 81–87.

Chmelík, F., P. Lukáč, J. Kiehn, B. L. Mordike, K. U. Kainer, and T. G. Langdon (2002), Characteristics of thermal cycling in a magnesium alloy composite, *Mater. Sci. Eng. A*, *325*, 320–323.

Delannay, F. (2000), Thermal stresses and thermal expansion in MMCs, in *Comprehensive Composite Materials*, edited by A. Kelly and C. Zweben, Pergamon Press, Amsterdam.

Dobroň, P., J. Bohlen, F. Chmelík, P. Lukáč, D. Letzig, and K. U. Kainer (2007), Acoustic emission during stress relaxation of pure magnesium and AZ magnesium alloys, *Mater. Sci. Eng.*, *462*, 307–310.

Dotsenko, V. I. (1979), Stress relaxation in crystals, *phys. stat. sol.(b)*, *93*, 11–43.

Drápala, J., K. Kuchař, L. Tomášek, and Z. Trojanová (2004), *Horčik, jeho slitiny a binárni systemy horčik-přiměs*, Vysoká škola báňská - Technická univerita Ostrava.

Dumant, X., F. Fenot, and G. Regazzoni (1988), in *Proceed. of 9 th Riso Conference on Mechanical and Physical Behaviour of Metallic and Ceramic Composites*, pp. 349–356.

Feltham, P. (1963), *Phys. Stat. Sol.*, *3*, 1340.

Friedrich, E. F., and B. L. Mordike (2006), *Magnesium Technology, Metallurgy, Design Data, Applications*, Springer-Verlag, Berlin, Heidelberg.

Hart, E. (1967), Theory of the tensile test, *Acta Metall.*, *15*, 351–355.

Hellmig, R. J., T. T. Lamark, M. V. Popov, M. Janeček, and F. Chmelík (2007), Influence of equal-channel angular pressing on the acoustic emission behaviour of magnesium alloy AZ31 under compression, *Mater. Sci. Eng. A*, *462*, 111–115.

Hollrigl-Rosta, F. (1980), Magnesium in the Volkswagen, *Light Met. Age*, *8*, 22–29.

Hu, X. S., K. Wu, M. Y. Zheng, W. M. Gan, and X. J. Wang (2007), Low frequency damping capacities and mechanical properties of MgSi alloys, *Mater. Sci. Eng. A*, *452–453*, 374–379.

Ion, S. E., F. J. Humphreys, and S. H. White (1982), Dynamic recrystallisation and the development of microstructure during the high temperature deformation of magnesium, *Acta Metall.*, *30*, 1909–1919.

Janeček, M., T. Lamark, and Y. Estrin (2004), Structural transformations in die–cast magnesium alloy AS21X, in *Letná škola únavy materialov*, pp. 173–176.

Janeček, M., R. Král, P. Dobroň, F. Chmelík, V. Šupík, and F. Holländer (2007a), Mechanisms of plastic deformation in AZ31 magnesium alloy investigated by acoustic emission and transmission electron microscopy, *Mater. Sci. Eng. A*, *426*, 311–315.

Janeček, M., M. Popov, M. G. Krieger, R. J. Hellmig, and Y. Estrin (2007b), Mechanical properties and microstructure of a Mg alloy AZ31 prepared by equal-channel angular pressing, *Mater. Sci. Eng. A*, *426*, 116–120.

Kaibyshev, O. A. (1992), *Superplasticity of alloys, intermetallics and ceramics*, Springer Verlag, Berlin.

Kiehn, J., Z. Trojanová, and P. Lukáč (1997), Effect of thermal cycling on the damping behaviour of Mg matrix composites, *Key Eng. Mater.*, *127–131*, 993–1000.

Kim, C. T., J. K. Lee, and M. R. Plichta (1990), Plastic relaxation of thermoelastic stress in aluminum/ceramic composites, *Metall. Mater. Trans. A*, *21*, 673–682.

Kobayashi, T., J. Koike, T. Mukai, M. Suzuki, H. Watanabe, K. Maruyama, and K. Higashi (2003), Anomalous activity on nonbasal dislocations in AZ31 Mg alloys at room temperature, *Mater. Sci. Forum*, *419–422*, 231–236.

Kocks, U. F., A. S. Argon, and M. F. Ashby (1975), Thermodynamics and kinetics of slip, *Progr. Mater. Sci.*, *19*, 1.

Koike, J., and R. Ohyama (2005), Geometrical criterion for the activation of prismatic slip in AZ61 Mg alloy sheets deformed at room temperature, *Acta Mater.*, *53*, 1963–1972.

Koike, J., T. Kobayashi, T. Mukai, H. Watanabe, M. Suzuki, K. Maruyama, and K. Higashi (2003a), The activity of non-basal slip systems and dynamic recovery at room temperature in fine-grained AZ31B magnesium alloys, *Acta Mater.*, *51*, 2055–2064.

Koike, J., R. Ohyama, T. Kobayashi, M. Suzuki, and K. Maruyama (2003b), Grain boundary sliding in AZ31 magnesium alloys at room temperature to 523 K, *Mater. Trans.*, *44*, 445–451.

Kouzeli, M., and A. Mortensen (2002), Size dependent strengthening in particle reinforced aluminium, *Acta Mater.*, *50*, 39–51.

Lee, J. K., Y. Y. Earmme, H. I. Aaronson, and K. C. Russell (1980), Plastic relaxation of the transformation strain energy of a misfitting spherical precipitate: ideal plastic behavior, *Metall. Trans.*, *11A*, 1837–1847.

Li, Q., Q. Wang, Y. Wang, X. Zeng, and W. Ding (2007), Effect of Nd and Y additions on microstructure and mechanical properties of as-cast Mg-Zn-Zr alloy, *J. Alloys Comp.*, *427*, 115–123.

Linholt, H. (1994), Strengthening and its mechanisms, in *Mechanical Properties of Metallic Composites*, edited by S. Ochiai, Marcel Deccer Inc., USA.

Loretto, M. H., and R. E. Smallman (1975), *Defect Analysis in Electron Microscopy*, Chapman and Hall, London.

Lukáč, P., F. Chmelík, U. Roos, K. U. Kainer, and B. L. Mordike (1995), Acoustic emission during thermal cycling of a Mg-based metal matrix composite, in *2nd International Symposium of Advanced Materials and Technologies, "Innovation 95"*, pp. 280–282.

Lukáč, P., R. Kocich, M. Greger, O. Padalka, and Z. Száraz (2007), Microstructure of AZ31 and AZ61 Mg alloys prepared by rolling and ECAP, *Kovove Mater., A 387–389.*

Luo, Z. P., S. Q. Zhang, and Y. L. Tang (1993), Quasicrystals in as-cast Mg-Zn-RE alloys, *Scripta Metall. Mater., 28*, 1513–1518.

Luo, Z. P., S. Q. Zhang, Y. L. Tang, and D. S. Zhao (1995), On the stable quasicrystals in slowly cooled Mg-Zn-Y alloys, *Scripta Metall. Mater., 32*, 1411–1416.

Luster, J. W., M. Thumann, and R. Baumann (1993), Mechanical properties of aluminium alloy 6061-Al_2O_3 composites, *Mater. Sci. Technol., 9*, 853–862.

Mabuchi, M. and K. Higashi (1996), Strengthening mechanisms of Mg-Si alloys, *Acta Mater., 44*, 4611–4618.

Mann, G., J. Griffiths, and C. Cáceres (2004), Hall-Petch parameters in tension and compression in cast Mg2Zn alloys, *J. Alloys Comp., 378*, 188–191.

Máthis, K., K. Nyilas, A. Axt, I. Dragomir-Cernatescu, T. Ungár, and P. Lukáč (2004), The evolution of non-basal dislocations as a function of deformation temperature in pure magnesium determined by X-ray diffraction, *Acta Mater., 52*, 2889–2894.

Máthis, K., F. Chmelík, M. Janeček, B. Hadzima, Z. Trojanová, and P. Lukáč (2006), Investigating deformation processes in AM60 magnesium alloy using the acoustic emission technique, *Acta Mater., 54*, 5361–5366.

Meza-García, E., P. Dobroň, J. Bohlen, D. Letzig, F. Chmelík, and P. Lukáč (2007), Deformation mechanisms in an AZ31 cast magnesium alloy as investigated by the acoustic emission technique, *Mater. Sci. Eng. A, 462*, 297–301.

Mordike, B. L., and P. Lukáč (2006), Physical metallurgy, in *Magnesium Technology*, edited by B. Mordike and H. Friedrich, Springer–Verlag, Berlin.

Mugrabi, H., and H. W. Höppel (2001), *Structure and Mechanical Properties of Nanophase Materials-Theory and Computer Simulation vs. Experiment*, MRS, Warendale.

Obara, T., H. Yoshinaga, and S. Morozumi (1973), $\{11\bar{2}2\} <11\bar{2}3>$ slip system in magnesium, *Acta Metall., 21*, 845–853.

Olsson, M., A. E. Giannakopoulos, and S. Suresh (1995), Elastoplastic analysis of thermal cycling ceramic particles in a metallic matrix, *J. Mech. Phys. Solids, 43*, 1639–1671.

Ono, K. (1968), Temperature dependence of dispersed barrier hardening, *J. Appl. Phys., 39*, 1803–1806.

Padmanabhan, K. A., and G. Davies (1988), *Superplasticity*, Springer Verlag, Berlin.

Pekguleryuz, M. O., and A. A. Kaya (2003), Creep resistant magnesium alloys for powertrain applications, *Adv. Eng. Mater.*, *5*, 866–878.

Pelcová, J., B. Smola, and I. Stulíková (2007), Influence of processing technology on phase transformations in a rare-earth-containing Mg-Zn-Zr alloy, *Mater. Sci. Eng. A*, *462*, 334–338.

Polmear, L. J. (1991), *Light Alloys — Metallurgy of Light Metals*, 3rd. Ed., Arnold, London.

Polmear, L. J. (1994), Magnesium alloys and applications, *Mater. Sci. Techn.*, *10*, 1–16.

Raynor, G. V. (1959), *The Physical Metallurgy of Magnesium and its Alloys*, Pergamon Press, New York.

Rosochowski, A. (2000), Microstructural evolution during creep of the Mg-Al alloy, *Solid State Phenomena*, *171-174*, 609–619.

Ryspaev, T., Z. Trojanová, O. Padalka, and W. Wesling (2007), Microstructure conditions for superplastic properties of QE22 and ZRE1 magnesium alloys, *Mater. Letters*, *submitted.*

Smola, B. (1983), *Transmisní elektronová mikroskopie ve fyzice pevných látek*, SPN, Praha.

Somekawa, H., A. Singh, and T. Mukai (2003), Fracture toughness in magnesium alloys produced by severe plastic deformation, *Met. Soc.*, *52*, 603–609.

Stohr, J. F., and J. P. Poirier (1972), Electron microscope study of pyramidal slip $\{11\bar{2}2\} < 11\bar{2}3 >$ in magnesium, *Phil. Mag.*, *25*, 1313–1329.

Svoboda, M., M. Pahutová, F. Moll, J. Březina, and V. Sklenička (2000), Microstructure and creep behaviour of SiC particulate reinforced QE22 composite, in *Magnesium Alloys and Their Applications*, pp. 234–239.

Tang, Y. L., D. S. Zhang, Z. P. Luo, N. F. Shen, and S. Q. Zhang (1993), Morphology and the structure of quasicrystal phase in as-cast and melt-spun Mg-Zn-Y-Zr alloys, *Scripta Metall. Mater.*, *29*, 955–958.

Tonda, H., and S. Ando (2002), Effect of temperature and shear direction on yield stress by $\{11\bar{2}2\} < \bar{1}\bar{1}23 >$ slip in hcp metals, *Metall. Mater. Trans. A*, *33*, 831–836.

Trojanová, Z., and P. Lukáč (2005), Compressive deformation behaviour of magnesium alloys, *J. Mater. Process. Techn.*, *162–163*, 416–421.

Trojanová, Z., A. Rudajevová, O. Padalka, M. Janeček, and P. Lukáč (2006), Deformation history effect in an AS21 magnesium alloy based composite, *Kovove Mater.*, *44*, 283–289.

Trojanová, Z., P. Lukáč, and K. U. Kainer (2007a), Stress relaxation in AX41 magnesium aloy studied at elevated temperatures, *Adv. Eng. Mater.*, *9*, 370–374.

Trojanová, Z., P. Lukáč, and Z. Száraz (2007b), Strengthening and recovery in AX41 magnesium alloy reinforced with short Saffil fibres, *Kovove Mater.*, *45*, 283–291.

Vedula, M., R. N. Pangborn, and R. A. Queeney (1988), Modification of residual thermal stress in a metal-matrix composite with the use of a tailored interfacial region, *Composites*, *19*, 55–60.

Vogelsang, M., R. J. Arsenault, and R. M. Fisher (1986), An in situ HVEM study of dislocation generation at Al/SiC interfaces in metal matrix composites, *Metall. Mater. Trans. A*, *17*, 379–389.

von Mises, R. (1928), Mechanik der plastischen Formänderung von Kristallen, *Z. Angew. Math. Mech.*, *8*, 161–185.

Wei, L. Y., and G. L. Dunlop (1997), Solidification behaviour and phase constituents of cast Mg-Zn-misch metal alloys, *J. Mater. Sci.*, *32*, 3335–2240.

Wei, L. Y., G. L. Dunlop, and H. Westengen (1995), The intergranular microstructure of cast Mg-Zn and Mg-Zn-rare earth alloys, *Metall. Mater. Trans. A*, *26*, 1947–1955.

Wesling, W., T. Ryspaev, and A. Schram (2007), Effect of overageing temperature on the superplastic behaviour in magnesium alloys, *Mater. Sci. Eng., A 462*, 144–148.

Williams, D. B., and C. B. Carter (1996), *Transmission Electron Microscopy. A Textbook for Materials Science*, Plenum Press, New York.

Yano, T., O. Yanagisawa, and M. Ohmori (1988), Deformation of a fiber-reinforced composite induced by temperature change and external loading, *J. Jpn. Inst. Metals*, *52*, 229–235.

Yi, S. B., H.-G. Brokmeier, and S. Zaefferer (2006), Mechanical behaviour and microstructural evolution of magnesium alloy AZ31 in tension at different temperatures, *Mater. Sci. Eng. A*, *424*, 275–281.

Zehetbauer, M. J. (2003), Nanomaterials by severe plastic deformation (SPD), *Adv. Eng. Mater.*, *5*, 265.

Zhang, J., Z. Fan, Y.-Q. Wang, and B.-L. Zhou (2000), Microstructure and mechanical properties of in situ Al-Mg_2Si composites, *Mat. Sci. Techn.*, *16*, 913–918.

Zhu, Y. T., and T. G. Langdon (2004), Fundamentals of Nanostructured Materials by Severe Plastic Deformation, *JOM*, *56*, 58–63.